Simulation of quantum corrals

Dissertation
von
Bernd Donner

23. September 2004

Physik-Department der Technischen Universität München
Institut für theoretische Physik T30

Simulation of quantum corrals

Bernd Donner

Vollständiger Abdruck der von der Fakultät für Physik der Technischen Universität München zur Erlangung des akademischen Grades eines Doktors der Naturwissenschaften (Dr. rer. nat.) genehmigten Dissertation.

Vorsitzender: Univ.-Prof. Dr. Martin Stutzmann
Prüfer der Dissertation:
1. Univ.-Prof. Dr. Manfred Kleber
2. Univ.-Prof. Dr. Axel Groß

Die Dissertation wurde am 27.9.2004 bei der Technischen Universität München eingereicht und durch die Fakultät für Physik am 22.11.2004 angenommen.

Contents

List of Figures

Chapter 1

Introduction

This thesis puts forward a three–dimensional model of scanning tunnelling microscope images. This model, which is based on the so–called source theory, is capable of simulating a multitude of experimental pictures, such as images of quantum corrals and quantum mirages.

The scanning tunnelling microscope (STM) was invented by Binnig and Rohrer in 1982. Four years later, they were awarded the Nobel Prize for their work. One of the most extraordinary features of the STM is that it can resolve single atoms even in closed packed surfaces, that is, it can resolve single atoms in the smoothest known objects.

Basically, an STM (figure 1.1) consists of a metal tip that scans the surface of the probe, without actually touching the probe. The tip–probe distance is about 3–10Å. The tip is moved by three piezoelectric elements, so that the position of the tip relative to the surface can be controlled on a 0.1Å scale. A voltage is applied between the tip and the probe. The resulting total current through the tip is the quantity that determines the STM image generation. The total current through the tip depends, in a zero order approximation, exponentially on the tip–probe distance. In the 'straightforward' mode of operation—the constant height mode—it is the total current values that are directly visualised. Due to some experimental problems, however, especially the unintended drift of the tip towards or away from the probe (which results from e.g. temperature change), this mode of operation is hardly used now. Instead of the constant height mode, it is the constant current mode that is used nowadays. In the constant current mode, the total current through the tip is kept constant. The height of the tip is controlled by a feedback loop so that the current stays constant while the tip moves along the probe. In this mode of operation, the height changes of the tip (the so called corrugation) are visualised. Nonetheless, the STM pictures of the two different modes look very alike. The raw data for these STM images consist of a single value for

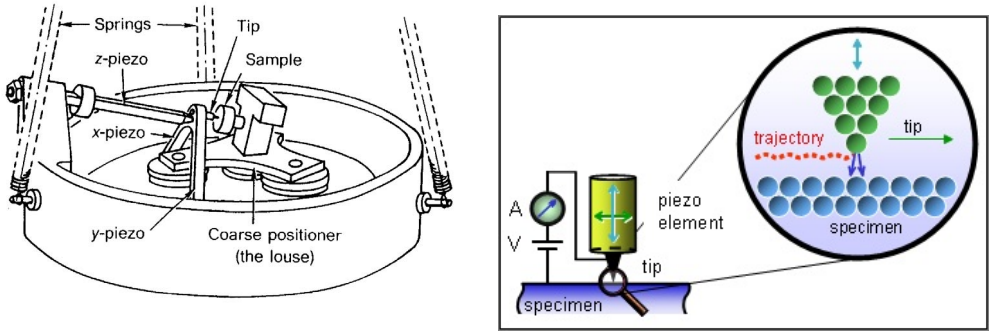

Figure 1.1: A schematic illustration of the scanning tunnelling microscope.

each (x, y) position of the tip. These values are usually graphically enhanced in false colour to yield the well known STM pictures.

The actual measurement takes approximately one minute. This is extremely long compared to the typical time scale of the observed atoms (for the propagation of a sound wave the oscillation period of the atoms is about $\approx 10^{-13}$s). Therefore, to achieve atomic resolution, the STM must be operated at about 4K. Experimentally, with an STM only relative distances and the total current through the tip can be controlled very precisely. It must be emphasised that the absolute tip–probe distance (apart from the difficulty to define this distance) is unknown on a 0.1Å scale and can be only speculated upon.

The STM has several constraints on the probe and on the measurement. Only conducting probes can be inspected by an STM. To get around this limitation, the so called atomic force microscope (AFM) has been developed. Until now, the AFM could not achieve the extremely high resolutions that an STM can, but due to its broader field of application, it is more often used today. One of the most fundamental problems for all scanning techniques is the very bad time resolution. This drastically reduces the possible applications. Especially in the medical and biological sciences, where one would prefer to study chemical reactions with an atomic resolution, the scanning techniques are almost useless. Nevertheless, they are still employed due to the extraordinary spatial resolution. In experimental solid state physics, for instance, the STM is a useful instrument to study the crystal surface. It is namely the straightforward way to analyse the results of epitaxial experiments.

The history of quantum corrals begins with the pioneering work of Ei-

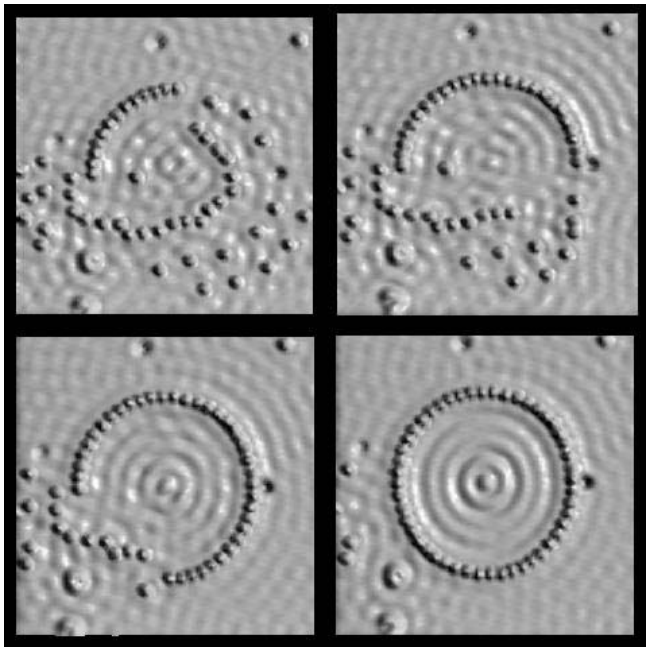

Figure 1.2: Here, some intermediate steps during the experimental construction of a quantum corral are shown. The surface is a Cu(111) surface, while the adatoms are Fe atoms. The corral has a radius of 71.3Å.

gler and Schweizer (1990), who were the first to demonstrate that the STM could be used to controllably move atoms from place to place on the surface of a substrate (figure 1.2). Not long afterwards, Crommie et al built the first quantum corrals from iron atoms on the Cu(111) surface and observed standing–wave patters inside them. In the early experiments it was thought that "stadium"–shaped corrals could be used as a laboratory to study "quantum chaos", but the walls proved too leaky for the electrons to bounce around the unstable periodic orbits long enough to detect any "scarring" effects [27]. A very intriguing recent STM corral experiment was done by Manoharan et al [26], who combined the physics of quantum corrals with the Kondo effect. In a special corral geometry, a "mirage" of the spectroscopic response of a spatially localized Kondo impurity can be observed. The mirage experiment achieves this by taking advantage of both the locally modified electron density in the corral and the scattering properties of a Kondo impurity.

In this thesis, a unified theoretical model of the STM is presented. The model is unified because it is possible to reproduce by this theory STM images of simple metallic surfaces, STM images of the famous circular quantum corral as well as STM images of the relatively new quantum mirage

that is based on the Kondo effect. In addition, the theoretical approach is fully three–dimensional. The quantum corral and the Kondo mirage are usually treated only in two space dimensions. Although this two–dimensional treatment is of enormous importance, as it could clarify some common misunderstandings that will be explained shortly, nevertheless, it will be shown in this thesis that the third space dimension contributes some fundamental ingredients to the understanding of the corral images.

Even in some recently published works, it is claimed that the electron were confined inside the corral. The name "corral" suggests this interpretation, but it was shown almost a decade ago that the electron is not confined within the circular area. The corral wall of 48 adatoms with a nearest neighbour distance of approximately 9Å are definitely too leaky to limit the electron propagation in the direction parallel to the surface. One could say that this recognition is one of the most significant results of the two–dimensional model of the quantum corral. This result, published long ago, will of course be reproduced by the presented three–dimensional theory.

The theory used in this thesis to simulate the STM is the so–called source theory. Mathematically, a source region is introduced in the model. In this source region, particle conservation is not valid. Such an approach has some great advantages. Usually, in scattering theory, the incident and the evanescent waves are only considered asymptotically. Such a description is inadequate for an STM since the tip is by no means infinitely far away from the probe. The fact that the STM could not be treated by ordinary scattering theory turned the theoretical treatment of an STM into a challenge. The first theory that was capable to describe the STM theoretically was the Tersoff–Hamann theory. Although it is the standard theory of an STM, it lacks some mathematical precision. The transfer Hamiltonian method used is based on Fermi's golden rule (which is called a rule and not a theorem or law for good reasons). The presented theory sets out from a model Hamiltonian, and from that point onwards rigorous derivations lead finally to the prediction of STM images that can be compared with experimental results. Thus from the point of view of formal clarity, the source theory of an STM should be considered superior to the standard theory.

In this thesis, a single particle approach is taken. It should be mentioned, however, that there exist some multi–particle calculations for an STM that employ extensive numerical know how. These calculations already try to reproduce STM pictures quantitatively. Although the presented approach cannot reproduce the STM images in full detail, and the assumed model Hamiltonian obviously contains some drastic approximations, nevertheless, these simplifications make the problem much more tractable and finally lead to insights that might have been disguised by the overall complexity of the

more realistic multi–particle treatment. One of the greatest merits of the presented theory is that the wavelength of the standing wave pattern in the corral can be explained and predicted. Although the starting point of the three–dimensional approach taken here is quite different from that of the two–dimensional model introduced by Heller, it will be seen in chapter 4.3 that these two theories are closely related to each other.

The second chapter introduces the theoretical foundations on which the simulation of the STM is based. In particular, some fundamental properties of the source theory are presented. Although this chapter is no easy reading, it provides the essentials for the application of the source theory to an STM. All physical quantities and parameters that will be referred to in later chapters are introduced here.

The third chapter presents a multitude of simulated STM images, including images from simple metal surfaces as well of various quantum corrals. This chapter illustrates the flexibility of the theory on which the simulation of an STM is based.

In the fourth chapter, the influence of the parameters of the model on the images is studied in detail. The goal of this chapter is to provide a physical interpretation of these parameters. Thus, the so far purely mathematical model can be filled with 'philosophy'.

Since this simulation of an STM was actually implemented, several numerical problems had to be addressed. The fifth chapter shows how these difficulties can be handled so that a simulation may achieve the accuracy required to reproduce STM images. Although motivated from a numerical point of view, this chapter also reveals some interesting physical properties of the model.

The sixth chapter is entirely devoted to the Kondo effect and its application in the quantum mirage. The "Kondo effect" in fact embraces several anomalous properties of dilute magnetic alloys. The necessary aspects for the quantum mirage are not addressed in standard solid state physics textbooks. Thus, this chapter starts with a comprehensive but still 'digestible' assembly of well known properties, and sketches their theoretical background with regard to the solution of the quantum mirage. Equipped with these fundamentals, the simulation of an STM is extended to quantum mirages. The chapter concludes with simulated images that exhibit the experimental properties of quantum mirages.

Chapter 2

Foundations

2.1 Source theoretical method in a nutshell

The source theoretical approach — abbreviated in the following as source theory — can be used and has been used to solve very different physical problems. In the following, the basic ideas of this theory will be illustrated by examining a concrete problem, a scanning tunnelling microscope (STM). The STM is modelled by the source theory, making the prediction of measurable quantities possible. In case of an STM, the only directly measurable quantities are the current and the relative distances of tip positions.

It is well known that the constant current or constant height images of an STM are determined by the physical properties of the tip–vacuum–probe region. Due to the very small size of this region, it is standard to describe the tip–vacuum–probe region by the Schrödinger equation. Since the STM tip is fixed in space (its motion is very slow on microscopic time scales) and the whole system is in equilibrium during the measurement, it is adequate to treat the measurement as a stationary problem. Thus the problem of evaluating the total current and other measurable quantities is best solved by the stationary Schrödinger equation.

$$\left(E + \frac{\hbar^2}{2M}\nabla^2 - U(\mathbf{r})\right)\phi(\mathbf{r}) = 0. \tag{2.1}$$

Next, the potential $U(\mathbf{r})$ would be used to describe the tip–vacuum–probe region. But there is a principal problem with equation (2.1) describing an STM.

In the approach sketched above, it seems to be natural to view the tip as an electron source. Accordingly, the electrons start from the tip and end in infinity, the boundary of the physical space. In between, their motion

is subject to the tip–vacuum–probe potential. But equation (2.1) does not permit a region other than the boundary of the physical space to be a particle source. This can be seen from:

$$\mathbf{j}(\mathbf{r}) = -\frac{i\hbar}{2M}\big(\phi^*(\mathbf{r})\nabla\phi(\mathbf{r}) - \phi(\mathbf{r})\nabla\phi^*(\mathbf{r})\big) = \frac{\hbar}{M}\,\mathrm{Im}\big(\phi^*(\mathbf{r})\nabla\phi(\mathbf{r})\big). \tag{2.2}$$

This shows that the total current through any closed surface ∂S is zero:

$$J(E) = \int_{\partial S} \mathbf{j}(\mathbf{r})\,df = \frac{2}{\hbar}\int_S \mathrm{Im}\big(\phi^*(\mathbf{r})\nabla^2\phi(\mathbf{r})\big)\,d^3r = 0. \tag{2.3}$$

$J(E)$ is the contribution to the total current of the electrons that have the energy E. In the source theory, equation (2.1) is modified by a source term $\varsigma(\mathbf{r})$ on the right hand side. This method was also proposed by Schwinger [57] and is very similar to the introduction of heat sources in the heat conduction equation. The fundamental equation of source theory is thus:

$$\left(E + \frac{\hbar^2}{2M}\nabla^2 - U(\mathbf{r})\right)\phi(\mathbf{r}) = \varsigma(\mathbf{r}). \tag{2.4}$$

That the introduction of the source term $\varsigma(\mathbf{r})$ has the desired effect of introducing particle sources other than the boundaries of physical space shows the following calculation:

$$J(E) = \int_{\partial S} \mathbf{j}(\mathbf{r})\,df = \frac{2}{\hbar}\int_S \mathrm{Im}\big(\phi^*(\mathbf{r})\varsigma(\mathbf{r})\big)\,d^3r. \tag{2.5}$$

Here the identity:

$$\mathrm{div}\,\mathbf{j}(\mathbf{r}) = \frac{\hbar}{M}\,\mathrm{Im}\big(\phi^*(\mathbf{r})\nabla^2\phi(\mathbf{r})\big) = \frac{2}{\hbar}\,\mathrm{Im}\big(\phi^*(\mathbf{r})\varsigma(\mathbf{r})\big) \tag{2.6}$$

has been used. Now equation (2.5) states that the total current through any surface must disappear as long as the source $\varsigma(\mathbf{r})$ is not inside this surface. Or more precisely:

$$\mathrm{supp}(\varsigma(\mathbf{r})) \cap S = \emptyset \qquad \Longrightarrow \qquad J(E) = 0. \tag{2.7}$$

Equation (2.6) is the equation of continuity within the stationary source model.

To solve equation (2.4), the Green's function formalism is very useful, since it has been developed to solve partial differential equations with inhomogeneity. Some very fundamental theorems will be merely stated here; for their rigorous derivation, see for example [3].

Let ϕ and ψ be solutions of equation (2.4). Then $\phi - \psi$ is a solution of the stationary Schrödinger equation (2.1). Thus determining all solutions of the homogeneous equation (2.1) and only one special solution of the inhomogeneous equation (2.4) suffice to solve the problem. This special solution of the inhomogeneous equation (2.4) is given by the Green's functions theory:

$$\left(E + \frac{\hbar^2}{2M}\nabla^2 - U(\mathbf{r})\right) G(\mathbf{r}, \mathbf{r}', E) = \delta(\mathbf{r} - \mathbf{r}'). \tag{2.8}$$

The product $G^*(\mathbf{r}, \mathbf{r}', E)G(\mathbf{r}, \mathbf{r}', E)$ is proportional to the probability to find a particle at $\mathbf{r}$ that has been created at $\mathbf{r}'$. If a single Green's function $G(\mathbf{r}, \mathbf{r}', E)$ has been determined then the special solution of the inhomogeneous equation (2.4) is given by:

$$\phi(\mathbf{r}) = \int_{\mathbb{R}^3} \varsigma(\mathbf{r}') G(\mathbf{r}, \mathbf{r}', E) d^3r'. \tag{2.9}$$

After presenting the fundamental mathematical properties of the source theory, it must be illustrated how the so far still unspecified quantities $U(\mathbf{r})$, $G(\mathbf{r}, \mathbf{r}', E)$ and $\varsigma(\mathbf{r})$ are used to describe an STM.

2.2 Connecting theory and experiment

The measured quantity in an STM experiment is the total current that runs through the tip at a certain tip position. In the constant height mode, the current is directly measured. In the constant current mode, it is again the total current through the tip that directly controls the corrugation via the feedback loop. This total current can be directly calculated from Green's functions: Substituting equation (2.9) in equation (2.6) and applying the divergence theorem leads to:

$$J(E) = -\frac{2}{\hbar} \int_{\mathbb{R}^3} \int_{\mathbb{R}^3} \mathrm{Im}\big(\varsigma^*(\mathbf{r}') G(\mathbf{r}, \mathbf{r}', E) \varsigma(\mathbf{r})\big) d^3r'\, d^3r. \tag{2.10}$$

The total current J_{tot} is given by the corresponding occupation probability factors of the tip and the probe:

$$J_{\mathrm{tot}} = \int \left[f(E - \epsilon_F + eV) - f(E - \epsilon_F)\right] J(E)\, dE. \tag{2.11}$$

For sufficiently low temperatures, the occupation probability factor

$$f(E - \mu) = \frac{1}{1 + e^{\frac{E-\mu}{k_b T}}} \tag{2.12}$$

degenerates to a step function. The conductivity defined as

$$\sigma \stackrel{\text{def}}{=} \frac{d}{dV} J_{\text{tot}} \tag{2.13}$$

can now be calculated for very small temperatures. Using the non trivial relation,

$$\lim_{T \to 0} \frac{d}{dV} f(E - \epsilon_F + eV) = e\delta(E - \epsilon_F + eV), \tag{2.14}$$

the conductivity is given by:

$$\sigma = e^2 J(\epsilon_F - eV). \tag{2.15}$$

From equation (2.13), the total current J_{tot} can now be easily calculated. Since the total current disappears when the applied voltage $V = 0$, the total current J_{tot} is given by the following integral:

$$J_{\text{tot}} = \int_0^V \sigma(V')dV' = e^2 \int_0^V J(\epsilon_F - eV')dV'. \tag{2.16}$$

The bias voltage V has typically a magnitude of 10mV in an STM experiment. If the conductivity happens to be constant in this relatively small region, the total current is given by:

$$J_{\text{tot}} = V \cdot \sigma = e^2 V J(\epsilon_F - eV). \tag{2.17}$$

In general, equation (2.17) will only be an approximation of the exact current through the STM. As long as the sample does not expose any extremely energy dependent effects, the approximation (2.17) is justified and employed in almost every theoretical description of STM pictures. For small temperatures and small bias voltages V, only the electrons with energy ϵ_F contribute to J_{tot}. The well known "quantum mirage" discussed in section 6 is a prominent example where this approximation must fail, since the scattering properties of the Kondo adatoms are highly energy dependent. In both cases (equation (2.17) and (2.16)), the simulation of STM pictures is reduced to the evaluation of Green's functions.

2.3 The physical Green's function

The retarded Green's function $G_{\text{ret}}(\mathbf{r}, \mathbf{r}', E)$ is a special solution of

$$\big(E - \hat{H}\big) G(\mathbf{r}, \mathbf{r}', E) = \delta(\mathbf{r} - \mathbf{r}'), \tag{2.18}$$

where $\hat{H}$ as usually denotes the Hamiltonian defined as:

$$\hat{H} = -\frac{\hbar^2}{2M}\Delta + U(\mathbf{r}). \tag{2.19}$$

M is the mass of the electron. The retarded Green's function can be obtained from the time development operator $\hat{U}(\mathbf{r}, \mathbf{r}', t-t')$ via a Laplace transform. It is well known that the time development operator is given by: $\hat{U}(\tau) = e^{-i\frac{\hat{H}\tau}{\hbar}}$ (compare for instance [3], pages 260–261). The retarded Green's function defined as

$$G_{\mathrm{ret}}(\mathbf{r}, \mathbf{r}', E) \stackrel{\mathrm{def}}{=} -\frac{i}{\hbar}\lim_{\eta\to 0^+}\int_0^\infty \hat{U}(\mathbf{r}, \mathbf{r}', \tau)e^{i\frac{(E+i\eta)\tau}{\hbar}}d\tau \tag{2.20}$$

satisfies equation (2.18). This can be verified by a simple substitution (compare [35], pages 349–351). Let $\phi(E, \mathbf{r})$ be the bounded and normalised solution (eigenfunction) of the Schrödinger equation:

$$\left(E + \frac{\hbar^2}{2M}\Delta - U(\mathbf{r})\right)\phi(E, \mathbf{r}) = 0. \tag{2.21}$$

Equation (2.20) shows that the retarded Green's function can be expressed in terms of the eigenfunctions:

$$G_{\mathrm{ret}}(\mathbf{r}, \mathbf{r}', E) = \lim_{\eta\to 0^+}\int \frac{\phi(\mu, \mathbf{r})\phi^*(\mu, \mathbf{r}')}{E - \mu + i\eta}d\mu. \tag{2.22}$$

Here the integral over μ is understood as integration over the continuous energy spectrum and summation over the discrete energy spectrum. Using the well known identity

$$\lim_{\eta\to 0^+}\int \frac{\phi(\mu)}{E - \mu \pm i\eta}d\mu = \int_{PV}\frac{\phi(\mu)}{E-\mu}d\mu \mp i\pi\int \phi(\mu)\delta(\mu - E)d\mu$$

and the definition of the fundamental Green's function

$$G_{\mathrm{f}}(\mathbf{r}, \mathbf{r}', E) \stackrel{\mathrm{def}}{=} \int_{PV}\frac{\phi(\mu, \mathbf{r})\phi^*(\mu, \mathbf{r}')}{E - \mu}d\mu, \tag{2.23}$$

where PV means the principal value, the relation (2.22) can be recast in the form:

$$G_{\mathrm{ret}}(\mathbf{r}, \mathbf{r}', E) = G_{\mathrm{f}}(\mathbf{r}, \mathbf{r}', E) - i\pi\int \phi(\mu, \mathbf{r})\phi^*(\mu, \mathbf{r}')\delta(\mu - E)d\mu. \tag{2.24}$$

These general properties stated above hold for Green's functions of any dimension, where the dimension of the Green's function is defined by the dimension of the vector $\mathbf{r}$. The following treatment focuses on one–dimensional Green's functions:

$$\left(E + \frac{\hbar^2}{2M}\partial_x^2 - U(x)\right) G_1(x, x', E) = \delta(x - x'). \tag{2.25}$$

Furthermore, it is assumed that the spectrum is not degenerate, that is: if $\phi_1(E, \cdot)$ and $\phi_2(E, \cdot)$ are two wavefunctions with energy $E \in \mathbb{R}$, it follows that $\phi_1 = \phi_2$. Now equation (2.24) can be written as:

$$G_{1\text{ret}}(x, x', E) = G_{1\text{f}}(x, x', E) - i\pi\phi(E, x)\phi^*(E, x'). \tag{2.26}$$

The fundamental Green's function $G_{1\text{f}}(x, x', E)$ satisfies equation (2.18). This can be verified by simple substitution. Thus the fundamental Green's function solves the Schrödinger equation for $(x < x')$ and $(x > x')$. Thus $G_{1\text{f}}(x, x', E)$ can be written as a linear combination of solutions of the Schrödinger equation (not necessarily eigenfunctions). In fact, the following theorem can be proved: Let $y_-(x, E)$ and $y_+(x, E)$ be solutions of the Schrödinger equation. $y_-(x, E)$ is bounded if $x \to -\infty$, and $y_+(x, E)$ is bounded if $x \to \infty$. Then the fundamental Green's function is given by (compare [6]):

$$G_{1\text{f}}(x, x', E) = \begin{cases} y_-(x, E)y_+(x', E) & (x < x') \\ y_+(x, E)y_-(x', E) & (x > x'). \end{cases} \tag{2.27}$$

$y_-(x, E)$ describes the particle in the area $(x < x')$, while $y_+(x, E)$ is the solution for $(x > x')$. In case of a potential well, (that is $U(x) \to \infty$ if $|x| \to \infty$), the spectrum is discrete. Equation (2.27) can be rewritten in the following way

$$G_{1\text{f}}(x, x', E) = \frac{2M}{\hbar^2}\frac{\phi_-(x_<)\phi_+(x_>)}{\mathcal{W}(\phi_-, \phi_+)}, \tag{2.28}$$

with $\mathcal{W}$ being the Wronskian. ϕ_- and ϕ_+ are the unique (up to a factor) bounded solutions in the area $(x < 0)$ and $(x > 0)$, respectively. In case of a continuous spectrum, only the solution in the tunnelling region is unique. The classically allowed region has two linear independent bounded solutions. Using the definition for the fundamental Green's function, the following identity can be proved:

$$G_{1\text{f}}(x, x', E) = \frac{2M}{\hbar^2}\frac{\phi(x_<)\psi_+(x_>)}{\mathcal{W}(\phi, \psi_+)}. \tag{2.29}$$

ϕ is the (up to a factor) unique bounded solution in the region $x \in \mathbb{R}$. ψ_+ is characterised by its asymptotic behaviour: For very large x, the particle moves in a classically allowed region, due to the choice of the potential as given in section 2.5. In this region, the WKB approximation converges to the exact solution of the problem, thus

$$\phi(x,E) \propto \sqrt{\frac{2M}{\pi\hbar^2}} \frac{1}{\sqrt{k(x,E)}} \sin\left(\int_a^x k(\xi,E)d\xi + \delta(E,a)\right) \quad \text{and}$$
$$\psi_+(x,E) \propto \sqrt{\frac{2\pi M}{\hbar^2}} \frac{1}{\sqrt{k(x,E)}} \cos\left(\int_a^x k(\xi,E)d\xi + \delta(E,a)\right). \tag{2.30}$$

The known solution $\phi(x,E)$ defines the scattering phase $\delta(E)$. As usual, $k(x,E) = \sqrt{\frac{2M}{\hbar^2}(E-U(x))}$.

Remark 1 The equations (2.30) can be derived from three conditions, that must be satisfied by the fundamental Green's function $G_{1\mathrm{f}}$:

1. Abel's theorem for the Schrödinger equation shows that the Wronskian of the fundamental solutions must be constant. This is due to the special structure of the differential equation (2.18) (see for instance [5], page 167).
2. The eigenfunctions $\phi(x,E)$ must be orthonormal.
3. The following equation $\int_{\mathbb{R}} \phi(x,E)G_f(x,x',E)\,dx = 0$ must be satisfied. The substitution of the definition (2.23) of the fundamental Green's function into this expression verifies the identity.

The retarded Green's function can now be written as

$$G_{1\mathrm{ret}}(x,x',E) = \frac{2M}{\hbar^2} \frac{\phi(x_<)h_+(x_>)}{\mathcal{W}(\phi,h_+)}, \tag{2.31}$$

where the definition $h_+(x,E) = \psi_+(x,E) - i\pi\phi(x,E)$ is used. The equations (2.30) show that $h_+(x,E)$ behaves like an outgoing wave in the asymptotic region. That means that the current flows from smaller x to greater x (as physically sensible due to the choice of the potential). From now on, when Green's function is mentioned, it is the retarded Green's $G_{\mathrm{ret}}(\mathbf{r},\mathbf{r}',E)$ function that is implicitly meant, if not stated otherwise.

2.4 Specifying the source $\varsigma(\mathbf{r})$

2.4.1 The multipole source

To achieve atomic resolution with an STM, extremely good tips are necessary. The tunnelling current is mainly flowing through a single tip atom. Since

the electrons are emitted from the valence orbital of the tip atom, they have well–defined multipole characteristics. The tip can be seen as a multipole point source. What properties must this point–like multipole source fulfil? Consider the free particle case. As it is well known from the partial wave analysis, the outgoing spherical wave in quantum mechanics is given by:

$$\phi_{lm}(\mathrm{r}, E) = \alpha \mathcal{Y}_{lm}(\hat{r}) h_l^+(kr) = \alpha \frac{\mathcal{Y}_{lm}(\mathbf{r})}{r^l} h_l^+(kr). \tag{2.32}$$

The centre of the spherical wave has been chosen as the origin of the coordinate system. Since the boundary condition for outgoing waves has to be satisfied, the Hankel functions

$$h_l^+(kr) \longrightarrow \frac{e^{+ikr}}{kr} \quad \text{for} \quad r \to \infty \tag{2.33}$$

must be chosen. The constant factor α is determined by the normalisation condition for scattering states.

What is the point–source generating this wavefunction? Before this question is answered, it should be pointed out that a point source that generates the multipole wavefunctions ϕ_{lm} in free space should be called a multipole source. Or turning it the other way round: What should a pointlike multipole source be, but a point–source that has the multipole wavefunctions ϕ_{lm} as solutions in free space? The question of uniqueness of the multipole point–source given by this definition must of course be addressed by the following derivation. With the following identities

$$\frac{\mathcal{Y}_{lm}(\mathbf{r})}{r^{2l+1}} = \frac{1}{(2l-1)!!} \mathcal{Y}_{lm}(-\nabla) \frac{1}{r} \tag{2.34}$$

and

$$\nabla^2 \frac{1}{r} = -4\pi\delta(\mathbf{r}), \tag{2.35}$$

(see [52] equation (20) for a proof), the construction of the source is straight forward:

$$\Big(\nabla^2 + k^2\Big) \alpha \frac{\mathcal{Y}_{lm}(\mathbf{r})}{r^{2l+1}} h_l^+(kr) r^{l+1} = \alpha h_l^+(kr) r^{l+1} \nabla^2 \frac{\mathcal{Y}_{lm}(\mathbf{r})}{r^{2l+1}}. \tag{2.36}$$

Remark 2 To show that the other terms appearing on the right hand side cancel is not difficult, though it is cumbersome. The terms are:

$$\alpha k^2 \mathcal{Y}_{lm}(\hat{r}) h_l^+(kr), \tag{2.37}$$

$$\alpha \frac{\mathcal{Y}_{lm}(\mathbf{r})}{r^{2l+1}} \nabla^2 h_l^+(kr) r^{l+1} \tag{2.38}$$

and

$$2\alpha\Big(\nabla\frac{\mathcal{Y}_{lm}(\mathbf{r})}{r^{2l+1}}\Big)\Big(\nabla h_l^+(kr)r^{l+1}\Big) = \alpha\frac{-2(l+1)}{r}\frac{\mathcal{Y}_{lm}(\mathbf{r})}{r^{2l+1}}\partial_r h_l^+(kr)r^{l+1}. \tag{2.39}$$

The last identity holds since $\nabla h_l^+(kr)r^{l+1}$ is parallel to $\mathbf{e}_r$. The sum of term (2.38) and term (2.39) can be written as:

$$\alpha\frac{\mathcal{Y}_{lm}(\mathbf{r})}{r^{2l+1}}k^{-l-1}k^2\Big(\partial_{kr}^2 - \frac{2l}{kr}\partial_{kr}\Big)h_l^+(kr)(kr)^{l+1}. \tag{2.40}$$

Employing the differentiation formula [1] 10.1.23 for Bessel functions gives:

$$\Big(\partial_x^2 - \frac{2l}{x}\partial_x\Big)h_l^+(x)x^{l+1} = \Big(x\partial_x\frac{1}{x}\partial_x - \frac{2l-1}{x}\partial_x\Big)h_l^+(x)x^{l+1} = x^{l+1}\Big(h_{l-2}^+(x) - \frac{2l-1}{x}h_{l-1}^+(x)\Big) \tag{2.41}$$

Since the term on the right hand side is the recurrence relation ([1] 10.1.19):

$$x^{l+1}\Big(h_{l-2}^+(x) - \frac{2l-1}{x}h_{l-1}^+(x)\Big) = -x^{l+1}h_l^+(x), \tag{2.42}$$

the sum of the term (2.38) and term (2.39) simplifies to:

$$-\alpha\frac{\mathcal{Y}_{lm}(\mathbf{r})}{r^{2l+1}}k^{-l-1}k^2(kr)^{l+1}h_l^+(kr) = -\alpha k^2\mathcal{Y}_{lm}(\hat{r})h_l^+(kr), \tag{2.43}$$

which is exactly the negative of the term (2.37).

With the above relations (2.34) and (2.35), the source is now easily constructed:

$$\Big(\nabla^2 + k^2\Big)\alpha\frac{\mathcal{Y}_{lm}(\mathbf{r})}{r^{2l+1}}h_l^+(kr)r^{l+1} = -\alpha h_l^+(kr)r^{l+1}\frac{4\pi}{(2l-1)!!}\mathcal{Y}_{lm}(-\nabla)\delta(\mathbf{r}). \tag{2.44}$$

Since the source term on the right hand side is zero except for $\mathbf{r} = 0$, the asymptotic behaviour

$$\lim_{r\to 0} h_l^+(kr)r^{l+1} = (-i)\frac{(2l-1)!!}{k^{l+1}} \tag{2.45}$$

(this relation can be derived from [1] 10.1.16) and the definition

$$\delta_{lm}(\mathbf{r}-\mathbf{r}') \stackrel{\text{def}}{=} \mathcal{Y}_{lm}\Big(\frac{\partial}{\partial\mathbf{r}'}\Big)\delta(\mathbf{r}-\mathbf{r}') = \mathcal{Y}_{lm}\Big(-\frac{\partial}{\partial(\mathbf{r}-\mathbf{r}')}\Big)\delta(\mathbf{r}-\mathbf{r}') \tag{2.46}$$

can be used to get the important result:

$$\Big(\frac{\hbar^2}{2M}\nabla^2 + E\Big)\phi_{lm}(\mathbf{r},E) = i\alpha\frac{2\pi\hbar^2}{Mk^{l+1}}\delta_{lm}(\mathbf{r}). \tag{2.47}$$

In analogy to equation (2.8), the free multipol Green's functions can be defined as:

$$\Big(\frac{\hbar^2}{2M}\nabla^2 + E\Big)G_{lm}(\mathbf{r},\mathbf{r}',E) = \delta_{lm}(\mathbf{r}-\mathbf{r}'), \tag{2.48}$$

where the multipol source is located at $\mathbf{r}'$. From equation (2.47) it is easily seen that the free multipole Green's function is given by:

$$G_{lm}(\mathbf{r}, \mathbf{r}', E) = \frac{1}{i} \frac{Mk^{l+1}}{2\pi\hbar^2} \mathcal{Y}_{lm}(\hat{R}) h_l^+(kR), \tag{2.49}$$

with $R = |\mathbf{r} - \mathbf{r}'|$. Obviously, the spherical wave is related to the multipole Green's function by:

$$\phi_{lm}(\mathbf{r}, E) = i\alpha \frac{2\pi\hbar^2}{Mk^{l+1}} G_{lm}(\mathbf{r}, \mathbf{0}, E). \tag{2.50}$$

2.4.2 The normalisation condition

The normalisation condition is given by

$$\delta(E - E') = \int_{\mathbb{R}} \phi_{lm}(\mathbf{r}, E) \phi_{lm}^*(\mathbf{r}, E') d^3r. \tag{2.51}$$

With the well know relation

$$\int_0^{2\pi} \int_0^{\pi} Y_{lm}(\theta, \phi) Y_{lm}^*(\theta, \phi) \sin(\theta)\, d\theta d\phi = 1 \tag{2.52}$$

(see [55], page 454) for spherical harmonics, equation (2.51) can be written as:

$$\delta(E - E') = \alpha\alpha^* \int_0^{\infty} h_l^+(kr) h_l^-(k'r) r^2\, dr. \tag{2.53}$$

The singular part of this integral depends only on the asymptotic behaviour of the spherical Hankel functions given by equation (2.33). Thus the Hankel functions can be replaced by their asymptotes in the above integral:

$$\delta(E - E') = \alpha\alpha^* \pi \frac{1}{kk'} \delta(k - k') = \alpha\alpha^* \pi \frac{1}{k^2} \frac{k\hbar^2}{M} \delta(E - E'). \tag{2.54}$$

Thus the spherical wave is given by:

$$\phi_{lm}(\mathrm{r}, E) = -i \sqrt{\frac{Mk}{\pi\hbar^2}} \mathcal{Y}_{lm}(\hat{r}) h_l^+(kr). \tag{2.55}$$

The arbitrary phase factor $-i$ has been chosen, so that later quantities (in particular the λ_{lm}) do not have a complex phase.

2.4.3 The multipole source in arbitrary potentials

It will be shown that although the multipole source is embedded in a non–constant potential, the Green's function

$$\Big(E + \frac{\hbar^2}{2M} - U(\mathbf{r})\Big) G_{lm}(\mathbf{r}, \mathbf{r}', E) = \delta_{lm}(\mathbf{r} - \mathbf{r}') \tag{2.56}$$

shows the (l, m)-multipole characteristics in the vicinity of the the source. From the definition (2.46) of the multipole sources it is obvious that the Green's function G_{lm} is given by:

$$G_{lm}(\mathbf{r}, \mathbf{r}', E) = \mathcal{Y}_{lm}\Big(\frac{\partial}{\partial \mathbf{r}'}\Big) G(\mathbf{r}, \mathbf{r}', E), \tag{2.57}$$

where the Green's function G is retarded and fulfils equation (2.9). The above statement about the behaviour of the multipole Green's function can be expressed as:

$$G_{lm}(\mathbf{r}, \mathbf{r}', E) = \mathcal{Y}_{lm}(\theta, \phi) R(r) = \frac{\mathcal{Y}_{lm}(\mathbf{r} - \mathbf{r}')}{r^l} R(r) \quad \text{for} \quad \mathbf{r} \approx \mathbf{r}', \tag{2.58}$$

where $R(r)$ is an arbitrary radial function and r, ϕ and θ are the spherical coordinates of $\mathbf{r} - \mathbf{r}'$. The following fundamental theorem describes the behaviour of the Green's G function in the vicinity of the tip:

Let $\hat{H}(\mathbf{r}) = \frac{\hbar^2}{2M}\nabla^2 + U(\mathbf{r})$ be a self–adjoint Hamiltonian with a potential $U(\mathbf{r})$ which is analytic in a sector $\mathbb{S} \subseteq \mathbb{R}^3$. When the retarded Green's function $G(\mathbf{r}, \mathbf{r}', E)$ exists for an $E \in \mathbb{R}$, it may be displayed in the form:

$$G(\mathbf{r}, \mathbf{r}', E) = -\frac{M}{2\pi\hbar^2} \frac{f(\mathbf{r}, \mathbf{r}', E)}{|\mathbf{r} - \mathbf{r}'|} + h(\mathbf{r}, \mathbf{r}', E), \tag{2.59}$$

where $f(\mathbf{r}, \mathbf{r}', E) = f(\mathbf{r}', \mathbf{r}, E)$ is a real symmetric function which is analytic for $\mathbf{r}, \mathbf{r}' \in \mathbb{S}$. Furthermore, the leading–order expansion of f reads:

$$f(\mathbf{r}, \mathbf{r}', E) = f^*(\mathbf{r}, \mathbf{r}', E) = 1 - \frac{M(E - U(\mathbf{r}'))}{\hbar^2} (\mathbf{r} - \mathbf{r}')^2 + \mathcal{O}(r_k^3, r_k'^3). \tag{2.60}$$

The function $h(\mathbf{r}, \mathbf{r}', E)$ is a solution of the homogeneous Schrödinger equation and analytic in $\mathbf{r}, \mathbf{r}' \in \mathbb{S}$. If E is not an eigenvalue of $\hat{H}(\mathbf{r})$, then $h(\mathbf{r}, \mathbf{r}', E)$ is also a real and symmetric function. (See [6], appendix 5 for a proof of this important theorem.)

With this theorem at hand, it is an easy task to calculate the leading–order expansion of the multipole Green's functions G_{lm}:

$$\begin{aligned} \mathcal{Y}_{lm}\left(\frac{\partial}{\partial \mathbf{r}'}\right) G(\mathbf{r}, \mathbf{r}', E) = \\ - \frac{M}{2\pi\hbar^2} \mathcal{Y}_{lm}\left(\frac{\partial}{\partial \mathbf{r}'}\right)\left(\frac{f(\mathbf{r}, \mathbf{r}', E)}{|\mathbf{r} - \mathbf{r}'|}\right) + \mathcal{Y}_{lm}\left(\frac{\partial}{\partial \mathbf{r}'}\right) h(\mathbf{r}, \mathbf{r}', E). \end{aligned} \tag{2.61}$$

A relatively easy calculation shows that (for details refer to [6])

$$\mathcal{Y}_{lm}\left(\frac{\partial}{\partial \mathbf{r}'}\right)\left(\frac{f(\mathbf{r},\mathbf{r}',E)}{|\mathbf{r}-\mathbf{r}'|}\right) = (2l+1)!!\frac{\mathcal{Y}_{lm}(\mathbf{r}-\mathbf{r}')}{|\mathbf{r}-\mathbf{r}'|^{2l+1}}\left(1+\frac{M(E-U(\mathbf{r}'))(\mathbf{r}-\mathbf{r}')^2}{\hbar^2(2l-1)}+\mathcal{O}\big((\mathbf{r}-\mathbf{r}')^4\big)\right). \tag{2.62}$$

Since $\mathcal{Y}_{lm}\big(\frac{\partial}{\partial \mathbf{r}'}\big)h(\mathbf{r},\mathbf{r}',E)$ is analytic, as a derivative of an analytic function, the Green's function is given by

$$G_{lm}(\mathbf{r},\mathbf{r}',E) \approx (2l+1)!!\frac{\mathcal{Y}_{lm}(\mathbf{r}-\mathbf{r}')}{|\mathbf{r}-\mathbf{r}'|^{2l+1}} \qquad \text{when} \qquad \mathbf{r}\approx\mathbf{r}'. \tag{2.63}$$

This behaviour is independent from the surrounding potential.

2.4.4 Transport limit for multipole sources

By now, the source term has been determined except for a constant factor λ_{lm}:

$$\Big(E+\frac{\hbar^2}{2M}\nabla^2-U(\mathbf{r})\Big)\phi(\mathbf{r},\mathbf{r}',E)=\lambda_{lm}\delta_{lm}(\mathbf{r}-\mathbf{r}'). \tag{2.64}$$

This parameter λ_{lm} is called source strength for obvious reasons. As shown in section 2.4.2, this factor is determined by the orthonormality of the states ϕ. The orthonormality of the states is a mathematical reformulation of the Pauli principle, that only one particle is in a certain energy eigenstate. In case of an STM, the particles emitted by the source are electrons. The spin quantum number of the electrons has not been taken into account so far. Since electrons emitted from the STM tip are not spin polarised, it would just bloat the formalism if spin up $\phi^{\uparrow}$ and spin down $\phi^{\downarrow}$ wavefunctions where used. Instead, the Pauli principle can be adapted to this special case: only two particles (spin up, spin down) can be in the same energy eigenstate

$$\int_{\mathbb{R}^3}\phi(\mathbf{r},\mathbf{r}',E)\phi^*(\mathbf{r},\mathbf{r}',E')\,d^3r = 2\delta(E-E'). \tag{2.65}$$

Even if this expression (2.65) could be evaluated for arbitrary potentials $U(\mathbf{r})$, the parameter λ_{lm} will usually depend on the energy E as well as on the potential $U(\mathbf{r})$. To eliminate the dependancy on the potential $U(\mathbf{r})$, the following approximation can be employed: The parameters λ_{lm} for a potential $U(\mathbf{r})$ is equal to the parameter λ_{lm} for $U(\mathbf{r})=0$. Therefore, the λ_{lm} are independent from the potential in this approximation.

Comparing equation (2.64) and equation (2.56), it is easily seen that

$$\phi(\mathbf{r}, \mathbf{r}', E) = \lambda_{lm} G_{lm}(\mathbf{r}, \mathbf{r}', E). \tag{2.66}$$

At first, the function ϕ will be evaluated for the field free case. Then the λ_{lm}'s are given by equation (2.66), since the free multipole Green's functions are well known (equation (2.49)). The necessary integrals have all been evaluated in section 2.4.2 (see especially equation (2.54)) and differ only by a factor 2, so the result can be stated immediately:

$$2\delta(E - E') = \alpha\alpha^* \pi \frac{1}{k^2} \frac{k\hbar^2}{M} \delta(E - E'). \tag{2.67}$$

Now ϕ is:

$$\phi(\mathbf{r}, \mathbf{r}', E) = -i\sqrt{\frac{2Mk}{\pi\hbar^2}} \mathcal{Y}_{lm}(\hat{r}) h_l^+(kr). \tag{2.68}$$

With equation (2.66) and equation (2.49), the source strength λ_{lm} is:

$$|\lambda_{lm}|^2 = -\frac{8\pi\hbar^2}{Mk^{2l+1}}. \tag{2.69}$$

Due to the approximation, the parameter k in equation (2.69) needs some thought. In case of an arbitrary potential, it cannot be the energy E that determines the source strength of the STM tip. The excess energy $U(\mathbf{r}') - E$ of the electron at the tip would come to mind in an ad hoc interpretation of k. But since the tip in an STM is located in the tunnelling region, this interpretation must fail. On the other hand, it is plausible that the momentum k of the electron at the STM tip is given by the momentum of the electron that propagated through the STM tip. Thus addressing continuity, the parameter k can been seen as the Fermi wave vector of the tip material. The Fermi wave vector of typical metals used for the tip (like tungsten) is approximately 1.5Å^{-1}. From now on, this specific value is used consistently through all calculations. Furthermore, this Fermi wave vector will be referred to as k_{tip}.

2.4.5 The multipole tips for an STM simulation

The tunnelling current is exponentially suppressed with increasing distance between the tip and the probe. The spatial extensions of the orbitals ($\approx$ 0.5Å) are of the same magnitude as the tip–probe distance ($\approx$ 4Å). Thus orbitals directed towards the probe give the dominant contribution to the total current. For instance, if the least bound electron is a d–electron, the dominant contribution to the current will come from d_{z^2}–electrons. Here, mainly the following three different multipole tips are considered:

s–orbital: $\mathcal{Y}_{00}\left(\frac{\partial}{\partial \mathbf{r}'}\right) = \frac{1}{\sqrt{4\pi}}$

p_z–orbital: $\mathcal{Y}_{10}\left(\frac{\partial}{\partial \mathbf{r}'}\right) = \sqrt{\frac{3}{4\pi}}\partial_{z'}$

d_{z^2}–orbital: $\mathcal{Y}_{20}\left(\frac{\partial}{\partial \mathbf{r}'}\right) = \sqrt{\frac{5}{16\pi}}(2\partial_{z'}^2 - \partial_{x'}^2 - \partial_{y'}^2) = \sqrt{\frac{5}{16\pi}}(2\partial_{z'}^2 - \frac{1}{\rho}\partial_\rho \rho \partial_\rho)$

2.5 The potential

From now on, the experimental setup is chosen in such a way that the tip is to the left and the probe to the right. Furthermore, the surface of the probe is perpendicular to the z–direction. The potential $U(\mathbf{r}) = U_1(z) + U_2(\mathbf{r})$ is split in two parts. The idea is to separate the contribution of single atoms $U_2(\mathbf{r})$ from a mean tip–vacuum–probe potential $U_1(z)$. The mean potential $U_1(z)$ only varies in the z–direction, while the atomic contribution $U_2(\mathbf{r})$ does not possess this symmetry.

2.5.1 The jellium–model

The jellium–model can be used to calculate the mean tip–vacuum–probe potential $U_1(z)$. This model for the vacuum–probe transition is relatively simple and still exactly solvable. The positively charged ion cores are approximated by a homogeneous background charge, with charge density ρ_+. The conduction electrons move in the potential $\rho_+\theta(z - z_0)$, where z_0 is the surface of the probe. This problem has been solved with the self–consistent equations by Kohn and Sham (see for instance [37, 42, 65, 23]). The potential for the jellium–model has been calculated by the usage of a local approximation of the exchange– and the correlation terms for the inhomogeneous electron gas (figure 2.1). The only parameter of this model is the charge density ρ_+. Assuming that each ion has one positive charge, the charge density ρ_+ can be calculated by the mean nearest ion distance $2r_s$:

$$\rho_+ = \left(\frac{4}{3}\pi r_s^3\right)^{-1}. \tag{2.70}$$

For instance, the quite reasonable choice $r_s = 3a_{\text{Bohr}}$ leads to a charge density of $\rho_+ = 5.94 \cdot 10^{22}\text{cm}^{-3}$. This result is almost the correct charge density for silver and gold. The wavefunction of the exact potential of the jellium–model can only be determined numerically, even in the one–dimensional case. For simplicity, and without loss of physical effects (as will be shown later), the

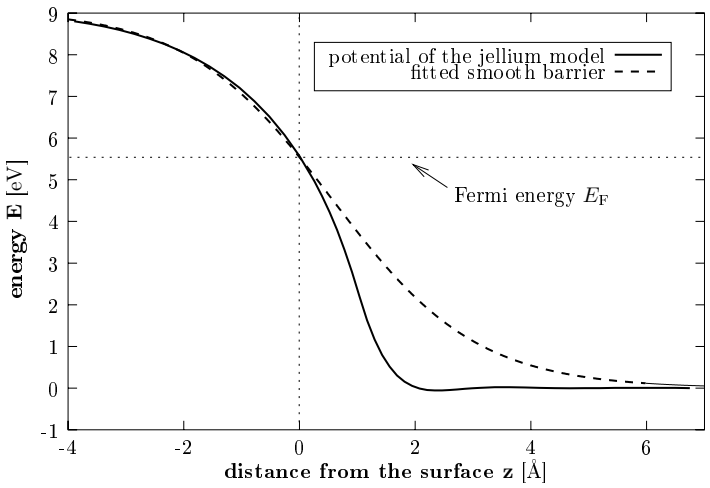

Figure 2.1: The potential distribution of the jellium–model is shown. For details on the calculation of this potential see [42]. A "smooth barrier" with the parameters $V_0 = 9.08\text{eV}$, $\alpha = 0.8\text{Å}^{-1}$ and $\zeta = 0.56\text{Å}$is fitted to the exact potential distribution of the jellium–model.

exact potential is approximated by a smooth barrier that is given by:

$$U_1(z) = \frac{V_0}{1 + e^{\alpha(z-\zeta)}} = \frac{V_0}{2}\left(1 - \operatorname{atanh}\left(\frac{\alpha}{2}(z-\zeta)\right)\right). \tag{2.71}$$

2.5.2 Overview: How to evaluate the three–dimensional Green's function

The evaluation of the Green's function of the complete problem

$$\left(E + \frac{\hbar^2}{2M}\nabla^2 - U_1(z) - U_2(\mathbf{r})\right) G_{lm}(\mathbf{r}, \mathbf{r}', E) = \delta_{lm}(\mathbf{r} - \mathbf{r}') \tag{2.72}$$

is done in two steps:

1. Assuming that the one–dimensional Green's function G_1 for the problem

$$\left(E + \frac{\hbar^2}{2M}\partial_z^2 - U_1(z))\right) G_1(z, z', E) = \delta(z - z') \tag{2.73}$$

is known, the three–dimensional multipole Green's function G^{w}_{lm}

$$\left(E + \frac{\hbar^2}{2M}\nabla^2 - U_1(z)\right) G^{\text{w}}_{lm}(\mathbf{r}, \mathbf{r}', E) = \delta_{lm}(\mathbf{r} - \mathbf{r}') \tag{2.74}$$

can be evaluated. For the following tip-vacuum–probe potentials, one–dimensional Green's functions are presented here: The "step barrier" defined by $U_1(z) = V_1\theta(z) + V_2\theta(-z)$ (see section 5.1.2 for details), the "triangular barrier" and the "smooth barrier". The triangular barrier $U_1(z) = -Fz$ is the potential of the pure electric field (see section 5.1.3) and the "smooth barrier", given by equation (2.71), is a good approximation to the solution of the jellium–model (see section 5.1.1).

2. In the second step, the potential $U_2(\mathbf{r})$ is taken into account. At first, only the Green's function for the complete problem

$$\Big(E + \frac{\hbar^2}{2M}\nabla^2 - U_1(z) - U_2(\mathbf{r})\Big)G(\mathbf{r},\mathbf{r}',E) = \delta(\mathbf{r}-\mathbf{r}') \tag{2.75}$$

is determined by the Dyson equation. Then from this Green's function the multipole Green's function G_{lm} is constructed via equation (2.57).

2.5.3 Three–dimensional Green's function from a one–dimensional Green's function

As already stated, it is assumed that the one–dimensional Green's function G_1 is known in closed–form. For the various tip–vacuum–probe potentials and their one–dimensional Green's function see section 5.1.2, 5.1.3 and 5.1.1. Here it is shown how any multipole Green's function G_{lm} can be calculated from the corresponding one–dimensional Green's function G_1.

$G_{lm}(\mathbf{r},\mathbf{r}',E) \stackrel{\text{def}}{=} \mathcal{Y}_{lm}(\nabla')G(\mathbf{r},\mathbf{r}',E)$ satisfies the following equation:

$$\left(E + \frac{\hbar^2}{2M}\big(\partial_x^2 + \partial_y^2 + \partial_z^2\big) - U_1(z)\right)G_{lm}(\mathbf{r},\mathbf{r}',E) = \delta_{lm}(\mathbf{r}-\mathbf{r}'). \tag{2.76}$$

The Fourier transform of the Green's function $G_{lm}(\mathbf{r},\mathbf{r}',E)$ in the two coordinates x, y is given by

$$G_{lm}(\mathbf{r},\mathbf{r}',E) = \frac{1}{(2\pi\hbar)^2}\int_{\mathbb{R}^2}\tilde{G}_{lm}(p,q,z,z',E)e^{i\frac{p(x-x')}{\hbar}}e^{i\frac{q(y-y')}{\hbar}}dpdq. \tag{2.77}$$

It is well known that p and q are the momenta in x and y direction. Substituting equation (2.77) in (2.76) leads to

$$\int_{\mathbb{R}^2}\left(E - \frac{p^2+q^2}{2M} + \frac{\hbar^2}{2M}\partial_z^2 - U_1(z)\right)\tilde{G}_{lm}(p,q,z,z',E)e^{i\frac{p(x-x')}{\hbar}}e^{i\frac{q(y-y')}{\hbar}}dpdq = \mathcal{Y}_{lm}\left(\frac{\partial}{\partial\mathbf{r}'}\right)\int_{\mathbb{R}^2}\delta(z-z')e^{i\frac{p(x-x')}{\hbar}}e^{i\frac{q(y-y')}{\hbar}}dpdq.$$

This can be further simplified to

$$\left(E-\frac{p^2+q^2}{2M}+\frac{\hbar^2}{2M}\partial_z^2-U_1(z)\right)\tilde{G}_{lm}(p,q,z,z',E)=\mathcal{Y}_{lm}\left(\frac{p}{i\hbar},\frac{q}{i\hbar},\partial_{z'}\right)\delta(z-z'). \tag{2.78}$$

By comparison of this equation with the defining equation for $G_1(z,z',E-\frac{p^2+q^2}{2m})$ it is found that

$$\mathcal{Y}_{lm}\left(\frac{p}{i\hbar},\frac{q}{i\hbar},\partial_{z'}\right)G_1\left(z,z',E-\frac{p^2+q^2}{2M}\right)=\tilde{G}_{lm}(p,q,z,z',E). \tag{2.79}$$

Equation (2.79) states that the momentum Green's function (in x, y–direction) can be determined directly from the one–dimensional Green's function $G_1(z,z',E)$. The basic reason why this could be derived is that the potential $U_1(z)$ does not depend on x, y. It should be stated that there is no limitation on $\mathcal{Y}_{lm}$. Especially, they do not need to be translationally symmetric in the x, y direction (that is equation (2.79) is also true for $m\neq 0$). Substituting equation (2.79) in (2.77) leads to

$$G_{lm}(\mathbf{r},\mathbf{r}',E)=\frac{1}{(2\pi\hbar)^2}\int_{\mathbb{R}^2}\mathcal{Y}_{lm}\left(\frac{p}{i\hbar},\frac{q}{i\hbar},\partial_{z'}\right)G_1\left(z,z',E-\frac{p^2+q^2}{2M}\right)$$
$$e^{i\frac{p(x-x')}{\hbar}}e^{i\frac{q(y-y')}{\hbar}}dpdq.$$

To further simplify this equation, a variable transformation to cylindrical coordinates that reflect the symmetry of the problem is necessary. The new variables k, θ, ρ, ϕ are defined as follows:

$$\frac{p}{\hbar}\overset{\text{def}}{=}k\cos\theta \quad , \qquad \frac{q}{\hbar}\overset{\text{def}}{=}k\sin\theta \tag{2.80}$$

$$(x-x')\overset{\text{def}}{=}\rho\cos\phi \quad \text{and} \quad (y-y')\overset{\text{def}}{=}\rho\sin\phi \tag{2.81}$$

$$\Longrightarrow \quad k^2=\frac{p^2}{\hbar^2}+\frac{q^2}{\hbar^2} \quad \text{and} \qquad \rho^2=(x-x')^2+(y-y')^2. \tag{2.82}$$

With these definitions, the three–dimensional Green's function can be written as

$$G_{lm}(\mathbf{r},\mathbf{r}',E)=\frac{1}{(2\pi)^2}\int_0^\infty\int_0^{2\pi}\mathcal{Y}_{lm}\left(\frac{k\cos\theta}{i},\frac{k\sin\theta}{i},\partial_{z'}\right)G_1\left(z,z',E-\frac{\hbar^2k^2}{2M}\right)$$
$$e^{ik\rho\cos(\theta-\phi)}kd\theta dk. \tag{2.83}$$

Taking into account the structure of the $\mathcal{Y}_{lm}$ as given in [52] yields:

$$\begin{aligned}\mathcal{Y}_{lm}\Big(\frac{k\cos\theta}{i},\frac{k\sin\theta}{i},\partial_{z'}\Big) &= \frac{\sqrt{(2l+1)(l-m)!(l+m)!}}{\sqrt{4\pi}2^l l!}\\ &\sum_{\substack{c-a=m\\ a+b+c=l\\ a,b,c\in\mathbb{Z}_0^+}} \frac{l!}{a!b!c!}\Big(\frac{k\cos\theta}{i}-i\frac{k\sin\theta}{i}\Big)^a(2\partial_{z'})^b(-1)^c\Big(\frac{k\cos\theta}{i}+i\frac{k\sin\theta}{i}\Big)^c =\\ &\frac{\sqrt{(2l+1)(l-m)!(l+m)!}}{\sqrt{4\pi}2^l l!}\Big(\frac{k\cos\theta}{i}+i\frac{k\sin\theta}{i}\Big)^m\\ &\sum_{\substack{c-a=m\\ a+b+c=l\\ a,b,c\in\mathbb{Z}_0^+}} \frac{l!}{a!b!c!}\bigg(\Big(\frac{k\cos\theta}{i}\Big)^2+\Big(\frac{k\sin\theta}{i}\Big)^2\bigg)^a(2\partial_{z'})^b(-1)^c.\end{aligned} \tag{2.84}$$

The term

$$\bigg(\Big(\frac{k\cos\theta}{i}\Big)^2+\Big(\frac{k\sin\theta}{i}\Big)^2\bigg)^a=(-1)^a k^{2a}$$

is independent from θ. Considering only the integral over θ in equation (2.83), in other words collecting all θ dependent terms, leads to:

$$\begin{aligned}&\int_0^{2\pi}\Big(\frac{k\cos\theta}{i}+i\frac{k\sin\theta}{i}\Big)^m e^{ik\rho\cos(\theta-\phi)}d\theta =\\ &(ik)^m\int_0^{2\pi} e^{im\theta}e^{ik\rho\cos(\theta-\phi)}d\theta =\\ &(ik)^m e^{im\phi}\int_0^{2\pi} e^{im(\theta-\phi)}e^{ik\rho\cos(\theta-\phi)}d\theta =\\ &(-k)^m(2\pi)e^{im\phi}J_m(k\rho).\end{aligned} \tag{2.85}$$

In the last step the identity [1] 9.1.21 has been used:

$$\frac{i^m}{2\pi}\int_0^{2\pi} e^{im\theta}e^{ik\rho\cos\theta}d\theta = J_m(k\rho). \tag{2.86}$$

Substituting all these simplifications into equation (2.83) leads to

$$\begin{aligned} G_{lm}(\mathbf{r},\mathbf{r}',E) = \frac{1}{2\pi}\int_0^\infty \frac{\sqrt{(2l+1)(l-m)!(l+m)!\pi}}{\sqrt{4\pi}2^l l!} e^{im\phi}k^m J_m(k\rho) \\ \sum_{\substack{c-a=m \\ a+b+c=l \\ a,b,c\in\mathbb{Z}_0^+}} \frac{l!}{a!b!c!} k^{2a}(2\partial_{z'})^b G_1\left(z,z',E-\frac{\hbar^2k^2}{2M}\right)kdk = \\ \frac{\sqrt{(2l+1)(l-m)!(l+m)!}}{\pi^{\frac{3}{2}}2^{l+2}} e^{im\phi} \\ \sum_{\substack{c-a=m \\ a+b+c=l \\ a,b,c\in\mathbb{Z}_0^+}} \frac{1}{a!b!c!}\int_0^\infty k^{2a+m+1} J_m(k\rho)(2\partial_{z'})^b G_1\left(z,z',E-\frac{\hbar^2k^2}{2M}\right)dk. \end{aligned} \tag{2.87}$$

For $m = 0$, this equation is independent from ϕ, as expected, since in this case the source term also exhibits rotational symmetry.

As a very important special case, the direct connection between one–dimensional Green's function and three–dimensional Green's function can be established:

$$G(\mathbf{r},\mathbf{r}',E) = \sqrt{4\pi}G_{00}(\mathbf{r},\mathbf{r}',E) = \frac{1}{2\pi}\int_0^\infty kJ_0(k\rho)G_1\left(z,z',E-\frac{\hbar^2k^2}{2M}\right)dk. \tag{2.88}$$

Thus the multipole or the three–dimensional Green's function is given by an one–dimensional integration. This integration must be solved numerically in almost all presented simulations. For details of the numerical evaluation of this so–called "Hankel transform", see section 5.2.

2.5.4 Zero–range potentials

The second part of the potential $U(\mathbf{r})$, that is $U_2(\mathbf{r})$, should account for the contribution of individual lattice atoms. As a possible approximation for this potential, so–called zero–range potentials can be used:

$$U_2(\mathbf{r}) = \sum_i u_i \delta(\mathbf{r}-\mathbf{r}_i)\partial_{|\mathbf{r}-\mathbf{r}_i|}|\mathbf{r}-\mathbf{r}_i|. \tag{2.89}$$

A pure delta function would not lead to scattering in three–dimensions. Regularised δ-functions or Fermi pseudopotentials are required in order to make

the Schrödinger equation well behaved [11, 67]. Still, the Green's function $G(\mathbf{r}, \mathbf{r}', E)$ for the complete problem

$$\Big(E + \frac{\hbar^2}{2M}\nabla^2 - U_1(z) - U_2(\mathbf{r})\Big)G(\mathbf{r}, \mathbf{r}', E) = \delta(\mathbf{r} - \mathbf{r}') \tag{2.90}$$

must be determined. The Green's function $G^{\mathrm{w}}(\mathbf{r}, \mathbf{r}', E)$ of the reduced problem

$$\Big(E + \frac{\hbar^2}{2M}\nabla^2 - U_1(z)\Big)G^{\mathrm{w}}(\mathbf{r}, \mathbf{r}', E) = \delta(\mathbf{r} - \mathbf{r}') \tag{2.91}$$

is given by equation (2.88). In principle, the unknown Green's function can be calculated via the Dyson equation:

$$G(\mathbf{r}, \mathbf{r}', E) = G^{\mathrm{w}}(\mathbf{r}, \mathbf{r}', E) + \int_{\mathbb{R}^3} G(\mathbf{r}, \mathbf{r}'', E)U_2(\mathbf{r}'')G^{\mathrm{w}}(\mathbf{r}'', \mathbf{r}', E)\, d^3r''. \tag{2.92}$$

The order of the Green's function's in this equation may be unusual, but in fact, the order can be changed as has been proved in section 8.4. Due to the special structure of the potential $U_2(\mathbf{r})$, the Green's function $G(\mathbf{r}, \mathbf{r}', E)$ can be evaluated directly from the Dyson equation. The zero–range potentials turn the integral Dyson equation into an algebraic equation.

Simple substitution of equation (2.89) into equation (2.92) leads to:

$$G(\mathbf{r}, \mathbf{r}', E) = G^{\mathrm{w}}(\mathbf{r}, \mathbf{r}', E) + \sum_i G(\mathbf{r}, \mathbf{r}_i, E)u_i G^{\mathrm{w}}(\mathbf{r}_i, \mathbf{r}', E), \tag{2.93}$$

if $\mathbf{r}' \neq \mathbf{r}_i$, since then there exists a neighbourhood M of $\mathbf{r}_i$ so that $G^{\mathrm{w}}(\cdot, \mathbf{r}', E)$ is analytic in M. On the other hand, if $\mathbf{r}' = \mathbf{r}_j$ then

$$G(\mathbf{r}, \mathbf{r}_j, E) = G^{\mathrm{w}}(\mathbf{r}, \mathbf{r}_j, E) + \sum_i G(\mathbf{r}, \mathbf{r}_i, E)u_i \mathbf{C}(E))_{ij}, \tag{2.94}$$

where the matrix elements of $\mathbf{C}(E)$ are given by

$$(\mathbf{C}(E))_{ij} \stackrel{\mathrm{def}}{=} \begin{cases} G^{\mathrm{w}}(\mathbf{r}_i, \mathbf{r}_j, E) & \text{for } i \neq j \\ \big[\partial_{|\mathbf{r}-\mathbf{r}_j|}|\mathbf{r} - \mathbf{r}_j|G^{\mathrm{w}}(\mathbf{r}, \mathbf{r}_j, E)\big]_{\mathbf{r}=\mathbf{r}_i} & \text{for } i = j \end{cases}. \tag{2.95}$$

Remark 3 If the single atoms were not modelled by regularised δ–functions, the real part of the diagonal elements of $\mathbf{C}(E)$ would diverge. Hence it would not be possible to assign the atoms different scattering strengths u_i.

For further calculations with equation (2.94), it is extremely convenient to rewrite it in matrix notation: Let $\mathbf{G}^T$ be the row vector

$$\mathbf{G}^T \stackrel{\mathrm{def}}{=} \Big(G(\mathbf{r}, \mathbf{r}_1, E), \ldots, G(\mathbf{r}, \mathbf{r}_n, E)\Big), \tag{2.96}$$

and

$$\mathbf{K}^T \stackrel{\text{def}}{=} \Big(G^{\text{w}}(\mathbf{r}, \mathbf{r}_1, E), \ldots, G^{\text{w}}(\mathbf{r}, \mathbf{r}_n, E) \Big), \tag{2.97}$$

and finally let the matrix $\mathbf{U}$ denote the following diagonal matrix:

$$\mathbf{U} \stackrel{\text{def}}{=} \text{diag}(u_1, u_2, \ldots, u_n). \tag{2.98}$$

With these definitions it is easily verified that equation (2.94) can be rewritten as:

$$\mathbf{G}^T = \mathbf{K}^T + \mathbf{G}^T \mathbf{U} \mathbf{C}(E). \tag{2.99}$$

Applying linear algebra, equation (2.99) is immediately solved:

$$\mathbf{G}^T = \mathbf{K}^T \Big(\mathbf{1} - \mathbf{U}\mathbf{C}(E) \Big)^{-1}. \tag{2.100}$$

By substituting this relationship in equation (2.93), it is immediately found that:

$$G(\mathbf{r}, \mathbf{r}', E) = G^{\text{w}}(\mathbf{r}, \mathbf{r}', E) + \sum_{i,j=1}^{n} G^{\text{w}}(\mathbf{r}, \mathbf{r}_i, E)(\mathbf{T}(E))_{ij} G^{\text{w}}(\mathbf{r}_j, \mathbf{r}', E), \tag{2.101}$$

where the so–called T–matrix $\mathbf{T}(E)$ is given by

$$\mathbf{T}(E) = \big(\mathbf{1} - \mathbf{U}\mathbf{C}(E) \big)^{-1} \mathbf{U} = \big(\mathbf{U}^{-1} - \mathbf{C}(E) \big)^{-1}. \tag{2.102}$$

2.5.5 Total elastic cross section of zero–range potentials

Until now, the parameters u_i have been only considered as a measure for the strength of the regularised delta potential. In this section it will be shown that the u_i directly determine the total cross section of the regularised delta potential. From equation (4.10) the scattering amplitude $f(\mathbf{k}, \mathbf{k}')$ can be directly derived since

$$\psi(\mathbf{r}) = -\frac{1}{(2\pi\hbar)^{\frac{3}{2}}} f(\mathbf{k}, \mathbf{k}') \frac{e^{ikr}}{r} + \frac{e^{i\mathbf{k}\mathbf{r}}}{(2\pi\hbar)^{\frac{3}{2}}}. \tag{2.103}$$

(see for instance [4, 28, 55]). The scattering amplitude is thus given by:

$$f(\mathbf{k}, \mathbf{k}') = -\frac{2Mu}{2Muik + 4\pi\hbar^2} \tag{2.104}$$

Since the scattering amplitude in forward direction and the total cross section are directly related by the optical theorem

$$\text{Im}\, f(\mathbf{k}, \mathbf{k}) = \frac{k\sigma_{\text{tot}}}{4\pi}, \tag{2.105}$$

the total elastic cross section of the regularised delta potential is:

$$\sigma_{\text{tot}} = \frac{4\pi}{k^2 + \left(\frac{2\pi\hbar^2}{Mu}\right)^2}. \tag{2.106}$$

Since the adatoms are usually very close to the tunnelling exit of the electrons, the energy of the electrons is almost zero. Thus in this approximation the total cross section is given by:

$$\sigma_{\text{tot}} = \frac{(Mu)^2}{\pi\hbar^4}. \tag{2.107}$$

2.5.6 Generalisation of the model to include multipoles

The T–matrix equation (2.101) must now be extended to multipole sources. For this purpose, the following property of the Green's function G^{w} is very important: G^{w} is symmetric in the spatial arguments:

$$G^{\text{w}}(\mathbf{r}, \mathbf{r}', E) = G^{\text{w}}(\mathbf{r}', \mathbf{r}, E). \tag{2.108}$$

This can be easily seen from equation (2.31) and (2.88). From this symmetry, the following important feature of the multipole Green's function can be derived:

$$G^{\text{w}}_{lm}(\mathbf{r}, \mathbf{r}', E) \stackrel{\text{def}}{=} \mathcal{Y}_{lm}\Big(\frac{\partial}{\partial \mathbf{r}'}\Big) G^{\text{w}}(\mathbf{r}, \mathbf{r}', E) = \mathcal{Y}_{lm}\Big(\frac{\partial}{\partial \mathbf{r}'}\Big) G^{\text{w}}(\mathbf{r}', \mathbf{r}, E). \tag{2.109}$$

From expression (2.10) the multipole current is thus given by:

$$\begin{aligned} J_{lm}(E) = \lim_{\mathbf{r}' \to \mathbf{r}} (-1)^m \mathcal{Y}_{lm}\Big(\frac{\partial}{\partial \mathbf{r}'}\Big) \mathcal{Y}_{l-m}\Big(\frac{\partial}{\partial \mathbf{r}}\Big) G^{\text{w}}(\mathbf{r}, \mathbf{r}', E) + \\ (-1)^m \sum_{j,k=1}^{n} G^{\text{w}}_{l-m}(\mathbf{r}_j, \mathbf{r}, E) (\mathbf{T}(E))_{jk} G^{\text{w}}_{lm}(\mathbf{r}_k, \mathbf{r}', E). \end{aligned} \tag{2.110}$$

This important relationship is derived from equation (2.10) and the fact that

$$\mathcal{Y}^*_{lm}(z) = (-1)^m \mathcal{Y}_{l-m}(z). \tag{2.111}$$

In equation (2.110), the multipole current $\mathcal{Y}_{l-m}(\partial_{\mathbf{r}}) G^{\text{w}}_{lm}(\mathbf{r}, \mathbf{r}', E)$ appears. The evaluation of this term is similar to the evaluation of $G^{\text{w}}_{lm}(\mathbf{r}, \mathbf{r}', E)$. The exact relationship is presented in section 5.3.

Chapter 3

Basic numerical results

This chapter shows a multitude of simulated STM images, and thus illustrates that a broad spectrum of setups can be calculated by this simulation. Starting with simple metallic surfaces, it will be demonstrated that this simulation is capable of reproducing the high corrugation observed on closed packed surfaces. This high corrugation could not be predicted by the original theory of Tersoff–Hamann [60, 61]. (Due to this shortcoming, several extensions to the Tersoff–Hamann theory have been proposed in the past.) Next, the simulation of quantum corrals is addressed. From the resulting images a basic interpretation of the corral images can be already derived (section 3.5). In the following sections 3.6, 3.7 and 3.8, the effect of various parameters of the theory on the STM images is analysed. The chapter concludes with the presentation of some unusual corrals which also illustrate the previously developed interpretation.

3.1 STM corrugation pictures of simple metallic surfaces

At first, it must be verified whether this model is capable of reproducing the STM corrugation pictures of simple metals like copper silver or gold. It is one of the most distingushed features of the STM that it can resolve single adatoms even in closed packed surfaces, as Ag(111) for instance. Such a measurement is done at very low temperatures, more precisely, at about 4K. Since the STM is operated in a low bias voltage regime ($V \approx 10\text{mV}$), the approximation (2.17) seems valid. The *exact* tip surface distance (3Å-7Å) is not experimentally accessible with the same precision with which relative height changes of the tip can be measured. But it is known that the influence of the STM–tip on the probe is not negligible. This can be seen in the

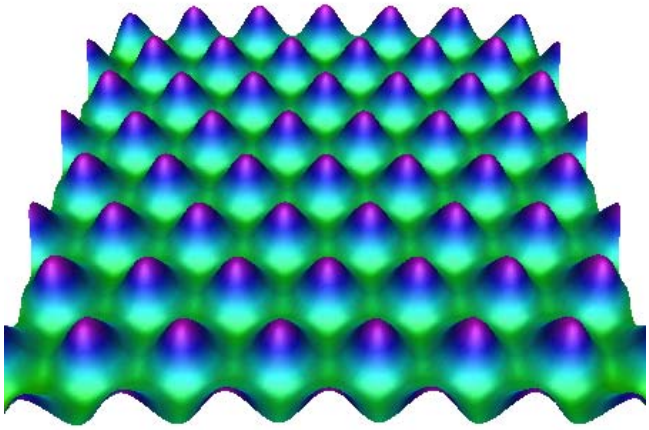

Figure 3.1: This is the resulting STM image for a silver surface. Here, the silver surface is viewed by an s–tip. The Ag(111) surface has a nearest neighbour distance of 2.89Å. The model to describe this surface uses the following parameters: $u_i = -27.6\text{Å}^3\text{eV}$, $E = 0\text{eV}$ at the tunnel exit. The resulting corrugation is 0.05Å.

following example.

The same area of a sample is scanned twice, where the scanning directions of the two scans are different. These two measurements are done several times with different angles between the scan direction of the first and second scan. The second scan is always performed in the same absolute direction. For certain samples, the STM pictures of the second scan are not identical, although they are all done in the same direction. They obviously depend on the scanning direction of the first scan. Thus, the first scan must have influenced the surface structure of the probe. In this case, the influence of the first scan even changes the stable surface configuration. For more details, see for instance [19].

At first, an s–tip (local rotational symmetric emission) is used in the following model. In this case, equation (2.64) reduces to

$$\Big(E + \frac{\hbar^2}{2M}\nabla^2 - U(\mathbf{r})\Big)\phi(\mathbf{r}, \mathbf{r}', E) = \lambda_{00}\delta_{00}(\mathbf{r} - \mathbf{r}'). \tag{3.1}$$

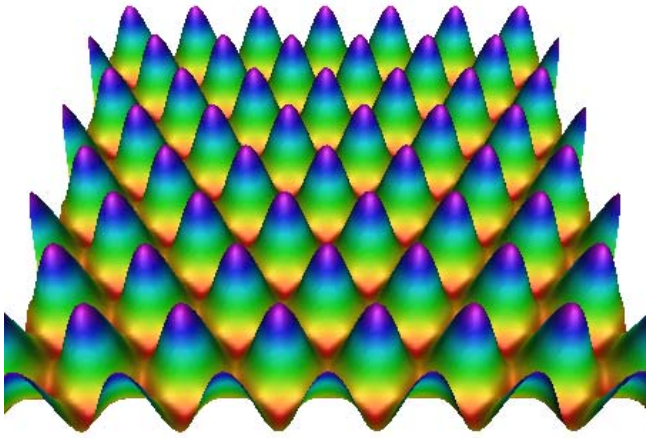

Figure 3.2: The same Ag(111) surface as in figure 3.1. The only difference is that this time, the surface is viewed by an d_{z^2}–tip. The setup is identical to the previous one in figure 3.1; thus, the parameters are: $u_i = -27.6\text{Å}^3\text{eV}$, $E = 0\text{eV}$ at the tunnel exit. The resulting corrugation (0.25Å) is five times larger then in figure 3.1.

As already mentioned in section 2.5, the potential is split into the contribution from single atoms $U_2(\mathbf{r})$ and a mean tip–vacuum–probe potential $U_1(z)$. The latter can be calculated within the jellium–model.

To simulate a simple metallic surface, the potential U_2 is chosen as a slab of 337 zero–range potentials. These zero–range potentials are arranged on fcc lattice positions of silver with a nearest neighbour distance of 2.89Å. The slab has a radius of 19Å and consists of 2 layers with a relative distance of 2.36Å. A relatively small 20Å·20Å part in the centre of the slab is then used for the STM corrugation picture. The size of the slab must be chosen in such a way that edge effects are negligible for the region that is selected for measurement.

The background potential is a triangular barrier with a slope $F = 1\text{eV/Å}$. Although this potential is not too realistic, it will be shown that the STM pictures are not very sensitive to the various background potentials, as long as they have similar barrier penetration probabilities (see [12]). Hence the

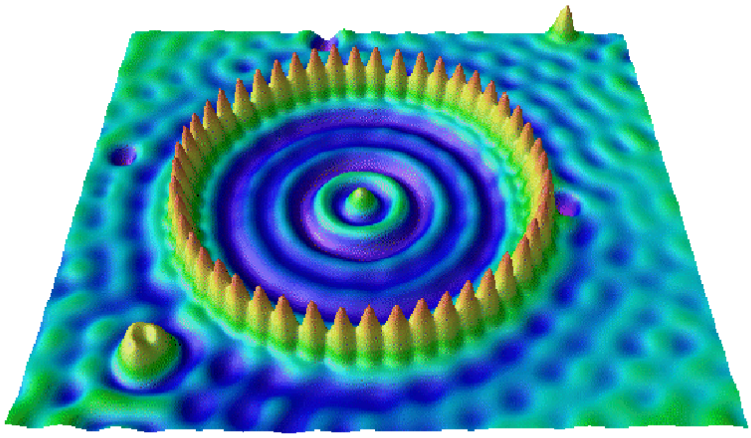

Figure 3.3: Experimental STM image of a quantum corral. The ring of 48 adatoms is clearly visible. There is no adatom in the centre of the corral. Outside the ring some artifacts can be seen. Published by IBM, Almaden: image gallery.

potential $U(\mathbf{r})$ is given by

$$U(\mathbf{r}) = -F \cdot z + \sum_j u_j \delta(\mathbf{r} - \mathbf{r}_j) \partial_{|\mathbf{r}-\mathbf{r}_j|} |\mathbf{r} - \mathbf{r}_j|. \tag{3.2}$$

The parameter u_j can be directly related to the total cross section of the zero–range potentials as given by (2.106).

Although the lattice structure is reproduced by the s–tip measurement of the Ag(111) surface, the observed corrugation for this surface is not the experimental corrugation. In the simulation (see figure 3.1), a corrugation of 0.05Å is observed while the experimental corrugation is approximately 0.2Å. To explain these high corrugations theoretically, tips with d–orbital characteristics are essential. Measuring the same surface with a d–tip (see figure 3.2) leads to a drastically increased corrugation of 0.25Å. Thus the multipole tips or the emission characteristics of the tip material are essential to explain the high corrugations that are observed in experimental pictures. The use of multipole tips in order to explain the high corrugations and thus the high spatial resolutions has been extensively discussed (see for instance [8, 9, 54]). The direct application of these results to source theory is presented

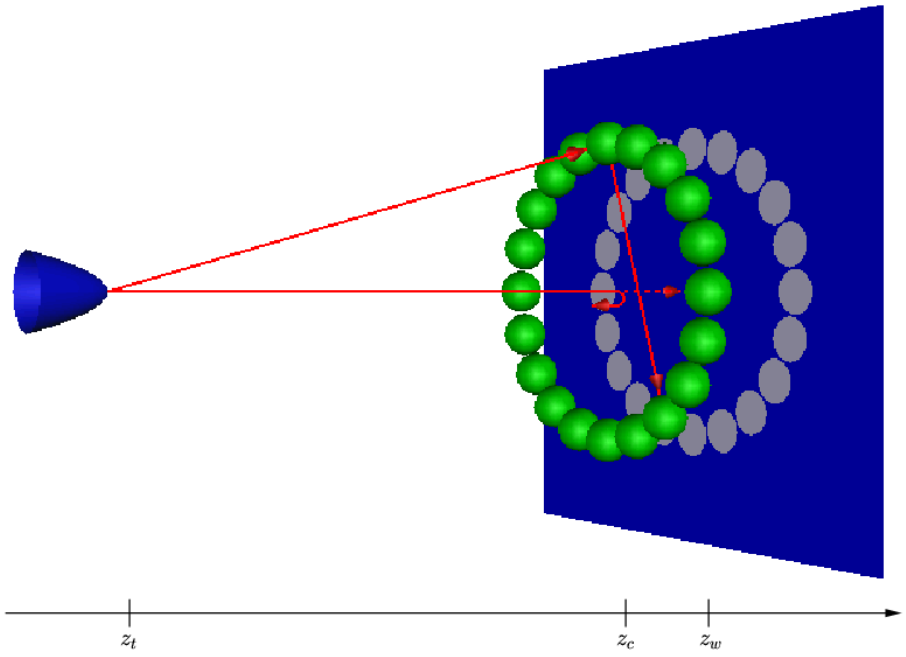

Figure 3.4: The setup to simulate quantum corrals. The partially reflecting surface that is necessary to introduce a two–dimensional electron gas is located at z_{w}. The corral adatoms are in front of this wall. The solution takes into account all possible scattering events between the adatoms and the partially reflecting surface.

in [10]. The influence of d–tips on STM images within the source theory is discussed in much more detail in [12].

3.2 Quantum corrals

Experimentally, a quantum corral is built on top of an atomically smooth surface, for instance Cu(111). The corral consists of 48 adatoms that are arranged in a circle on top of the smooth surface. The 48 adatoms are placed by the STM: The tip is driven towards an adatom, where an attractive voltage is applied. By this process the adatom is "torn off the surface". Then the STM tip with the adatom on top is driven to the desired location, where a repulsive voltage is applied so that the adatom is placed on the desired position. That this process is extremely cumbersome and littered with experimental difficulties is obvious. The STM is operated at approximately

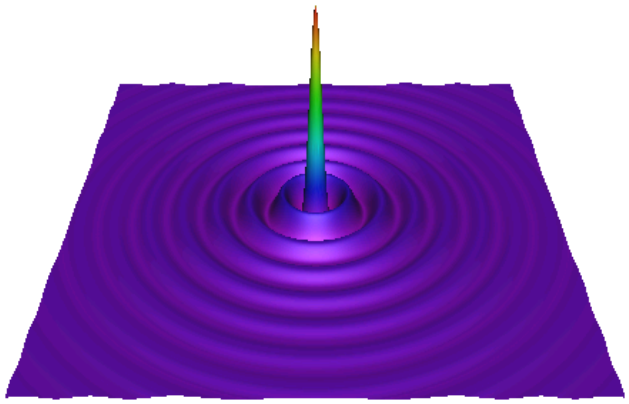

Figure 3.5: The STM image of a single adatom. The scanned area is $150 \times 150\text{Å}^2$. The intrinsic barrier with a strength of 60ÅeV that builds up the two–dimensional electron gas at the surface of the probe also causes the circular oscillations in the electronic density. It is 4.31Å away from the classical turning point, where the adatom is located. The slope of the potential is $F = 0.8\text{eV/Å}$. The tip is 4Å away from the adatom emitting electrons with an energy of -3.2eV. Thus the electrons reach the adatom with 0eV energy. As a reasonable value for the scattering length of the atom, 1.15Å was chosen. Thus the parameter $u_1 = +27.6\text{Å}^3\text{eV}$.

4K. Usually, iron adatoms are used for the construction of the corral. In the experiment, the diameter of the circle is $142,8$Å. Thus it is an extremely large object compared to the nearest neighbour distance of the substrate (see figure 3.3).

The Cu(111) surface is essential to see a standing wave pattern. The reason is that the Cu(111) surface has surface states of the Shockley type. That is, the surface state electrons cannot propergate in the direction perpendicular to the surface, since their momentum $\mathbf{k}$ is located in a band gap of the bulk material. This is sometimes referred to as a two–dimensional electron gas. Other surfaces and the crystal orientation with Shockley surface states are Ag(111) and Au(111). All these materials have been used to build corral–like structures. The scattering adatoms themselves can be replaced by others metals.

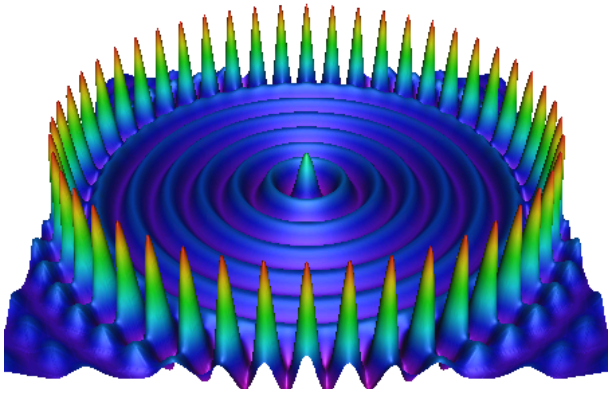

Figure 3.6: The STM image of a quantum corral. The corral consists of 48 adatoms on a circle with a radius of 71.3Å. All the other parameters are identical to those in figure 3.5. The corrugation in the above picture is 0.5Å when the conductivity is kept constant at $2.7 \cdot 10^{-8}$A/V. The wavelength of the oscillation is $\lambda = 10$Å.

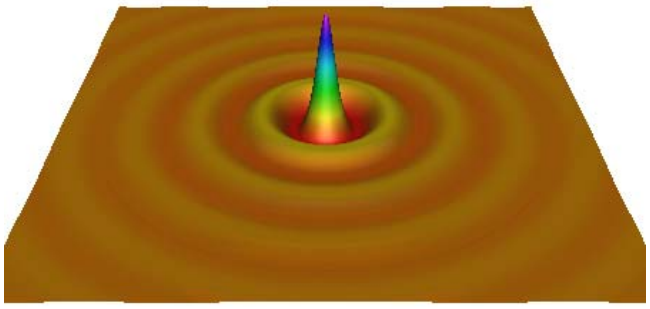

Figure 3.7: The STM image of a single adatom. The scanned area is 150×150Å^2. The intrinsic barrier with a strength of 60ÅeV that builds up the two–dimensional electron gas at the surface of the probe also causes the circular oscillations in the electronic density. It is 8.0Å away from the STM tip. The slope of the potential is $F = 1.0$eV/Å. The tip is 4Å away from the adatom emitting electrons with an energy of -0.3eV. As a reasonable value for the scattering length of the adatom, 1.15Å was chosen. Thus the parameter $u_1 = -27.6$Å^{3}eV. The setup is slightly different from the setup in figure 3.5, resulting in a modified STM image.

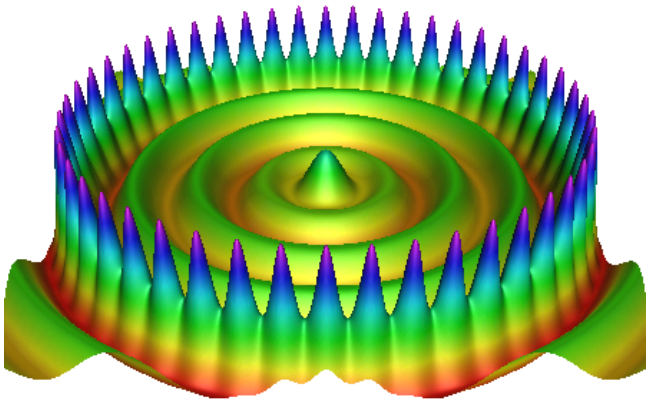

Figure 3.8: The STM image of a quantum corral. The corral consists of 48 adatoms on a circle with a radius of 71.3Å. All the other parameters are identical to those in figure 3.7. The corrugation in the above picture is 0.45Å when the conductivity is kept constant at $3.0 \cdot 10^{-7}$A/V. The wavelength of the oscillation is $\lambda = 20$Å. The parameters here differ from those in figure 3.6.

3.3 The model

The simulation of STM pictures of a quantum corral should of course be possible within the presented theoretical framework. Equation (2.64) will be the fundamental equation to calculate the pictures. What causes some trouble are the Shockley surface states. Without these, no standing wave pattern inside the corral is observed. Thus to model quantum corrals, the following potential

$$U(\mathbf{r}) = -F \cdot z + \alpha\delta(z - z_{\mathrm{w}}) + \sum_j u_j \delta(\mathbf{r} - \mathbf{r}_j)\partial_{|\mathbf{r}-\mathbf{r}_j|}|\mathbf{r} - \mathbf{r}_j| \qquad (3.3)$$

(illustrated in figure 3.4) is utilised. The potential $U(\mathbf{r})$ is of course only an approximation of the "real world". The only difference between the model (3.2) to simulate simple metallic surfaces and the model for quantum corrals (3.3) is the second term. This partially reflecting surface (that is, a surface that reflects only a portion and not all of the incident particles) is introduced to account for the two–dimensional electron gas [23]. (Those particles that are not reflected are transmitted.) Although the electrons cannot propagate into the bulk due to a band gap, inelastic processes eventually change the energy of the electron in such a way that it can contribute to the total current.

These processes that confine the electron onto the surface for a relatively long time are accounted for by a partially reflecting surface.

The introduction of the partially reflecting surface directly affects the calculation of the one–dimensional Green's function given by equation (2.73), since the potential $U_1(z)$ is now given by

$$U_1(z) = U_0(z) + \alpha\delta(z - z_{\mathrm{w}}), \tag{3.4}$$

where $U_0(z) = -F \cdot z$. The following derivation applies not only for the triangular barrier, but is valid in general. Let $U_0(z)$ be the potential in direction z (triangular, step or smooth barrier) and assume (as in equation 2.73) that the one–dimensional Green's function $G_1(z, z', E)$

$$\Big(E + \frac{\hbar^2}{2M}\partial_z^2 - U_0(z)\Big)G_1(z, z', E) = \delta(z - z') \tag{3.5}$$

is known. From this Green's function $G_1(z, z', E)$, the one–dimensional Green's function ${G_1}^{\mathrm{w}}(z, z', E)$

$$\Big(E + \frac{\hbar^2}{2M}\partial_z^2 - U_0(z) + \alpha\delta(z - z_{\mathrm{w}})\Big){G_1}^{\mathrm{w}}(z, z', E) = \delta(z - z') \tag{3.6}$$

can be constructed. The construction is for instance presented in [35]. The Dyson equation results in the equation:

$${G_1}^{\mathrm{w}}(z, z', E) = G_1(z, z', E) + \alpha \int_{-\infty}^{\infty} G_1(z, \tilde{z}, E)\delta(\tilde{z} - z_{\mathrm{w}}){G_1}^{\mathrm{w}}(\tilde{z}, z', E)\, d\tilde{z}. \tag{3.7}$$

Setting $z = z_{\mathrm{w}}$ gives:

$${G_1}^{\mathrm{w}}(z_{\mathrm{w}}, z', E) = G_1(z_{\mathrm{w}}, z', E) + \alpha G_1(z_{\mathrm{w}}, z_{\mathrm{w}}, E){G_1}^{\mathrm{w}}(z_{\mathrm{w}}, z', E). \tag{3.8}$$

From this condition ${G_1}^{\mathrm{w}}(z_{\mathrm{w}}, z', E)$ can be easily derived:

$${G_1}^{\mathrm{w}}(z_{\mathrm{w}}, z', E) = \frac{G_1(z_{\mathrm{w}}, z', E)}{1 - \alpha G_1(z_{\mathrm{w}}, z_{\mathrm{w}}, E)}. \tag{3.9}$$

From equation (3.7) and (3.9), the one–dimensional Green's function ${G_1}^{\mathrm{w}}(z, z', E)$ is easily calculated:

$${G_1}^{\mathrm{w}}(z, z', E) = G_1(z, z', E) + \frac{G_1(z, z_{\mathrm{w}}, E)G_1(z_{\mathrm{w}}, z', E)}{\frac{1}{\alpha} - G_1(z_{\mathrm{w}}, z_{\mathrm{w}}, E)}. \tag{3.10}$$

The behaviour of the one–dimensional Green's function (3.10) has been discussed many times before (for example [44, 14]). Although the one–dimensional

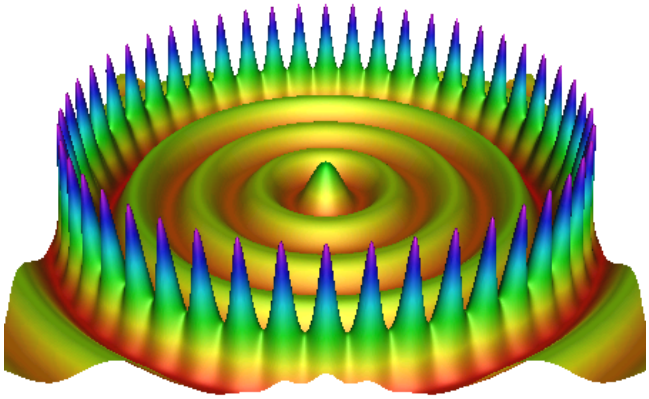

Figure 3.9: The STM image of a quantum corral. Here, only the diagonal elements of the T–matrix (2.102) are different from zero. This picture results from superposing 48 times the image 3.7. All the other parameters are identical to those in figure 3.8. The corrugation in the above picture is 0.45Å when the conductivity is kept constant at $3.0 \cdot 10^{-7}$A/V. The wavelength of the oscillation is $\lambda = 20$Å.

Green's function $G_1^{\mathrm{w}}(z, z', E)$ as given by equation (3.10) cannot be Hankel transformed analytically as in equation (2.87) or (2.88), still, the denominator in equation (3.10) will permit some quite accurate approximations of the three–dimensional Green's function. This is because the structure of the Green's function $G_1^{\mathrm{w}}(z, z', E)$ is mostly determined by the zeros of the denominator. The parameter α is chosen positive, so that the potential $\alpha\delta(z - z_{\mathrm{w}})$ represents a wall and not a ditch. Furthermore, α is real and thus there are no inelastic scattering processes. The fact that α and also u_i are real is an additional restriction which is not imposed by the underlying mathematical model. Thus the model presented here could be very easily extended into a complex parameter space without changing the presented equations. As shown in figure 3.4, the adatoms are positioned in a plane parallel to the repulsive wall. Although this is a rather crude approximation of the underlying effective potential, it turns out that this approximation is sufficient to produce the typical STM–images of quantum corrals.

3.4 The results

A numerical simulation shows all the characteristic features of quantum corrals seen in experimental pictures. The major difficulty for a numerical simu-

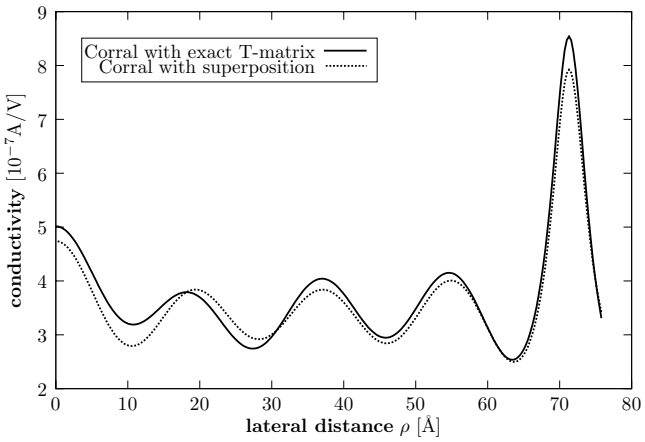

Figure 3.10: Here, the direct comparison of figure 3.8 with figure 3.9 is shown. This is a constant height scan with a tip–adatom distance of 4Å. The figure shows that the superposition approximation is a zero order approximation which is capable of reproducing the *wavelength* of the oscillation in the electronic density. But the figure also shows the limitations of the superposition approximation, since the approximated *current profile* significantly deviates from the exact calculation.

lation is the accurate evaluation of the three–dimensional Green's function by equation (2.87). Several algorithms exist, but most of them lack the accuracy needed. The algorithm employed here is presented in section 5.2. Due to the simplicity of the model, these pictures can be calculated within minutes on a standard personal computer.

It is very interesting to study STM pictures not only of the quantum corral but also of a single adatom. From experiments it is well known (see [46]) that the typical oscillations occur not only in a ring of atoms, but also in the case of single atoms. Furthermore, the wavelengths of the electronic density oscillations produced by a single adatom are identical with the wavelengths appearing in a quantum corral. Although at first sight this detail seems unimportant, it shows that the wavelengths in a quantum corral have nothing to do with the radius of the corral. To emphasise the importance of the single adatom images, the figure pairs 3.5, 3.6 and 3.7, 3.8 are shown. It should be mentioned that there is no adatom in the centre of the ring. The maximum in the centre (shown in figures 3.6 and 3.8) results from the circular arrangement of the adatoms.

The standing wave patterns (for a single adatom as well as for a whole array of adatoms) are seen if and only if the surface of the probe harbours a two–

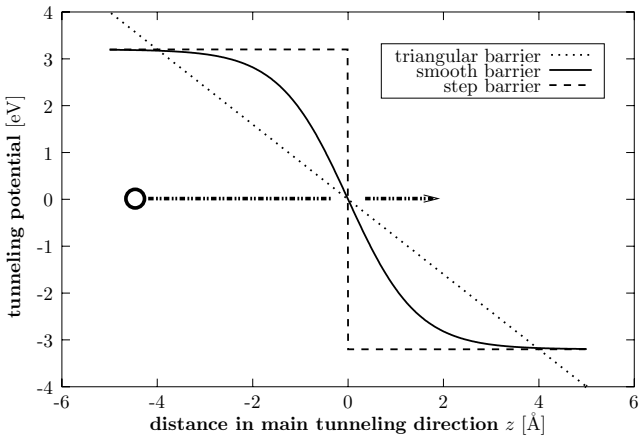

Figure 3.11: This figure shows the three different potential distributions used in this thesis. The step barrier is given by $3.2\text{eV/Å} \cdot \text{sign}(z)$. The triangular barrier is given by $-0.8\text{eV/Å} \cdot z$. The smooth barrier is given by $\frac{6.4\text{eV/Å}}{1-e^{1.37824\text{Å}^{-1}z}} - 3.2\text{eV}$. In this case, the parameters of the smooth barrier have been chosen so that the area between the step barrier and the triangular barrier is exactly halved.

dimensional electron gas. Since in the theory presented the two–dimensional electron gas results from the potential wall term $\alpha\delta(z-z_{\text{w}})$ in equation (3.4), the oscillations will disappear for $\alpha \to 0$.

From these pictures some basic understanding of the emerging wavelength can be already gained. It must be the $-F\cdot z+\alpha\delta(z-z_{\text{w}})$ term of the potential and the energy E of the electrons that determines the wavelengths. The only other parameter that might influence the wavelength of the corral is the strength u_j that is directly related to the total cross section of an adatom. But from the experiments it is known that the choice of the adatoms is not fixed, any material can be chosen. The adatoms can be replaced without any drastic changes of the STM image. This relative insensitivity of the STM images to the parameter u_j can also be reproduced theoretically (see section 4.2).

3.5 The superposition approximation

In the previous section, the strong correspondence between the wavelength of a single adatom and the wavelength for a circular arrangement has been pointed out. As a zero order approximation, one can try to interpret the

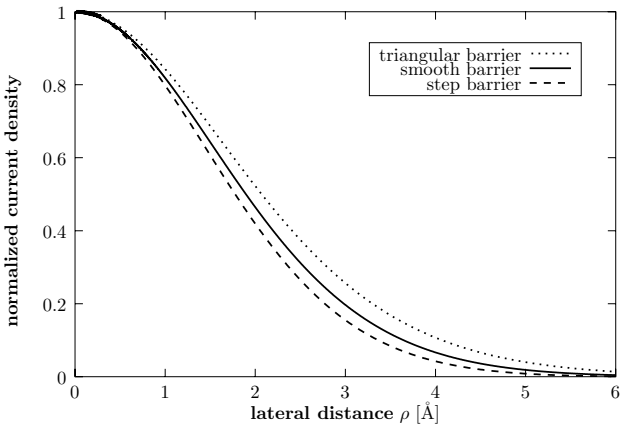

Figure 3.12: The resulting tunnelling spots at the position $z = 0$, that is, at the exit of the tunnel. These are the tunnelling spots for the different barriers shown in figure 3.11. Clearly, all the spots have a Gaussian shape. Furthermore, it can be seen that the step barrier leads to the smallest spot and thus to the highest resolution. This is followed by the smooth barrier, and finally, the triangular barrier.

corral pictures as mere superposition of 48 single adatom STM images. More precisely, in the T–matrix (equation (2.102)) all off diagonal elements are set to zero.

The resulting conductivity picture of an arbitrary setup of adatoms can be explained basically by simple superposition. Thus the standing wave pattern can be calculated not only for a circular arrangement of the adatoms, but for any arbitrary formation. In how far this zero order approximation is valid is shown in figure 3.8, 3.9 and 3.10. From the superposition approximation it is easy to predict when a maximum appears at the centre of the quantum corral. All experimental pictures show that the rings turn into rings of 48 bumps when the radius exceeds a certain limit, as it is shown in figure 3.6. Again, this can be explained by superposition. The reason why this superposition model is so useful is that the diagonal matrix elements of the T–matrix $\mathbf{T}(E)$ are the dominant ones. They are typically 100 times greater than the biggest off–diagonal term.

Although this approximation is able to reproduce the quantum corral qualitatively, it should be emphasised that there are some physical effects of a quantum corral that cannot be described by this approximation. For instance, there would be no Kondo mirage if the T–matrix were diagonal.

Since within the superposition approximation the standing wave pattern

of an arrangement of adatoms is reduced to the standing wave pattern of the individual adatoms, the understanding of the oscillations for a single adatom is essential. In other words, the interesting effect is the standing wave pattern that appears for *individual* adatoms as shown in figure 3.5 or 3.7 and not the whole corral of 48 adatoms. Calculating the STM image of a single adatom yields some useful insights. In this case, the T–matrix reduces to one complex number. Choosing u_1 so that $\mathbf{T}(E)$ is maximal will lead to maximal changes in conductivity. Indeed, it turns out that u_1 mainly determines how much the second summand in equation (2.101) is amplified. Thus the parameter u_1 has hardly any influence on qualitative conductivity pictures. However, it directly influences the observed corrugation amplitude.

Sometimes in scientific publications the standing wave pattern inside a quantum corral is attributed to an electron that is confined in a ring. As it is clear from the experimental data, this interpretation cannot be valid. Indeed, Heller has shown a decade ago that the electrons are *not* confined inside the corral [15]. Obviously, one cannot speak of the confinement of the electron if there is only an individual adatom present (at least, it cannot be confined in the direction parallel to the surface of the probe). Nonetheless, a standing wave pattern can be observed experimentally (for experimental images see [46]). In the present thesis it will be shown that the standing wave pattern is a result of electron confinement—however, the electrons are not confined in the direction *parallel* to the surface of the probe (x,y) but in the direction *perpendicular* to the surface (z). For details see section 4.3. The name "quantum corral" is thus misleading, but it has been nevertheless established due to historic reasons.

3.6 Comparison of different barriers

Since the mean background potential is not exactly known, its influence on the STM pictures must be studied. Although the tunnelling potential can be calculated within the jellium–model (see section 2.5.1), the precise form of the potential is not known. This potential does not depend only on the probe material but also on the position and material of the tip. In addition, the bias voltage has definitely an effect on the tunnelling potential. Since the experimental STM pictures look alike for a variety of different materials, tip positions and bias voltages, the precise shape of the tunnelling potential cannot have a great influence on the STM images. It could even be stated that if the STM were much more sensitive to the tunnelling barrier, it could hardly be used as a surface visualisation instrument. This relative stability of the STM images in spite of the changes of the tunnelling barrier must also

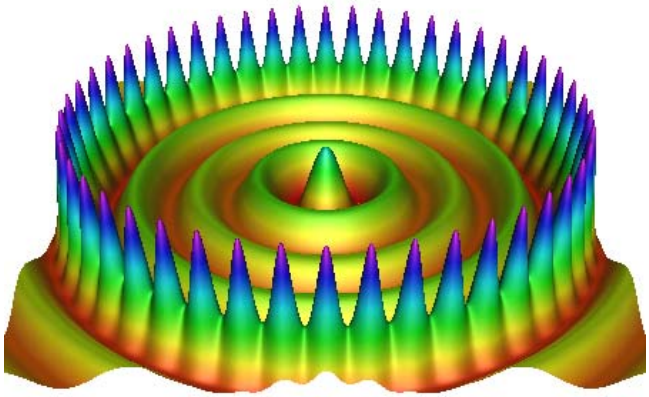

Figure 3.13: A smooth background barrier has been employed in the simulation of this quantum corral. The partially reflecting surface with a strength of 60ÅeV causes the circular oscillations in the electronic density. It is 8.5Å away from the STM tip. The parameters for the potential are: $V_0 = 7$eV, $\alpha = 0.8$Å^{-1}. The tip emitting electrons with an energy of 0.262eV is 4.5Å away from the adatom.

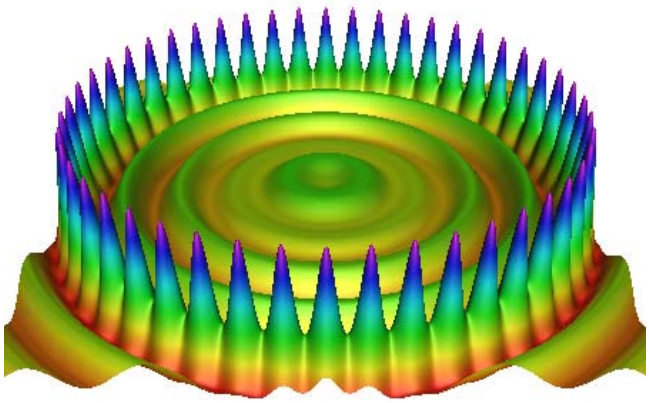

Figure 3.14: The same corral as in figure 3.8 with a slightly different energy. All parameters of the model are identical to those in figure 3.8 except for the energy of the emitted electrons. The tip emitting electrons with an energy of -0.242eV is 4Å away from the adatom. This slight energy shift turned the maximum in the centre of the corral into a plateau.

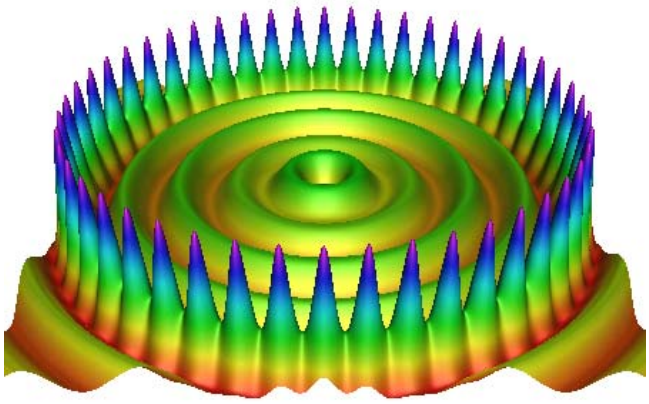

Figure 3.15: The same corral as in figure 3.8 with a slightly different energy. All parameters of the model are identical to those of figure 3.8 except for the energy of the emitted electrons. The tip emitting electrons with an energy of -0.246eV is 4Å away from the adatom. In this case, the energy shift turned the maximum in the centre of the corral into a minimum.

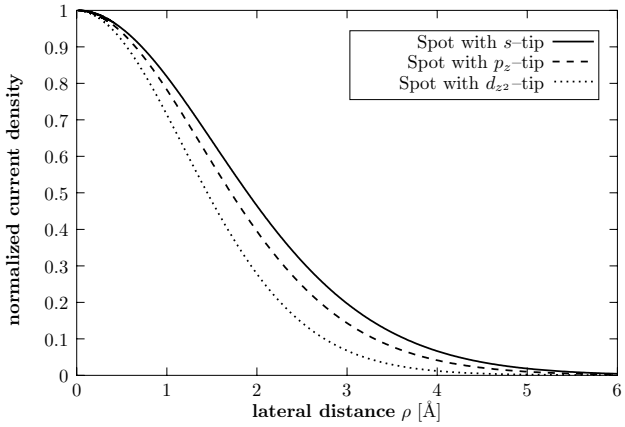

Figure 3.16: These are the resulting current distributions for the triangular barrier. Tips with different orbital emission characteristics are used. The d_{z^2}–tip gives the highest spatial resolution, while the s–tip has a broader tunnelling spot and thus a lower resultion. These spots explain the observed increase in corrugation from figure 3.1 to 3.2.

be seen theoretically.

Three different test–potential distributions are studied here. The potentials are shown in figure 3.11. The distributions are: a step potential, a triangular barrier, and the smooth barrier. A step potential is an often used zero order approximation. The triangular barrier would be the solution of the free electric field. And finally, the smooth barrier has one more free parameter than the other two. Basically, the slope in the origin can be adjusted. Here the parameters of the smooth barrier have been chosen so that the area between the step barrier and the triangular barrier is exactly halved.

In [12], the resulting current distributions for various potentials have been studied. So only the main results are recapitulated here:

The total current is approximately exponentially suppressed by increasing tunnelling distance. One of the most important quantities is the radius of the tunnelling spot, where the tunnelling spot is the area of the probe that is illuminated by the STM. The radius of the tunnelling spot determines the smallest structures that can be resolved. The resulting tunnelling spots for the different barriers in figure 3.11 are shown in figure 3.12. All these distributions have a Gaussian shape. The precise deviations of a Gaussian can be calculated as in [12]. This observation can be exploited theoretically in the minimum uncertainty model (see [10] for details). The step barrier leads to the smallest spot and thus to the highest resolution, whereas the triangle barrier has the worst resolution.

In how far different barriers affect the image of quantum corrals is shown in figure (3.13). There, the same corral as in picture 3.8 is shown, but a smooth barrier is used instead of a triangular barrier. Although the spots and thus the resolution of the STM changes slightly for the various potentials, the resulting STM pictures of the quantum corrals hardly change. This is due to the fact that the standing wave pattern inside the corrals has typically a wavelength of 10 to 20Å. These standing waves are thus much bigger than the typical spot of the STM, which is about 2Å in radius.

3.7 The energy dependence

The only parameter that is changed in this section is the energy of the emitted electrons. From equation (2.17) it can be seen that the energy of the emitted electrons is $\epsilon_F - eV$ in this approximation. Thus a change of the energy of the emitted electrons can be interpreted as a change of the bias voltage. From experiments it is known that the STM pictures of quantum corrals are quite sensitive to changes of the bias voltage (see for instance [18]). Typically, the STM image significantly changes when the bias voltage is changed by 10meV.

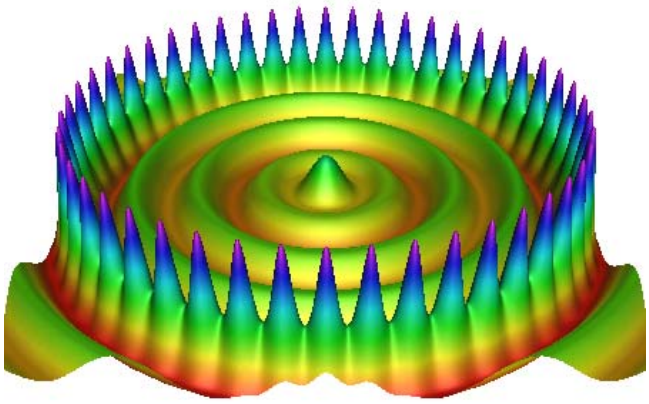

Figure 3.17: The same corral as in figure 3.8 except that here the quantum corral is scanned by an p_z–tip instead of an s–tip. All other parameters are identical to those in the setup for figure 3.8. At first sight, the two images seem to be identical. A detailed analysis reveals an increase in the corrugation above the adatom sites (see figure 3.19). The corrugation is 0.5Å when the conductivity is $2.7 \cdot 10^{-8}$A/V.

Figure 3.14 shows exactly the same corral as picture 3.8, except that the energy of the emitted electrons has been shifted from -0.3eV to -0.242eV. The maximum in the centre of the corral disappeared and instead, a plateau can be seen in the centre. The appearance of the plateau can be explained in terms of the superposition model (see section 3.4) in case the wavelength of the single adatom (shown in figure 3.7) changed due to the shift in the bias voltage. That the wavelength of a single adatom can be directly controlled by the bias voltage will be shown in section 4.3. If the energy of the electrons is further increased, this plateau can be turned into a minimum in the centre of the corral. This is shown in figure 3.15. Although in experimental publications there is a clear preference to present corrals that have a maximum in the centre, there are unpublished experimental pictures of quantum corrals with a minimum, plateau or anything in between. In the publication of Rieder [18], only the energy dependence of triangular corrals is studied. Rieder presents experimental evidence that these corrals are very sensitive to the change of the bias voltage, and thus it is no great surprise that circular corrals also show this sensitivity. From the superposition approximation the maximum in the centre of the corral can be easily understood: The standing wave pattern for a single adatom (as shown in figure 3.5 or 3.7) must have a

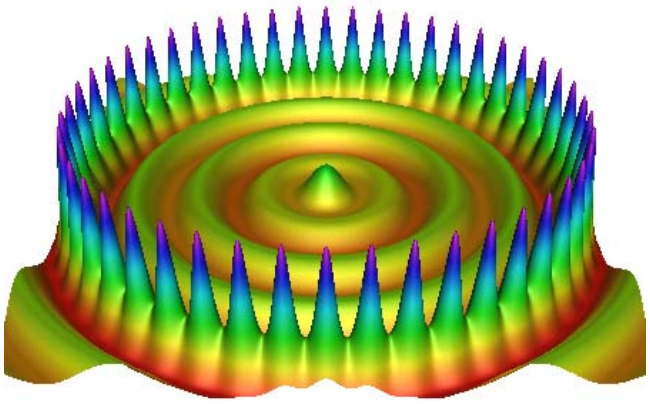

Figure 3.18: The same corral as in figure 3.8 except that here the quantum corral is scanned by an d_{z^2}–tip instead of an s–tip. All other parameters are identical to those in the setup for figure 3.8. At first sight, the two images seem to be identical. A detailed analysis reveals a drastic increase in the corrugation above the adatom sites (see figure 3.19). The corrugation is 0.8Å when the conductivity is $2.7 \cdot 10^{-8}$A/V.

maximum 71.4Å away from the adatom. When the ring of 48 adatoms is set up, then the 48 maxima interfere constructively in the centre of the corral.

3.8 The corral with different multipole tips

In section 3.1 it was shown that multipole tips are essential to reproduce the relatively high corrugation for smooth metal surfaces. Here only tips with s, p_z and d_{z^2} emission characteristics will be considered. The different resolutions that can be achieved with these tips can be illustrated by studying the tunnelling spot, as in section 3.6. In figure 3.16 the resulting spots for the three different multipole tips are shown. It is not surprising that the d_{z^2}–tip has the smallest tunnelling spot and thus the highest resolution. Until now in this thesis, all corrals have been simulated with an s–tip. In figure 3.17 and 3.18 the resulting STM image of a corral with a p_z and d_{z^2} tip is shown. The orbital character of the tip has no influence on the wavelength of the corral. However, the corrugation at the adatom sites is increased with increasing multipole. In figure 3.19, a cut from the centre of the corral to one of the adatom sites is shown. From this detailed picture it can be seen that the standing wave pattern is not influenced by the different multipole

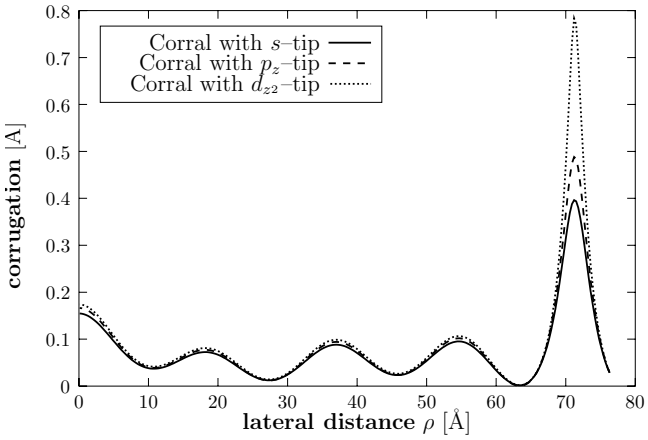

Figure 3.19: This figure shows the corrugation profiles of the image 3.8, image 3.17 and image 3.18. This direct comparison shows that the standing wave pattern is hardly affected by the different multipolarity of the tip. On the other hand, with higher orbital character of the tip, the corrugation above the adatom sites drastically increases.

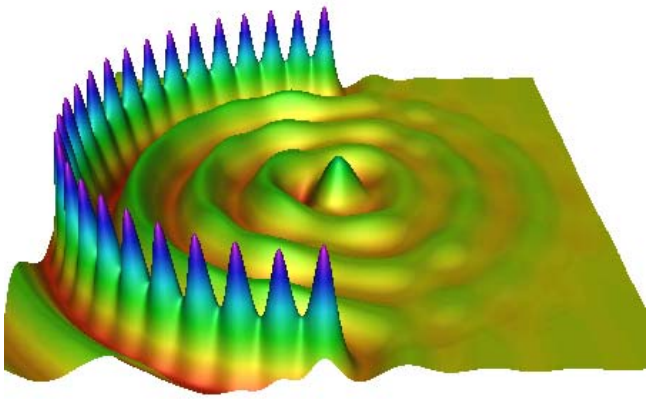

Figure 3.20: These is a half corral consisting of 25 adatoms. Otherwise, the setup is identical to the setup of figure 3.8. Although the electrons cannot be confined in the direction along the surface, a standing wave pattern is observed.

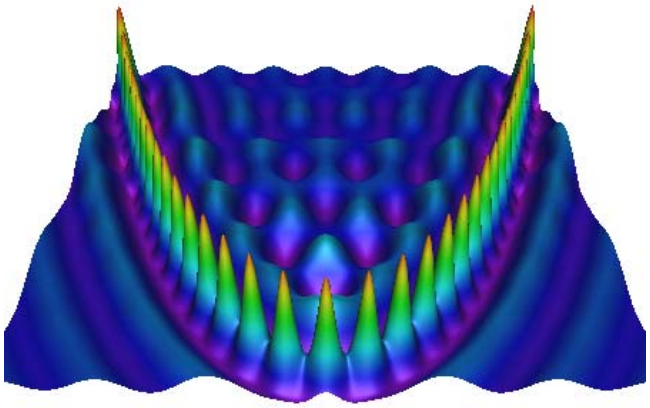

Figure 3.21: This is a parabola with the coefficients: $y = (35.65\text{Å})^{-1} \cdot x^2$. The 35 adatoms all have a nearest neighbour distance of 9.333Å. The physical setup is the "standard setup" of figure 3.8. A maximum can be observed in the focus of the parabola. Far from the vertex of the parabola, the oscillations of electronic density show a plane wave behaviour.

tips. Especially the d_{z^2} gives a high corrugation above the adatom sites.

3.9 Unusual corrals

After the publication of the experimental results for the original circular corral, a variety of other adatom arrangements have been studied. The most important ones are stadium like corrals, quadratic and triangular corrals. Experimentally, the adatoms cannot be placed on an arbitrary position on the probe surface. For an fcc surface, there is only an hexagonal mesh of possible adatom sites. This constraint does not apply for the theory presented here since it does not calculate the stability of an adatom configuration. Consequently, any adatom arrangement can be set up easily.

The first arrangement is a half corral. This half corral (figure 3.20) appears during the experimental construction process of the complete corral (see figure 1.2). It can be seen that even half corrals show already a maxi-

mum in the centre. That the electrons cannot be confined in the direction along the surface of the probe is obvious. Finally, a parabola arrangement is shown in picture 3.21. The nearest adatom distance is 9.333Å, which is identical to the nearest adatom distance in the circular corral.

Chapter 4

Interpretation

After presenting some simulated STM pictures, this chapter goes beyond the relatively simple approximations like the superposition approximation. In this chapter, a fundamental theoretical understanding for the model Hamiltonian is presented. At first, it will be discussed in how far different adatom types influence the STM images. Then an approximation is presented that links the theory to the two–dimensional theory of Heller [20]. In section 4.1 and section 4.2, it will be seen that the zero–range potentials can acquire not only attractive but also repulsive properties. In other words, an adatom can appear as hill as well as a hole in the STM images. That an adatom can in fact appear as a depression on the STM image has been shown for an oxygen atom absorbed on a metal surface [56]. This can happen since the STM does not give a direct image of the atomic geometry of the surface but rather, it maps the electronic structure.

4.1 Scattering properties of the regularised delta potential

Contrary to the scattering properties of the three–dimensional regularised delta potential, the bound state of this potential is well known. The three–dimensional regularised delta potential

$$U_2(\mathbf{r}) = u\delta(\mathbf{r})\partial_{|\mathbf{r}|}|\mathbf{r}| \tag{4.1}$$

has a bound state only for $u > 0$. It is given by:

$$\psi_b(\mathbf{r}) = \left(\frac{\kappa}{2\pi}\right)^{\frac{1}{2}} \frac{1}{|\mathbf{r}|} e^{-\kappa|\mathbf{r}|} \qquad \text{with} \qquad \kappa = \frac{2\pi\hbar^2}{Mu}. \tag{4.2}$$

The energy of this bound state is:

$$E = -\frac{\hbar^2}{2M}\kappa^2. \tag{4.3}$$

The most obvious setup to discuss the scattering properties of the regularised delta potential is to place the delta potential in the origin of a free potential $U_1(\mathbf{r}) = 0$. Thus the potential in the whole space is given by the regularised potential

$$U(\mathbf{r}) = U_1(\mathbf{r}) + U_2((r)) = u\delta(\mathbf{r})\partial_{|\mathbf{r}|}|\mathbf{r}|. \tag{4.4}$$

Now it can be studied how an incident free particle is scattered by this potential. In this case, the Lippmann-Schwinger equation is:

$$\psi(\mathbf{r}) = \frac{e^{i\mathbf{kr}}}{(2\pi\hbar)^{\frac{3}{2}}} - \frac{2M}{\hbar^2}\int \frac{e^{ik|\mathbf{r}-\mathbf{r}'|}}{4\pi|\mathbf{r}-\mathbf{r}'|}u\delta(\mathbf{r}')\partial_{|\mathbf{r}'|}|\mathbf{r}'|\psi(\mathbf{r}')d^3r'. \tag{4.5}$$

The convention $|\mathbf{x}| = x$ is used. To solve equation (4.5), the following ansatz is useful:

$$\psi(\mathbf{r}) = \alpha\frac{e^{ikr}}{r} + \frac{e^{i\mathbf{kr}}}{(2\pi\hbar)^{\frac{3}{2}}}. \tag{4.6}$$

Substituting equation (4.6) in equation (4.5) on the right hand side leads to

$$\psi(\mathbf{r}) = \frac{e^{i\mathbf{kr}}}{(2\pi\hbar)^{\frac{3}{2}}} - \frac{2Mu}{4\pi\hbar^2}\frac{e^{ikr}}{r}\left(ik\alpha + \frac{1}{(2\pi\hbar)^{\frac{3}{2}}}\right). \tag{4.7}$$

In the above derivation $\mathbf{kr} = kr\cos\phi$ is used, where ϕ is the angle between $\mathbf{k}$ and $\mathbf{r}$. Comparing the ansatz (4.6) and equation (4.7) leads to a simple equation for α:

$$\alpha = -\frac{2Mu}{4\pi\hbar^2}\left(ik\alpha + \frac{1}{(2\pi\hbar)^{\frac{3}{2}}}\right). \tag{4.8}$$

Thus

$$\alpha = -\frac{1}{(2\pi\hbar)^{\frac{3}{2}}}\frac{2Mu}{2Muik + 4\pi\hbar^2}. \tag{4.9}$$

So the scattering states of the regularised delta potential are given by:

$$\psi(\mathbf{r}) = -\frac{1}{(2\pi\hbar)^{\frac{3}{2}}}\frac{2Mu}{2Muik + 4\pi\hbar^2}\frac{e^{ikr}}{r} + \frac{e^{i\mathbf{kr}}}{(2\pi\hbar)^{\frac{3}{2}}}. \tag{4.10}$$

As usual the bound state is orthogonal to the scattering states:

$$\int \psi(\mathbf{r})\psi_b^*(\mathbf{r})d^3r = \left(\frac{\kappa}{2\pi}\right)^{\frac{1}{2}} \frac{1}{(2\pi\hbar)^{\frac{3}{2}}} \cdot \int_0^\infty \int_0^\pi \Big(-\frac{2Mu}{2Muik + 4\pi\hbar^2}\frac{e^{ikr}}{r} + e^{ikr\cos\phi}\Big)\frac{e^{-\kappa|\mathbf{r}|}}{|\mathbf{r}|} 2\pi r^2 \sin\phi \, d\phi dr = \left(\frac{\kappa}{2\pi}\right)^{\frac{1}{2}} \frac{1}{(2\pi\hbar)^{\frac{3}{2}}} \frac{2\pi(4\hbar^2\pi - 2Mu\kappa)}{(2\hbar^2\pi + ikMu)(k^2+\kappa^2)}. \tag{4.11}$$

With the definition of κ as given in equation (4.2) it is easily seen that the two states are orthogonal:

$$\int \psi(\mathbf{r})\psi_b^*(\mathbf{r})d^3r = 0. \tag{4.12}$$

A very interesting question is whether the three–dimensional regularised delta potential is attractive for negative or positive u? The usual definition for attractiveness of a potential is

$$U(\mathbf{r}) < 0 \quad \text{for all } \mathbf{r}. \tag{4.13}$$

This definition is not directly applicable in the case of a regularised delta potential. Another possible definition of an attractive potential is the increase of the number of particles in an area including the scattering potential. The number of particles N in a sphere of radius R around the regularised delta potential is given by:

$$N(u) = \int_0^R \int_0^\pi \int_0^{2\pi} \psi(\mathbf{r})\psi^*(\mathbf{r}) r^2 \sin\phi \, d\alpha d\phi dr. \tag{4.14}$$

The integrals involved in the above equation (4.14) are evaluated straight forward:

$$N(u) = \frac{1}{(2\pi\hbar)^3}\left(\frac{4\pi}{3}R^3 + \frac{2M\pi\Big(kMu^2\sin(2kR) - 4\pi\hbar^2 u\big(\sin(kR)\big)^2\Big)}{4\pi^2\hbar^4k^2 + M^2u^2k^4}\right). \tag{4.15}$$

The above equation (4.15) shows that for any radius R of the sphere $N(-u) \geq N(u)$ if $u > 0$. Thus it follows that the regularised delta potentials with negative u are the attractive potentials, in the sense defined above.

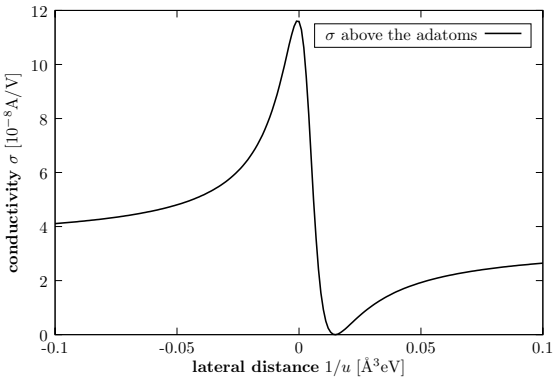

Figure 4.1: Here the resulting conductivities for different adatoms are shown. The STM tip is located directly above the adatom. The physical setup is the "standard setup": The partially reflecting surface has a strength of 60ÅeV. It is 8Å away from the STM tip. The slope of the potential is $F = 1\text{eV/Å}$. The tip emitting electrons with an energy of -0.3eV is 4Å away from the adatom. For this standard setup, the parameters are: $a = 0.0039378\frac{1}{\text{eVÅ}^3}$, $b = -0.00697744\frac{1}{\text{eVÅ}^3}$, $A = -9.61925 \cdot 10^{-5}\frac{1}{\text{eVÅ}^3}$, $B = -6.16125 \cdot 10^{-5}\frac{1}{\text{eVÅ}^3}$ and $\sigma_{\text{back}} = 3.38257 \cdot 10^{-8}\frac{\text{A}}{\text{V}}$.

4.2 The influence of the u_j on the STM images

In this section, the conductivity picture of a single adatom is studied. It has already been pointed out in section 3.5 that the single adatom behaviour is the key to understand the corral images. For this purpose, all parameters are kept constant except the scattering cross section σ_1 of the adatom. Thus only the parameter u_1 is varied. Let

$$A + iB \stackrel{\text{def}}{=} G^{\text{w}}(\mathbf{r}, \mathbf{r}_j, E) \qquad \text{and} \qquad a + ib \stackrel{\text{def}}{=} \mathbf{C}(E), \tag{4.16}$$

where $\mathbf{C}(E)$ is given by equation (2.95). Although A diverges for $\mathbf{r} \to \mathbf{r}_j$ it is not necessarily true that $A \gg B$. The conductivity $\sigma(\mathbf{r}', E)$ is given by:

$$\begin{aligned}\sigma(\mathbf{r}', E) &\propto \text{Im}(G^{\text{w}}(\mathbf{r}, \mathbf{r}', E) + (A + iB)\frac{1}{u_1^{-1} - (a + ib)}(A + iB)) \\ &= \text{Im}(G^{\text{w}}(\mathbf{r}, \mathbf{r}', E)) + \Big(\frac{b}{B}(A^2 - B^2) + 2A(u_1^{-1} - a)\Big)\frac{B}{(u_1^{-1} - a)^2 + b^2}. \end{aligned} \tag{4.17}$$

The last expression shows that the conductivity has mainly a Lorentzian shape (see figure 4.1). The important difference is the term linear in u_1^{-1} in

the numerator. The zero of the numerator is given by:

$$\frac{1}{u} = -\frac{A^2 - B^2}{2A}\frac{b}{B} + a = \Big(\frac{B}{A} - \frac{A}{B}\Big)\frac{b}{2} + a. \tag{4.18}$$

Why is this zero of physical importance? The zero is the point where single adatoms seen as a conductivity maximum are suddenly seen as a conductivity minimum and vice versa. It is interesting to note that knowledge of the phase of the Green's function $G^{\mathrm{w}}(\mathbf{r}, \mathbf{r}_j, E)$ is sufficient to determine this zero. The expression (4.17) is especially interesting when the tip is above the adatom, that is $\rho = 0$. In this case, the real part A is given by the integral:

$$A = \frac{M}{2\pi\hbar^2}\int_{-\infty}^{E} \mathrm{Re}\big(G_1{}^{\mathrm{w}}(z, z', E')\big)\, dE'. \tag{4.19}$$

In section 5.4 it will be shown that the real part a is given by the expression:

$$a = \frac{M}{2\pi\hbar^2}\int_{-\infty}^{E}\left(\mathrm{Re}\big(G_1{}^{\mathrm{w}}(z, z, E')\big) + \frac{M}{\hbar^2\sqrt{E - E'}}\right)dE'. \tag{4.20}$$

4.3 An approximation of the Green's function G^{w}

To gain more insight into the oscillations of the standing waves in the corral images, it is necessary to approximate the one–dimensional Green's function (3.10). If the parameter α is infinitely large, the quasi bound states of the potential $U_1(z) = -F \cdot z + \alpha\delta(z - z_{\mathrm{w}})$ turn into bound states. Then the Green's function has the following form [13]:

$$G_1{}^{\mathrm{w}}(z, z', E) = \sum_{n=0}^{\infty} \frac{\phi_n(z)\phi_n^*(z')}{E + z_{\mathrm{w}}F - E_n}. \tag{4.21}$$

The problem now turned into the quantum mechanical bouncing ball problem. Its solutions are well known. The wave function is:

$$\begin{aligned}\phi_n(z) = \Big(\frac{2MF}{\hbar^2}\Big)^{\frac{1}{6}}\frac{1}{\mathrm{Ai}'(a_n)}\,\mathrm{Ai}\bigg(\Big(\frac{2MF}{\hbar^2}\Big)^{\frac{1}{3}}(z_{\mathrm{w}} - z) + a_n\bigg) = \\ \Big(\frac{2MF}{\hbar^2}\Big)^{\frac{1}{6}}\frac{1}{\mathrm{Ai}'(a_n)}\,\mathrm{Ai}\Big(\beta\big(F(z_{\mathrm{w}} - z) - E_n\big)\Big),\end{aligned} \tag{4.22}$$

where a_n is the n-th zero of the Airy function. The eigenenergies E_n of the states ϕ_n are given by:

$$E_n = -\left(\frac{F^2\hbar^2}{2M}\right)^{\frac{1}{3}} a_n.$$

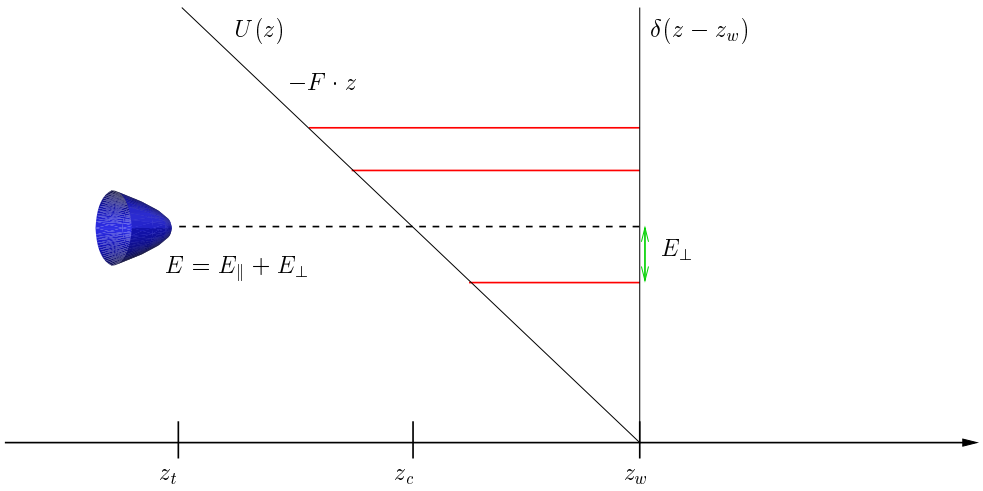

Figure 4.2: This is the potential $U_1(z)$ of the model in z–direction. This potential possesses quasi bound states with energies E_n. Thus, mainly electrons with $E_\parallel = E_n$ are transmitted. The excess energy $E - E_n$ is taken by the remaining degrees of freedom. It can be shown that the single adatom behaves like a two–dimensional electron source with energies $E - E_n = E_\perp$, where the dominant contribution comes from the classically allowed first resonance E_0.

The one–dimensional Green's function with finite but large α is now approximated by expression (4.21), where E_n is chosen complex by the condition

$$G_1(z_\mathrm{w}, z_\mathrm{w}, E_n - z_\mathrm{w}F) = \frac{1}{\alpha}. \tag{4.23}$$

The condition (4.23) assures that the denominator of (3.10) is zero. Thus (4.21) and (3.10) have the same singularities. That this choice of the energy E_n is sensible will be shown in section 4.5. In particular, it will be proved that the expression (4.21) yields a retarded Green's function with this energy definition.

Writing the one–dimensional Green's function as in equation (4.21) has the major advantage that this expression can easily be Hankel transformed. The corresponding three–dimensional Green's function is:

$$G^\mathrm{w}(\mathbf{r}, \mathbf{r}', E) = G^\mathrm{w}(z, z', \rho, E) = -\frac{M}{\pi\hbar^2} \cdot \sum_{n=0}^{\infty} \phi_n(z)\phi_n^*(z') K_0\Big(\rho \frac{\sqrt{2M(E_n - z_\mathrm{w}F - E)}}{\hbar}\Big). \tag{4.24}$$

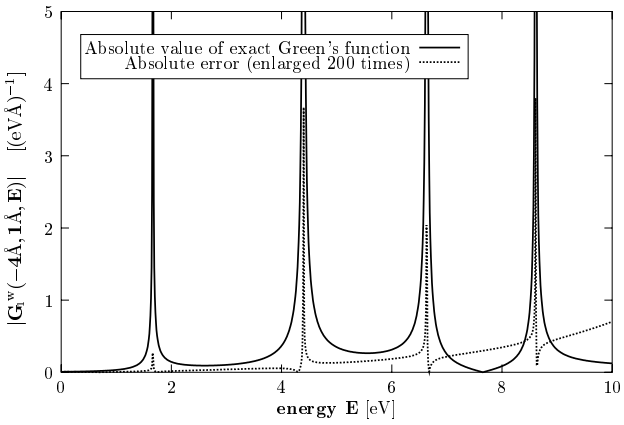

Figure 4.3: The absolute value of the exact one–dimensional Green's function (3.10) with $F = 1\text{eV/Å}$, $\alpha = 300\text{ÅeV}$, and $z_{\mathrm{w}} = 2\text{Å}$. Only the first 7 energy poles E_n are considered in the approximation. (4 poles must be included since they are shown in the picture. The next pole above 10eV also plays a dominant role for energies between $9 - 10\text{eV}$. The other 2 poles are included though they hardly contribute to the approximation.) Although the infinite sum (4.24) is approximated by a partial sum of only 7 summands, the difference between the approximation and the exact Green's function is extremely small. To illustrate the validity of this approximation, the absolute error is shown. The relative error is very small except near the zero of the one–dimensional Green's function. The relative error increases for energies greater than 10eV due to the different asymptotes of the two functions.

The three–dimensional bouncing ball potential is separable. Therefore, the notion of the total energy of the electron *parallel*, $E_{\parallel}$, and *orthogonal*, $E_{\perp}$ to the surface may be introduced.

The essential point is that the energy $E_{\parallel}$ must be given by

$$E_{\parallel} = E_n. \tag{4.25}$$

Correspondingly, the energy $E_{\perp}$ is:

$$E_{\perp} = E + z_{\mathrm{w}}F - E_n. \tag{4.26}$$

The term $z_{\mathrm{w}}F$ adjusts the energy zero so that it lies at the bottom of the bouncing ball potential. Thus the term $z_{\mathrm{w}}F$ simply shifts the energy zero for a given configuration. Before the numerical evaluation of the expression (4.24) is discussed, the total current through the bouncing ball barrier is calculated. For this purpose, an STM tip is positioned in front of the barrier, as it is shown in figure 4.2.

At first, some preliminaries are presented. Since the argument of the Bessel function K_0 is either purely real or purely imaginary, the following identity is very useful:

$$K_0(-iz) = \frac{\pi}{2}\big(iJ_0(z) - Y_0(z)\big). \tag{4.27}$$

With this relation, it is easily seen that for $\rho = 0$

$$\mathrm{Im}\big(G^{\mathrm{w}}(z, z', 0, E)\big) = -\frac{M}{2\hbar^2} \cdot \sum_{n=0}^{m} \phi_n(z)\phi_n^*(z'), \tag{4.28}$$

where m is chosen so that $E_m - z_{\mathrm{w}}F - E < 0$ and $E_{m+1} - z_{\mathrm{w}}F - E > 0$. If $E_0 - z_{\mathrm{w}}F - E > 0$ the sum is empty, so m may be chosen to be $m = -1$. Equation (4.28) in fact hides some essential physics that is revealed on further consideration. Assuming that there is no adatom, then the total current through an s–tip at position $\mathbf{r}$ would be (from equation (2.10), equation (2.69) and section 2.4.5)

$$J(E) = -\frac{4\hbar}{Mk_{\mathrm{tip}}}\,\mathrm{Im}\big(G^{\mathrm{w}}(\mathbf{r}, \mathbf{r}, E)\big). \tag{4.29}$$

Equation (4.28) now states that no current flows as long as $E < E_0 - z_w F$. In the energy range $E_0 - z_w F \leq E < E_1 - z_w F$ there will be a constant current flow given by

$$J(E) = -\frac{4\hbar}{Mk_{\mathrm{tip}}}\frac{M}{2\hbar^2}\big|\phi_n(z)\big|^2. \tag{4.30}$$

In the next energy interval from $E \in [E_1, E_2[$, there will be an additional contribution from the resonance at E_1 and so on. The total current versus energy function is a step function, with steps precisely at the bound states E_n. More figuratively, one could say that each resonance E_n has the capability to conduct a fixed amount of current. But this channel is only used for electron conduction if and only if it is classically allowed, that is, $E > E_n$. For finite α, the sharp resonances broaden and the sharp steps in the total current versus energy function are slightly smoothed. At first sight one might think that there cannot flow any current through the bouncing ball setup illustrated in figure 4.2. But obviously, the current does flow to the boundary of physical space along the reflecting surface at z_{w}.

After this small excursion, let us continue with the calculation of the three–dimensional Green's function $G^{\mathrm{w}}(\mathbf{r}, \mathbf{r}', E)$. Equation (4.24) is still an infinite sum and can only be evaluated numerically for a finite number of

summands. This equation resembles very much a Fourier series. From the previous paragraph it is clear that the maximal index $n_{\max}$ should at least fulfil $E < E_{n_{\max}}$. In fact, it turns out that the expression (4.24) converges very fast as long as $\rho \gg 0$. So it suffices to include one or two resonances that lie above the energy E. In how far this approximation

$$G^{\mathrm{w}}(\mathbf{r}, \mathbf{r}', E) \approx -\frac{M}{\pi\hbar^2} \cdot \sum_{n=0}^{n_{\max}} \phi_n(z)\phi_n^*(z') K_0\Big(\rho \frac{\sqrt{2M(E_n - z_{\mathrm{w}}F - E)}}{\hbar}\Big) \quad (4.31)$$

reproduces the original one–dimensional Green's function with finite α is shown in figure 4.3.

Although these two Green's functions hardly seem to differ — the structure of the singularities is almost perfectly reproduced — it must be noted that the asymptotes of these two functions do differ. While the original function decays like $G_1^{\mathrm{w}}(\cdot, \cdot, E) \propto e^{-\gamma\sqrt{|E|}}$ for decreasing E, any finite partial sum of equation (4.21) falls off only with $G_1^{\mathrm{w}}(\cdot, \cdot, E) \propto \frac{1}{E}$.

Due to the different asymptotes of equation (3.10) and any finite partial sum of (4.21), this Green's function can only be useful for large ρ. Indeed, the Green's function (4.31) diverges at $\rho = 0$. This is not surprising since the integral over any function that decays like $\frac{1}{x}$ will be infinite.

Comparing expression (4.21) and (3.10) in the limit $\alpha \to \infty$ leads to the interesting and not at all obvious identity:

$$G_1(z, z', E) - \frac{G_1(z, z_{\mathrm{w}}, E) G_1(z_{\mathrm{w}}, z', E)}{G_1(z_{\mathrm{w}}, z_{\mathrm{w}}, E)} = \sum_{n=0}^{\infty} \frac{\phi_n(z)\phi_n^*(z')}{E + z_{\mathrm{w}}F - E_n}. \quad (4.32)$$

4.4 Applying the bouncing ball approximation to corral images

In the previous section it was shown how the three–dimensional Green's function can be approximated by a sum of Bessel functions K_0. The actual wavelength of the standing wave pattern (in figures 3.5 and 3.6) is half the wavelength of the underlying three–dimensional Green's function (4.24), since the total current (given by equation (2.101) and (2.10)) depends quadratically on the Green's function. This is even valid for the multipole case as can be seen from equation (2.110). For the multipole case this might be a surprise since the multipole Green's function G_{l0}^{w} is not symmetric in its arguments. Nonetheless, the wavelength for a single adatom is again proportional to $\big(G_{l0}^{\mathrm{w}}\big)^2$.

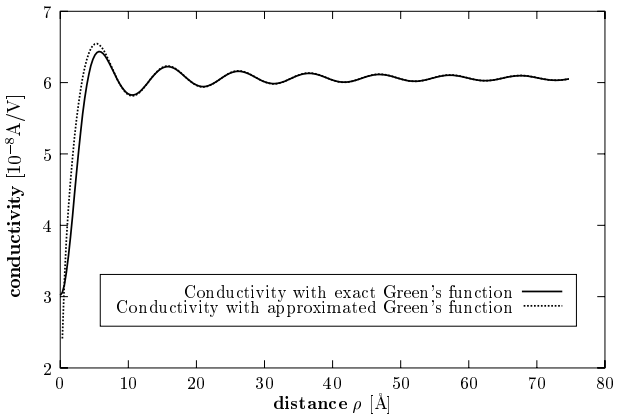

Figure 4.4: This figure shows the resulting conductivity profile for the single adatom in figure 3.5. The conductivity resulting from the exact Green's function is compared to the conductivity calculated with the approximation. Although the approximation is not valid in the vicinity of the atom, the wavelength of the oscillation is almost perfectly reproduced by the approximation. In this case, the imaginary part of the energy $\mathrm{Im}(E_n) = -0.00289577\mathrm{eV}$.

Since the Bessel function K_0 has *no* oscillatory behaviour for a real argument, only the "classically allowed" quasi bound states can contribute to the observed wavelength. Equation (4.31) states that the wavelength λ of the three–dimensional Green's function is given by a superposition of wavelength λ_n. The wavelengths λ_n are given by

$$\lambda_n \stackrel{\mathrm{def}}{=} \frac{\sqrt{2M(E_n - z_{\mathrm{w}}F - E)}}{\hbar}, \tag{4.33}$$

where the energies E_n are determined by equation (4.23). All experimental images of quantum corrals and single adatoms that I know of show no superposition of two or more wavelengths. Instead, there is strong evidence that they can be described with only a single wavelength [20]. That means that the energy E of the emitted electrons must lie between E_0 and E_1, as shown in figure 4.2.

Remark 4 It is an interesting question whether it is possible to observe a superposition of two or more wavelengths experimentally. There are two fundamental experimental difficulties:

1. In the theory presented, the tip–vacuum probe potential is completely decoupled from the applied bias voltage. In an experiment, this is not the case.
2. Futhermore, in this theory the partially reflecting surface is independent from the energy of the incident electrons. Translated into the language of solid state physics,

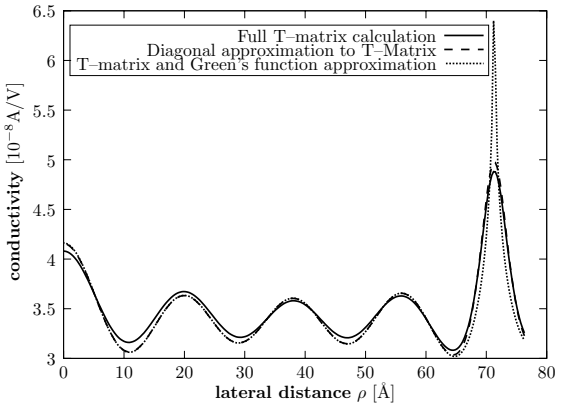

Figure 4.5: This is a comparison of the approximations presented in this thesis. The physical setup is the "standard setup": The partially reflecting surface has a strength of 60ÅeV. It is 8Å away from the stm tip. The slope of the potential is $F = 1\text{eV}/\text{Å}$. The tip emitting electrons with an energy of -0.3eV is 4Å away from the adatom. The parameter describing the adatoms is $u_i = -27.6\text{Å}^3\text{eV}$.

this means that the probe material has an infinitely large band gap. This obviously cannot be achieved experimentally. But the band gap may be big enough to cover the energy range of the first two resonances E_0 and E_1.

With this knowledge at hand, it is straightforward to simulate quantum corrals with the approximation (4.31) of G^{w}. In figure 4.4, the exact and the approximated conductivities are compared. The very good agreement shows the usefulness of this approximation. It is best in the region far away from the adatom sites ($\rho \gg 0$), since then the infinite sum (4.24) converges very fast, and thus the approximation (4.31) gives almost the exact result, as can be seen in figure 4.4 and 4.5.

From equation (2.57) and the explicit expressions of the $\mathcal{Y}_{lm}$ given in section 2.4.5 it is now clear why the standing wave pattern hardly changes when the multipolarity of the tip is changed. Taking the following relationship into account

$$\frac{1}{\rho}\partial_\rho \rho \partial_\rho K_0(\rho) = K_0(\rho), \tag{4.34}$$

which can be easily derived from the expressions 3.71.7 and 3.71.5 in [64], it is seen that only the prefactor of the K_0 in equation (4.24) is changed by a different multipole tip.

It is remarkable that the free particle Green's function in two–dimensions

is

$$G_2^{\text{free}}(\mathbf{r}, \mathbf{r}', E) = G_2^{\text{free}}(\rho, \phi, E) = -\frac{M}{\pi\hbar^2} K_0(k_0\rho), \tag{4.35}$$

where $k_0 = \sqrt{2ME}/\hbar$. It is obvious that a single scattering adatom at the z–position z_0 behaves like a point source in the two–dimensional z_0 plane in this approximation. In several publications, this behaviour of the scattering atoms is intuitively used [8, 53, 25, 29].

To conclude: The wavelengths appearing in a quantum corral are in direct correspondence with the eigenenergies of the one–dimensional potential $-F \cdot z + \alpha\delta(z - z_{\text{w}})$. This can be generalised further: The potential from the tip–conductor transition plus the effective barrier creating the Shockley surface states build a potential pot. The eigenenergies of this potential pot are seen in a quantum corral. What is more, they can be observed already in case of a single scatterer, and not only when a ring of atoms are used.

4.5 The correct choice of the eigenenergies E_n

The energy E_n in equation (4.21) should have a relatively small *negative* imaginary part, since the Green's function is supposed to be the retarded Green's function of the problem. A retarded Green's function is usually defined to have a small positive imaginary part in the denominator. This would be the case if $\operatorname{Im} E_n < 0$. E_n is chosen by the condition

$$G_1(z_{\text{w}}, z_{\text{w}}, E_n) = \frac{1}{\alpha}, \tag{4.36}$$

where α is real and G_1 is the retarded Green's function.

Proposition 4.5.1 *When there exists an $E \in \mathbb{C}$ so that $\operatorname{Im} G_1\big(z, z, E\big) = 0$ for fixed z then $\operatorname{Im}(E) < 0$.*

Proof We start from equation (2.24):

$$G_1(z, z', E) = \int \frac{\phi(\mu, z)\phi^*(\mu, z')}{E - \mu} d\mu - i\pi\phi(E, z)\phi^*(E, z'). \tag{4.37}$$

Now let $E = \mathcal{E} + i\epsilon$ be the decomposition in real and imaginary parts. It follows that

$$\operatorname{Im}\Big(G_1(z, z, E)\Big) = (-\epsilon) \int \frac{|\phi(\mu, z)|^2}{(\mathcal{E} - \mu)^2 + \epsilon^2} d\mu - \pi|\phi(\mathcal{E} + i\epsilon, z)|^2. \tag{4.38}$$

Since $|\phi(\mathcal{E} + i\epsilon, z)|^2 = 0$ if and only if $\phi = 0$ (but this degenerate solution is by definition no wavefunction), it follows that $|\phi(\mathcal{E} + i\epsilon, z)|^2 > 0$. The first

term is also greater or equal to 0. Thus $\mathrm{Im}\Big(G_1(z,z,E)\Big)$ can only be 0 for $\epsilon < 0$. The proposition follows. ∎

Chapter 5

Numerical details

This section describes all numerical methods necessary for the actual implementation of the STM simulation presented so far. At first, some one–dimensional Green's functions are derived for several potentials. The resulting current distributions and the algorithms to implement these one–dimensional Green's functions have been presented in detail in [12]. It is a pity that the freely available *GNU scientific library* cannot evaluate most special functions with complex arguments, but can handle only the real argument case. Thus it was necessary to implement the Airy functions to calculate the one–dimensional Green's function of the triangular barrier. The numerical evaluation of the Gaussian hypergeometric function ${}_2F_1$ for complex arguments, which appear in the one–dimensional Green's function of the smooth barrier, is presented in detail in [12]. The numerical evaluation of the Hankel transform (2.87) is not at all straight forward since due to the Bessel functions the integrand is oscillating. Furthermore, the algorithm presented in section 5.2 is a numerical transform. That is, it returns the transformed function instead of a single value. In section 5.3, the numerical evaluation of the multipole current

$$\lim_{\mathbf{r}'\to\mathbf{r}} (-1)^m \mathcal{Y}_{lm}\Big(\frac{\partial}{\partial \mathbf{r}'}\Big)\mathcal{Y}_{l-m}\Big(\frac{\partial}{\partial \mathbf{r}}\Big) G^{\mathrm{w}}(\mathbf{r},\mathbf{r}',E) \tag{5.1}$$

in equation (2.110) is presented. The method to determine this integral resembles the method employed in section 2.5.3. The chapter concludes with several tricks to calculate the necessary quantities. Especially in section 5.4, where the numerical evaluation of the regularised T–matrix elements (the diagonal T-matrix elements) in expression (2.95) is discussed, some insight into the general properties of Green's functions is gained.

5.1 Some one–dimensional Green's functions

5.1.1 The Green's function of the smooth barrier

Before calculating the Green's function, the two fundamental solutions of the Schrödinger equation

$$\left(E + \frac{\hbar^2}{2M}\partial_z^2 - \frac{V_0}{1+e^{\alpha z}}\right)\phi(z) = 0 \tag{5.2}$$

must be determined (see [40], page 78). Defining $\beta = \sqrt{\frac{2MV_0}{\hbar^2}}$ and $k = \sqrt{\frac{2ME}{\hbar^2}}$, the Schrödinger equation can be rewritten as

$$\partial_z^2\phi(z) + k^2\phi(z) - \frac{\beta^2}{1+e^{\alpha z}}\phi(z) = 0. \tag{5.3}$$

This differential equation can be cast into a new form by using the definition $\kappa = \sqrt{\frac{2M(V_0-E)}{\hbar^2}}$, introducing the new variable $x = -e^{\alpha z}$ ($\Rightarrow \partial_z^2 = \alpha^2 x(\partial_x + x\partial_x^2)$), and utilising the following ansatz

$$\phi(z) = x^{\frac{\kappa}{\alpha}} f(x)$$

for the wavefunction $\phi(z)$. Now the differential equation (5.3) is mapped to the differential equation for $f(x)$:

$$x(1-x)f''(x) + \left(\left(1+\frac{2\kappa}{\alpha}\right) - \left(1+\frac{2\kappa}{\alpha}\right)x\right)f'(x) - \frac{\beta^2}{\alpha^2}f(x) = 0. \tag{5.4}$$

This equation (5.4) has the structure of a Gaussian hypergeometric differential equation. Its solutions are well known (see for instance [1] 15.5.1):

$$f_{reg}(x) = {}_2\mathrm{F}_1\left(\frac{1}{\alpha}(\kappa+ik), \frac{1}{\alpha}(\kappa-ik), 1+\frac{2\kappa}{\alpha}, x\right)$$
$$f_{irr}(x) = x^{-\frac{2\kappa}{\alpha}}\,{}_2\mathrm{F}_1\left(-\frac{1}{\alpha}(\kappa+ik), -\frac{1}{\alpha}(\kappa-ik), 1-\frac{2\kappa}{\alpha}, x\right).$$

Replacing the new variables by the old ones leads to:

$$\phi(z) = e^{\kappa z}\,{}_2\mathrm{F}_1\left(\frac{1}{\alpha}(\kappa+ik), \frac{1}{\alpha}(\kappa-ik), 1+\frac{2\kappa}{\alpha}, -e^{\alpha z}\right) \tag{5.5}$$
$$\phi_{irr}(z) = e^{-\kappa z}\,{}_2\mathrm{F}_1\left(-\frac{1}{\alpha}(\kappa+ik), -\frac{1}{\alpha}(\kappa-ik), 1-\frac{2\kappa}{\alpha}, -e^{\alpha z}\right).$$

The Gaussian hypergeometric function is defined as

$$ {}_2\mathrm{F}_1(a,b,c,z) = \sum_{n=0}^{\infty} \frac{(a)_n (b)_n}{(c)_n} \frac{z^n}{n!} = 1 + \frac{ab}{c} z + \frac{a(a+1)b(b+1)}{c(c+1)} \frac{z^2}{2!} + \ldots $$

for $|z| < 1$, where

$$ (x)_n = \frac{\Gamma(x+n)}{\Gamma(x)}. $$

To define the Gaussian hypergeometric function ${}_2\mathrm{F}_1(a,b,c,z)$ for $z \in \mathbb{C}$, the linear transformations must be used (see for instance [1] 15.3.3–15.3.14). The solutions have the structure ${}_2\mathrm{F}_1(a,a^*,c,z)$. Obviously, these solutions are real for $c, z \in \mathbb{R}$ and $a \in \mathbb{C}$. The solution $\phi(z)$ decays exponentially for $z \to -\infty$. Therefore ϕ is the bounded solution, while the solution ϕ_{irr} is unbounded, since $\phi_{irr}(z)$ grows exponentially for $z \to -\infty$. From these two solutions an appropriate linear combination must be found, which behaves like an outgoing wave. The solution that has the asymptotes of an outgoing wave is essential to construct the retarded Green's function, as we have seen in section 2.3. Using the following linear transformation (see [1] 15.3.7) and the abbreviation

$$ \lambda = \frac{\kappa + ik}{\alpha},\ \mu = 1 - \frac{2ik}{\alpha} \text{ and } \nu = \frac{2ik}{\alpha}, \tag{5.6} $$

the solution can be rewritten as:

$$ \phi(z) = 2\Gamma\left(1 + \frac{2\kappa}{\alpha}\right) \mathrm{Re}\left(\frac{\Gamma(\nu) e^{ikz}}{\Gamma(\lambda)\Gamma(1+\lambda)} \, {}_2\mathrm{F}_1(\lambda^*, -\lambda, \mu, -e^{-\alpha z}) \right) $$

$$ \phi_{irr}(z) = 2\Gamma\left(1 - \frac{2\kappa}{\alpha}\right) \mathrm{Re}\left(\frac{\Gamma(\nu) e^{ikz}}{\Gamma(-\lambda^*)\Gamma(1-\lambda^*)} \, {}_2\mathrm{F}_1(-\lambda, \lambda^*, \mu, -e^{-\alpha z}) \right). $$

Since the following relation holds

$$ \lim_{z \to \infty} {}_2\mathrm{F}_1(a,b,c,-e^{-\alpha z}) = 1, \tag{5.7} $$

the asymptotic behaviour of the two solutions when $z \to \infty$ is known:

$$ \phi(z) = 2\Gamma\left(1 + \frac{2\kappa}{\alpha}\right) \mathrm{Re}\left(\frac{\Gamma(\nu) e^{ikz}}{\Gamma(\lambda)\Gamma(1+\lambda)} \right) $$

$$ \phi_{irr}(z) = 2\Gamma\left(1 - \frac{2\kappa}{\alpha}\right) \mathrm{Re}\left(\frac{\Gamma(\nu) e^{ikz}}{\Gamma(-\lambda^*)\Gamma(1-\lambda^*)} \right). $$

Now an outgoing wave is easily constructed as:

$$ \phi(z) = \frac{\Gamma(1 - \frac{2\kappa}{\alpha})\Gamma(\nu^*)}{\Gamma(-\lambda)\Gamma(1-\lambda)} \phi(z) - \frac{\Gamma(1 + \frac{2\kappa}{\alpha})\Gamma(\nu^*)}{\Gamma(\lambda^*)\Gamma(1+\lambda^*)} \phi_{irr}(z). \tag{5.8} $$

By skilled use of the already mentioned linear transformations (see [49]), this outgoing wave can be expressed as:

$$\psi_+(z) = \frac{\kappa}{ik} e^{ikz}\, {}_2\mathrm{F}_1\left(-\frac{\kappa+ik}{\alpha}, \frac{\kappa-ik}{\alpha}, 1-\frac{2ik}{\alpha}, -e^{-\alpha z}\right). \tag{5.9}$$

The solutions (5.5) and (5.9) can be analytically continued into the classical forbidden region with energy $E < 0$. As usual, let $\tilde{k} = \frac{\sqrt{-2ME}}{\hbar}$. Due to the general properties of the Green's function in the tunnelling region, the following must hold: $\psi_+(z) \propto e^{-\tilde{k}z}$. Therefore, in the correct analytic continuation for $E < 0$, ik is replaced by $-\tilde{k}$ ($k = i\tilde{k}$). This leads to the two solutions:

$$\phi(z) = e^{\kappa z}\, {}_2\mathrm{F}_1\left(\frac{\kappa-\tilde{k}}{\alpha}, \frac{\kappa+\tilde{k}}{\alpha}, 1+\frac{2\kappa}{\alpha}, -e^{\alpha z}\right) \tag{5.10}$$

$$\psi_+(z) = -\frac{\kappa}{\tilde{k}} e^{-\tilde{k}z}\, {}_2\mathrm{F}_1\left(-\frac{\kappa-\tilde{k}}{\alpha}, \frac{\kappa+\tilde{k}}{\alpha}, 1+\frac{2\tilde{k}}{\alpha}, -e^{-\alpha z}\right). \tag{5.11}$$

To fully determine the Green's function, the Wronskian of these two solutions must be evaluated. Since the differential equation for these solutions does not contain any term proportional to $\partial_z\phi(z)$, the Wronskian must be constant (z independent). Thus the Wronskian can be calculated from the asymptotic behaviour of the solutions for ($z \to \infty$):

$$\mathcal{W}(\phi(z), \psi_+(z)) = \phi'(z)\psi_+(z) - \phi(z)\psi'_+(z) = 2\kappa \frac{\Gamma(-\frac{2ik}{\alpha})\Gamma(1+\frac{2\kappa}{\alpha})}{\Gamma(\frac{\kappa-ik}{\alpha})\Gamma(1+\frac{\kappa-ik}{\alpha})}. \tag{5.12}$$

With this result, the Green's function is now given by:

$$\begin{aligned} G_1(z, z', E) =& \frac{2M}{\hbar^2} \frac{\phi(z_<)\psi_+(z_>)}{\mathcal{W}(\phi(z_<), \psi_+(z_>))} = -\frac{2m}{\hbar^2\alpha} \frac{\Gamma(\frac{\kappa-ik}{\alpha})\Gamma(1+\frac{\kappa-ik}{\alpha})}{\Gamma(1-\frac{2ik}{\alpha})\Gamma(1+\frac{2\kappa}{\alpha})} e^{\kappa z_< + ikz_>} \cdot \\ & {}_2\mathrm{F}_1\left(-\frac{\kappa+ik}{\alpha}, \frac{\kappa-ik}{\alpha}, 1-\frac{2ik}{\alpha}, -e^{-\alpha z_>}\right) \cdot \\ & {}_2\mathrm{F}_1\left(\frac{\kappa+ik}{\alpha}, \frac{\kappa-ik}{\alpha}, 1+\frac{2\kappa}{\alpha}, -e^{\alpha z_<}\right), \end{aligned} \tag{5.13}$$

where $k = \sqrt{\frac{2ME}{\hbar^2}}$, $\kappa = \sqrt{\frac{2M(V_0-E)}{\hbar^2}}$, $z_< = \min(z, z')$ and $z_> = \max(z, z')$.

5.1.2 The Green's function of the step barrier

To calculate the Green's function for the step barrier, a fundamental solution of the corresponding Schrödinger equation must be determined:

$$\left(E + \frac{\hbar^2}{2M}\partial_z^2 - V_1\theta(z) - V_2\theta(-z)\right)\phi(z) = 0. \tag{5.14}$$

Without loss of generality, let $V_2 > V_1$. At first, the case where $V_2 \leq E \leq V_1$ is considered. Additionally, we use the definition

$$k_1 \stackrel{\text{def}}{=} \frac{\sqrt{2M(V_1 - E)}}{\hbar} \text{ and } k_2 \stackrel{\text{def}}{=} \frac{\sqrt{2M(V_2 - E)}}{\hbar}. \tag{5.15}$$

It is well known that the solution of the equation (5.14) has the following structure:

$$\psi(z) = \begin{cases} Ae^{k_2 z} + Be^{-k_2 z} \text{ for } z < 0 \\ Ce^{k_1 z} + De^{-k_1 z} \text{ for } z > 0. \end{cases} \tag{5.16}$$

The introduced constants are complex numbers: $A, B, C, D \in \mathbb{C}$. The regular solution (wavefunction) must be bounded, therefore $B = 0$. Furthermore, ψ as well as ψ' must be continuous. These conditions lead to:

$$\phi(z) = D \cdot \begin{cases} (1+R)e^{k_2 z} \text{ for } z < 0 \\ Re^{k_1 z} + e^{-k_1 z} \text{ for } z > 0, \end{cases} \tag{5.17}$$

where $R \stackrel{\text{def}}{=} \frac{k_1 + k_2}{k_1 - k_2}$ (reflection coefficient). Usually, the last free parameter D is calculated by the normalisation condition (in this case usually a normalised current is assumed). For the calculation of the Green's function, the form (5.17) is totally satisfactory, since the Wronskian will be proportional to D. By a completely analogous treatment, the irregular solution ϕ_{irr} can be determined. It is given by:

$$\phi_{irr}(z) = E \cdot \begin{cases} (1+R)e^{-k_2 z} \text{ for } z < 0 \\ e^{k_1 z} + Re^{-k_1 z} \text{ for } z > 0. \end{cases} \tag{5.18}$$

With equation (5.17) and equation (5.18) at hand, it is now possible to construct an outgoing wave ($\psi_+ \propto e^{k_1 z}$ for $z \to \infty$). This outgoing wave is given by the expression:

$$\psi_+(z) = \frac{D\phi_{irr}(z) - ER\phi(z)}{(1+R)^2} = \frac{DE}{1+R} \cdot \begin{cases} e^{-k_2 z} - Re^{+k_2 z} \text{ for } z < 0 \\ (1-R)e^{k_1 z} \text{ for } z > 0. \end{cases} \tag{5.19}$$

From equation (5.19) it is obvious how k_1 must be defined in the case $V_1 > E$. In this case, equation (5.19) must again be a bounded solution for $V_1 > E$. Thus k_1 must be given by:

$$k_1 \stackrel{\text{def}}{=} -\frac{\sqrt{2M(V_1 - E)}}{\hbar}. \tag{5.20}$$

To calculate the retarded Green's function G_1 the Wronskian of the solution (5.17) and (5.19) must be determined:

$$\mathcal{W}(\phi(z), \psi_+(z)) = \phi(0)\psi'_+(0) - \phi'(0)\psi_+(0) = -D^2E \cdot 2k_2. \tag{5.21}$$

With all these results the retarded Green's function G_1 is given by:

$$\begin{aligned} G_1(z, z', E) = \frac{M}{\hbar^2}\Bigg(& \frac{\theta(z_<)\theta(z_>)}{k_1}(e^{k_1(z_> - z_<)} + Re^{k_1(z_> + z_<)}) - \\ & \frac{\theta(-z_<)\theta(-z_>)}{k_2}(e^{-k_2(z_> - z_<)} - Re^{k_2(z_> + z_<)}) + \\ & \frac{\theta(-z_<)\theta(z_>)T}{i\sqrt{k_1 k_2}}(e^{k_2 z_<} e^{k_1 z_>})\Bigg). \end{aligned} \tag{5.22}$$

In equation (5.22), the transmission coefficient is given by $T \stackrel{\text{def}}{=} i\frac{2\sqrt{k_1 k_2}}{k_1 - k_2}$. The result agrees with the one published in [62] (page 154).

5.1.3 The Green's function of the triangular barrier

Before calculating the Green's function, the fundamental solutions of the corresponding Schrödinger equation for the triangular barrier must be determined:

$$\left(E + \frac{\hbar^2}{2M}\partial_z^2 + Fz\right)\phi(z) = 0. \tag{5.23}$$

The new variable $x = 2az + b$ is introduced, where

$$a = -\left(\frac{MF}{4\hbar^2}\right)^{\frac{1}{3}} \text{ and } b = -\frac{ME}{2\hbar^2 a^2}. \tag{5.24}$$

This substitution maps the Schrödinger equation to the so–called Airy differential equation. This equation has the fundamental solutions $\mathrm{Ai}(x)$ and $\mathrm{Bi}(x)$. Studying the asymptotic behaviour of the solutions when $x \to -\infty$

$(z \to \infty)$ is essential to construct the outgoing wave. From [1] 10.4.61 and 10.4.63 follows that

$$\mathrm{Ai}(-z) \propto \frac{1}{\sqrt{\pi}} z^{-\frac{1}{4}} \sin\left(\zeta + \frac{\pi}{4}\right) \tag{5.25}$$

$$\mathrm{Bi}(-z) \propto \frac{1}{\sqrt{\pi}} z^{-\frac{1}{4}} \cos\left(\zeta + \frac{\pi}{4}\right), \tag{5.26}$$

where $\zeta = \frac{2}{3} z^{\frac{3}{2}}$. The outgoing wave is therefore given by

$$\mathrm{Ci}(x) = \mathrm{Bi}(x) + i\,\mathrm{Ai}(x). \tag{5.27}$$

By using the previously mentioned transformation $x = 2az + b$ and $x' = 2az' + b$, the Green's function can be written as:

$$G_1(x, x', E) = \frac{2M}{\hbar^2} \frac{\mathrm{Ai}(x_>)\,\mathrm{Ci}(x_<)}{\mathcal{W}(\mathrm{Ai}(x_>)\,\mathrm{Ci}(x_<))}. \tag{5.28}$$

In the above expressions, the following definitions have been utilised: $x_> = \max(x, x')$ and $x_< = \min(x, x')$. The Wronskian is easily calculated to be $\mathcal{W}(\mathrm{Ai}(x_>)\,\mathrm{Ci}(x_<)) = -\frac{a}{2\pi}$. The complete result is thus:

$$G_1(u, v, E) = -\frac{M\pi}{a\hbar^2}\,\mathrm{Ai}\left(\frac{u + v - |u - v|}{2}\right)\mathrm{Ci}\left(\frac{u + v + |u - v|}{2}\right), \tag{5.29}$$

or, expressed in the original coordinates z, z':

$$\begin{aligned} G_1(z, z', E) = -\frac{M\pi}{a\hbar^2}\,&\mathrm{Ai}\big(a(z + z' - |z - z'|) + b\big) \\ &\mathrm{Ci}\big(a(z + z' + |z - z'|) + b\big). \end{aligned} \tag{5.30}$$

5.1.4 The WKB approximated Green's function

To calculate the one–dimensional Green's function it is necessary to determine the regular solution (WKB–wavefunction) in the semiclassical approximation. We start from the Schrödinger equation, that is recast into the form:

$$\left(E + \frac{\hbar^2}{2M}\partial_z^2 - U_1(z)\right)\phi(z) = 0. \tag{5.31}$$

The semiclassical approximation is only valid in the regions far away from the classical turning points. Thus there are no more two independent solutions for the whole physical space but two independent solutions for each region. The difficulty in the semiclassical approximation is to connect these numerous

solutions to each other in such a way so that a regular solution is constructed. If the potential is monotone, then there can be only one such turning point $z_0(E)$. Furthermore, let $U_1(z)-E \leq 0$ for $z \in]-\infty, z_0(E)]$ and $U_1(z)-E \geq 0$ for $z \in [z_0(E), \infty]$. Utilising the definitions

$$k(z,E) = \sqrt{\frac{2M}{\hbar^2}\big(E - U_1(z)\big)} \tag{5.32}$$

$$\kappa(z,E) = \sqrt{\frac{2M}{\hbar^2}\big(U_1(z) - E\big)}, \tag{5.33}$$

the fundamental solutions of (5.31) are given by (see for instance [36]):

$$\phi_\pm(z,E) = \frac{1}{\sqrt{\kappa(z,E)}} e^{\pm \int_z^{z_0} \kappa(x,E)dx} \quad \text{if } z \in]-\infty, z_0(E)[\tag{5.34}$$

$$\phi_\pm(z,E) = \frac{1}{\sqrt{k(z,E)}} e^{\pm i \int_{z_0}^{z} k(x,E)dx} \quad \text{if } z \in]z_0(E), \infty[. \tag{5.35}$$

For the following discussion, let z as well as z' (position of the tip) be in the "tunnelling region" ($z, z' \in]-\infty, z_0(E)]$). Thus it is only necessary to determine the regular solution and the outgoing wave in the tunnelling region. The regular semiclassical solution is given as a linear combination of the above fundamental solutions:

$$\phi(z,E) = \frac{1}{\sqrt{\kappa(z,E)}} e^{-\int_z^{z_0} \kappa(x,E)dx}. \tag{5.36}$$

The outgoing wave is at first only known in the classically allowed region — otherwise, it could not be determined whether the solution has outgoing characteristics. Thus the outgoing wave in this region is given by:

$$\psi_+(z,E) = \frac{1}{\sqrt{\kappa(z,E)}} e^{i \int_{z_0}^{z} k(x,E)dx}. \tag{5.37}$$

Using the semiclassical connection rules, the above solution can be continued into the tunnelling region. The outgoing wave is given by (see [49]):

$$\psi_+(z,E) = \frac{e^{i\frac{\pi}{4}}}{\sqrt{\kappa(z,E)}} \left(\frac{1}{2} e^{-\int_z^{z_0} \kappa(x,E)dx} - i e^{\int_z^{z_0} \kappa(x,E)dx} \right). \tag{5.38}$$

Now the WKB Green's function in the tunnelling region is given by:

$$\begin{aligned} G(z,z',E) = -\frac{M}{\hbar^2} \frac{1}{\sqrt{\kappa(z,E)\kappa(z',E)}} e^{-\int_{z_<}^{z_0} \kappa(x,E)dx} \\ \left(e^{\int_{z_>}^{z_0} \kappa(x,E)dx} + \frac{i}{2} e^{-\int_{z_>}^{z_0} \kappa(x,E)dx} \right). \end{aligned} \tag{5.39}$$

5.2 The Hankel transformation

This section describes the basic ideas presented in [45]. The method to calculate the Hankel transform of order zero can easily be extended to transformations of higher order. What is more, the idea can be used to Hankel transform any polynomial spline, not just stepwise constant functions, as shown here. The Hankel transform of order m of a function $f(x)$ is given by:

$$g_m(y) \stackrel{\text{def}}{=} \frac{1}{2\pi} \int_0^\infty x f(x) J_m(xy) dx. \tag{5.40}$$

Remark 5 It can be shown that the above integral exists under the following conditions:

1. $f(x)$ is defined on $[0, \infty[$.
2. $f(x)$ and $\frac{d}{dx} f(x)$ are piecewise continuous.
3. $\int_0^\infty |f(x)| dx$ exists.

The reason why the above equation (5.40) is called a transformation is that

$$f(x) = 2\pi \int_0^\infty y g_m(y) J_m(yx) dy \tag{5.41}$$

holds. Unlike for the Fourier transformation, there is no standard method for the numerical evaluation of the integral (5.40). Numerous algorithms exist and it is not at all easy to identify the advantages of the different methods. Due to the simplicity (of both the implementation and the algorithm itself) and the relatively high accuracy, I have chosen the algorithm presented in [45]. That does not necessarily mean that this algorithm is superior to the others. Another interesting method is proposed by [43]. This approach is much more complicated and it is questionable whether higher accuracy can be reached in the same calculation time.

The two basic ideas to evaluate the integral (5.40) are the evaluation of the integral on a *finite* interval $[0, x_{\max}]$ and the approximation of $f(x)$ by $\tilde{f}(x)$, where $\tilde{f}(x)$ is a piecewise constant function. Additionally, an upper bound ($y_{\max}$) is chosen for y. y is replaced by $y y_{\max}$ to confine the possible values for y to $[0, 1]$. The equation (5.40) is thus approximated by the following

expression:

$$
\begin{aligned}
g(yy_{\max}) = \frac{1}{2\pi}\int_0^{x_{\max}} x\tilde{f}(x)J_0(y_{\max}xy)dx = \\
\frac{1}{2\pi}\int_0^{1} x_{\max}^2 x\tilde{f}(xx_{\max})J_0(x_{\max}y_{\max}xy)dx = \\
\frac{1}{2\pi}\sum_{n=0}^{N-1} x_{\max}^2 \int_{\xi_n}^{\xi_{n+1}} x\tilde{f}(xx_{\max})J_0(x_{\max}y_{\max}xy)dx = \\
\frac{1}{2\pi}\sum_{n=0}^{N-1} \frac{\tilde{f}(x_n x_{\max})x_{\max}}{y_{\max}y}(\xi_{n+1}J_1(x_{\max}y_{\max}y\xi_{n+1}) - \\
\xi_n J_1(x_{\max}y_{\max}y\xi_n)) = \\
\frac{1}{2\pi}\frac{x_{\max}}{y_{\max}y}\sum_{n=0}^{N-1}(\tilde{f}(x_n x_{\max}) - \tilde{f}(x_{n+1}x_{\max}))\xi_{n+1}J_1(x_{\max}y_{\max}y\xi_{n+1}).
\end{aligned}
\tag{5.42}
$$

Here $\tilde{f}(xx_{\max})$ is piecewise constant on $]\xi_n, \xi_{n+1}[$ with $\xi_0 = 0$, $\xi_{N-1} = 1$. This function is chosen so that $\tilde{f}(\xi_n x_{\max}) = f(\xi_n x_{\max})$. This choice is quite obvious since $\tilde{f}$ is supposed to approximate the original function f. Additionally, $x_n \in]\xi_n, \xi_{n+1}[$. The points ξ_n, x_n and y_n are chosen in such a way, that expression (5.42) can be expressed as a "discrete correlation". To do so, the ξ_n are set to $\xi_n = e^{\alpha(n-N)}$ and $\xi_0 = 0$. Furthermore, the $y_n = (1+e^{\alpha})\frac{e^{\alpha(n-N)}}{2}$ for $n \in \{0, 1, \ldots, N-1\}$ and $x_0 = \frac{e^{\alpha(1-N)}}{2}$, $x_n = y_n$ for $n \in \{1, 2, \ldots, N-1\}$. With all these definitions, expression (5.42) can be rewritten as

$$
\begin{aligned}
g(y_n y_{\max}) = \frac{1}{2\pi}\frac{x_{\max}}{y_{\max}}\sum_{n=0}^{N-1}(\tilde{f}(x_n x_{\max}) - \tilde{f}(x_{n+1}x_{\max}))e^{2\alpha(n+1-N)} \\
\frac{J_1(x_0 x_{\max} y_{\max} e^{\alpha(n+m+1-N)})}{x_0 e^{\alpha(n+m+1-N)}}.
\end{aligned}
\tag{5.43}
$$

This expression can now be evaluated numerically ($f(x_N) = 0$). The equation (5.43) is constructed in such a way that it is a "discrete correlation" (compare [7] page 198–223). Now equation (5.43) can be rewritten in the following way:

$$
g(y_n y_{\max}) = \frac{1}{2\pi}\frac{x_{\max}}{y_{\max}}\sum_{n=0}^{N-1} h(n)k(n+m) = \frac{1}{2\pi}\frac{x_{\max}}{y_{\max}}\mathrm{FFT}(\mathrm{FFT}(h)\mathrm{IFFT}(k)).
\tag{5.44}
$$

Here, FFT and IFFT are the fast Fourier transform and the inverse fast Fourier transform, respectively. These are defined by

$$\mathrm{FFT}(h) = \sum_{n=0}^{N-1} h(n) e^{2\pi i \frac{nk}{N}} \quad \text{with} \quad k \in \{0, 1, \ldots, N-1\} \tag{5.45}$$

and

$$\mathrm{IFFT}(h) = \frac{1}{N} \sum_{n=0}^{N-1} h(n) e^{-2\pi i \frac{nk}{N}} \quad \text{with} \quad k \in \{0, 1, \ldots, N-1\}. \tag{5.46}$$

$\mathrm{FFT}(h)$ and $\mathrm{IFFT}(h)$ simply assign a vector of N numbers to another vector of N numbers. The product in equation (5.44) is a pointwise product. In the actual case of equation (5.43), the vectors are defined in the following way:

$$h(n) = \begin{cases} (\tilde{f}(x_n x_{\max}) - \tilde{f}(x_{n+1} x_{\max})) e^{2\alpha(n+1-N)} & n \in \{0, 1, \ldots, N-1\} \\ 0 \quad n \in \{N, N+1, \ldots, 2N-1\} \end{cases} \tag{5.47}$$

and

$$k(n) = \frac{J_1(x_{\max} y_{\max} e^{\alpha(n+1-N)})}{y_{\max} e^{\alpha(n+1-N)}} \quad n \in \{0, 1, \ldots, 2N-1\}. \tag{5.48}$$

The parameter α is (more or less arbitrarily) chosen in such a way that the first and the last interval have the same size. With this condition, α can be evaluated from the equation

$$\alpha = \frac{-\ln(1 - e^{-\alpha})}{N-1} \tag{5.49}$$

(in the original work [45] one sign is wrong). For a fixed partition $\{x_{\max} \xi_n\}$ of the interval $[0, x_{\max}]$, the expression $\mathrm{IFFT}(k)$ is independent of the function f that is transformed. Thus $\mathrm{IFFT}(k)$ must only be determined once for a given partition. The Hankel transform is now reduced to two fast Fourier transforms. How this method can be generalised for Hankel transformations of order 1 is sketched in the following paragraph. Due to the special structure of equation (2.87), it is advisable to modify the Hankel transform integral by a factor x^m:

$$g_m(y) \stackrel{\text{def}}{=} \frac{1}{2\pi} \int_0^\infty x^{m+1} f(x) J_m(xy) dx. \tag{5.50}$$

For instance, the equation (5.50) is replaced by:

$$
\begin{aligned}
g_1(yy_{\max}) = \frac{1}{2\pi}\int_0^{x_{\max}} x^2\tilde{f}(x)J_1(y_{\max}xy)dx = \\
\frac{1}{2\pi}\int_0^{1} x_{\max}^3 x^2\tilde{f}(xx_{\max})J_1(x_{\max}y_{\max}xy)dx = \\
\frac{1}{2\pi}\sum_{n=0}^{N-1} x_{\max}^3\int_{\xi_n}^{\xi_{n+1}} x^2\tilde{f}(xx_{\max})J_1(x_{\max}y_{\max}xy)dx = \\
\frac{1}{2\pi}\sum_{n=0}^{N-1}\frac{\tilde{f}(x_nx_{\max})x_{\max}^2}{y_{\max}y}(\xi_{n+1}^2J_2(x_{\max}y_{\max}y\xi_{n+1})- \\
\xi_n^2J_2(x_{\max}y_{\max}y\xi_n)) = \\
\frac{x_{\max}^2}{2\pi y_{\max}y}\sum_{n=0}^{N-1}(\tilde{f}(x_nx_{\max})-\tilde{f}(x_{n+1}x_{\max}))\xi_{n+1}^2J_2(x_{\max}y_{\max}y\xi_{n+1}).
\end{aligned}
\tag{5.51}
$$

The main limitation of this algorithm is that the function $f(x)$ is sampled to the step function $\tilde{f}(x)$ at fixed sample points ξ_n. It would be a great improvement if the sample points could be arbitrary. To improve accuracy, the samples would be denser where the function is drastically changing and sparser where the function is relatively constant. In this algorithm, the fixed sample points are essential since otherwise, equation (5.43) is no more a "discrete correlation". Nonetheless, an arbitrary choice of sampling points can be achieved by distorting the coordinate system (see [43]). The implementation of such an algorithm is much more intricate. A relatively straight forward extension of this algorithm is to transform cubic splines instead of stepwise constant functions. This may be promising since the Hankel transform is very much related to the Fourier transform — in fact, it can be expressed as a two–dimensional Fourier transform. Let g be the Fourier transform of f and let $\tilde{g}$ be the Fourier transform of $\tilde{f}$, then from Parseval's identity ([33] page 324) it follows that:

$$
\begin{aligned}
\| f-\tilde{f}\|_2 \stackrel{\text{def}}{=} \int_{\mathbb{R}^n}|f(x)-\tilde{f}(x)|^2dx^n = \\
\frac{1}{(2\pi)^n}\int_{\mathbb{R}^n}|g(x)-\tilde{g}(x)|^2dx^n = \frac{1}{(2\pi)^n}\|g-\tilde{g}\|_2 .
\end{aligned}
\tag{5.52}
$$

5.3 Evaluation of $\mathcal{Y}_{l-m}(\partial_{\mathbf{r}})G_{lm}(\mathbf{r},\mathbf{r}',E)$

As in section 2.5.3, this expression can be simplified by using the Fourier transform. Using equation (2.77), it is found that

$$\mathcal{Y}_{l-m}(\partial_{\mathbf{r}})G_{lm}(\mathbf{r},\mathbf{r}',E) = \frac{1}{(2\pi\hbar)^2}\int_{\mathbb{R}^2}\mathcal{Y}_{l-m}(\partial_{\mathbf{r}})\tilde{G}_{lm}(p,q,z,z',E) \\ e^{i\frac{p(x-x')}{\hbar}}e^{i\frac{q(y-y')}{\hbar}}dpdq. \tag{5.53}$$

Now again the x, y dependence is fully absorbed in the exponential factors. Thus the operator $\mathcal{Y}_{l-m}(\partial_{\mathbf{r}})$ can be recast to

$$\frac{1}{(2\pi\hbar)^2}\int_{\mathbb{R}^2}\mathcal{Y}_{l-m}(\partial_{\mathbf{r}})\tilde{G}_{lm}(p,q,z,z',E)e^{i\frac{p(x-x')}{\hbar}}e^{i\frac{q(y-y')}{\hbar}}dpdq = \\ \frac{1}{(2\pi\hbar)^2}\int_{\mathbb{R}^2}\mathcal{Y}_{l-m}\left(-\frac{p}{i\hbar},-\frac{q}{i\hbar},\partial_{z'}\right)\tilde{G}_{lm}(p,q,z,z',E)e^{i\frac{p(x-x')}{\hbar}}e^{i\frac{q(y-y')}{\hbar}}dpdq. \tag{5.54}$$

Substituting equation (2.79) in the above expression leads to:

$$\mathcal{Y}_{l-m}(\partial_{\mathbf{r}})G_{lm}(\mathbf{r},\mathbf{r}',E) = \frac{1}{(2\pi\hbar)^2}\int_{\mathbb{R}^2}\mathcal{Y}_{l-m}\left(-\frac{p}{i\hbar},-\frac{q}{i\hbar},\partial_{z'}\right)\mathcal{Y}_{lm}\left(\frac{p}{i\hbar},\frac{q}{i\hbar},\partial_{z'}\right) \\ G_{\mathrm{l}}\left(z,z',E-\frac{p^2+q^2}{2M}\right)e^{i\frac{p(x-x')}{\hbar}}e^{i\frac{q(y-y')}{\hbar}}dpdq. \tag{5.55}$$

From now on the remaining simplifications are straight forward and analogous to these in section 2.5.3. The variable transformation as defined by equation (2.80) and (2.81) gives

$$G_{lm}(\mathbf{r},\mathbf{r}',E) = \frac{1}{(2\pi)^2}\int_0^{\infty}\int_0^{2\pi}\mathcal{Y}_{l-m}\left(-\frac{k\cos\theta}{i},-\frac{k\sin\theta}{i},\partial_z\right) \\ \mathcal{Y}_{lm}\left(\frac{k\cos\theta}{i},\frac{k\sin\theta}{i},\partial_{z'}\right)G_{\mathrm{l}}\left(z,z',E-\frac{\hbar^2k^2}{2M}\right)e^{ik\rho\cos(\theta-\phi)}kd\theta dk. \tag{5.56}$$

With equation (2.84), the product of the spherical harmonics can be recast in the form:

$$\mathcal{Y}_{l-m}\Big(-\frac{k\cos\theta}{i},-\frac{k\sin\theta}{i},\partial_z\Big)\mathcal{Y}_{lm}\Big(\frac{k\cos\theta}{i},\frac{k\sin\theta}{i},\partial_{z'}\Big)=\frac{(2l+1)(l-m)!(l+m)!}{4\pi 2^{2l}(l!)^2}$$
$$\sum_{\substack{a-c=m\\ a+b+c=l\\ a,b,c\in\mathbb{Z}_0^+}}\frac{l!}{a!b!c!}\left(\Big(\frac{k\cos\theta}{i}\Big)^2+\Big(\frac{k\sin\theta}{i}\Big)^2\right)^a(2\partial_z)^b(-1)^c\cdot$$
$$\sum_{\substack{c-a=m\\ a+b+c=l\\ a,b,c\in\mathbb{Z}_0^+}}\frac{l!}{a!b!c!}\left(\Big(\frac{k\cos\theta}{i}\Big)^2+\Big(\frac{k\sin\theta}{i}\Big)^2\right)^a(2\partial_{z'})^b(-1)^c=$$
$$\frac{(2l+1)(l-m)!(l+m)!}{4\pi 2^{2l}}\sum_{\substack{a-c=m\\ a+b+c=l\\ a,b,c\in\mathbb{Z}_0^+}}\frac{1}{a!b!c!}(-1)^a k^{2a}(2\partial_z)^b(-1)^c\cdot$$
$$\sum_{\substack{c-a=m\\ a+b+c=l\\ a,b,c\in\mathbb{Z}_0^+}}\frac{1}{a!b!c!}(-1)^a k^{2a}(2\partial_{z'})^b(-1)^c. \tag{5.57}$$

This and equation (2.86) lead to the final expression:

$$\mathcal{Y}_{l-m}(\partial_{\mathbf{r}})G_{lm}(\mathbf{r},\mathbf{r}',E)=\frac{(2l+1)(l-m)!(l+m)!}{\pi^2 2^{2l+3}}\int_0^\infty kJ_m(k\rho)$$
$$\left(\sum_{\substack{c-a=m\\ a+b+c=l\\ a,b,c\in\mathbb{Z}_0^+}}\frac{1}{a!b!c!}k^{2c}(2\partial_z)^b\cdot\sum_{\substack{c-a=m\\ a+b+c=l\\ a,b,c\in\mathbb{Z}_0^+}}\frac{1}{a!b!c!}k^{2a}(2\partial_{z'})^b\right)G_1\Big(z,z',E-\frac{\hbar^2k^2}{2M}\Big)dk. \tag{5.58}$$

5.4 About the regularisation

The formula for the diagonal elements of $\mathbf{C}$

$$(\mathbf{C}(E))_{jj}=\big[\partial_{|\mathbf{r}-\mathbf{r}_j|}|\mathbf{r}-\mathbf{r}_j|G(\mathbf{r},\mathbf{r}_j,E)\big]_{\mathbf{r}=\mathbf{r}_j} \tag{5.59}$$

is not applicable for numerical purposes. If the potential is analytic, it can be shown that the three–dimensional Green's function has the following structure

$$G(\mathbf{r},\mathbf{r}',E)=-\frac{M}{2\pi\hbar^2}\frac{f(\mathbf{r},\mathbf{r}')}{|\mathbf{r}-\mathbf{r}'|}+g(\mathbf{r},\mathbf{r}'), \tag{5.60}$$

where $g(\mathbf{r},\mathbf{r}')$ is an analytic function. The function $f(\mathbf{r},\mathbf{r}')$ has the following structure:

$$f(\mathbf{r},\mathbf{r}') = 1 - \frac{M\big(E-U(\mathbf{r}')\big)}{\hbar^2}(\mathbf{r}-\mathbf{r}')^2 + \mathcal{O}\big((\mathbf{r}-\mathbf{r}')_i^3\big). \tag{5.61}$$

By definition, any analytic function h can be expressed as a Taylor series

$$h(\mathbf{r}_k+(\mathbf{r}-\mathbf{r}_k),\mathbf{r}') = \sum_{n=0}^{\infty}\frac{1}{n!}|\mathbf{r}-\mathbf{r}_k|^n\big(\mathbf{e}_{\mathbf{r}-\mathbf{r}_k}\cdot\nabla_{\mathbf{r}_k}\big)^n h(\mathbf{r}_k,\mathbf{r}'). \tag{5.62}$$

In the above expansion, the second argument remains constant, thus the differentiation is only applied to the first argument. Now it is obvious that for any analytic function $g(\mathbf{r},\mathbf{r}')$

$$\lim_{\mathbf{r}\to\mathbf{r}_k}\partial_{|\mathbf{r}-\mathbf{r}_k|}\big(|\mathbf{r}-\mathbf{r}_k|g(\mathbf{r},\mathbf{r}')\big) = g(\mathbf{r}_k,\mathbf{r}') \tag{5.63}$$

holds. Furthermore,

$$\begin{aligned}&\lim_{\mathbf{r}\to\mathbf{r}_k}\partial_{|\mathbf{r}-\mathbf{r}_k|}\Big(|\mathbf{r}-\mathbf{r}_k|\frac{f(\mathbf{r},\mathbf{r}_k)}{|\mathbf{r}-\mathbf{r}_k|}\Big) = \lim_{\mathbf{r}\to\mathbf{r}_k}\partial_{|\mathbf{r}-\mathbf{r}_k|}f(\mathbf{r},\mathbf{r}_k) = \\ &\lim_{\mathbf{r}\to\mathbf{r}_k}\big(\mathbf{e}_{\mathbf{r}-\mathbf{r}_k}\cdot\nabla_{\mathbf{r}}\big)f(\mathbf{r},\mathbf{r}_k) = 0\end{aligned} \tag{5.64}$$

vanishes due to the special structure of the function f. Now the right hand term in equation (5.59) can be rewritten as:

$$\lim_{\mathbf{r}\to\mathbf{r}_k}\partial_{|\mathbf{r}-\mathbf{r}_k|}\big(|\mathbf{r}-\mathbf{r}_k|G(\mathbf{r},\mathbf{r}_k,E)\big) = f(\mathbf{r}_k,\mathbf{r}_k). \tag{5.65}$$

It should be emphasised that the identity (5.63) is true for any analytic function. The function $f(\mathbf{r},\mathbf{r}')$ can be written as

$$f(\mathbf{r},\mathbf{r}') = \frac{1}{2\pi}\int_0^\infty\Big(G_1\Big(z,z',E-\frac{(\hbar k)^2}{2M}\Big)+\frac{M}{\hbar^2}\frac{e^{-|z-z'|k}}{k}\Big)kJ_0(\rho k)\,dk, \tag{5.66}$$

where equation (5.60) is used. This finally leads to

$$(\mathbf{C}(E))_{jj} = \frac{1}{2\pi}\int_0^\infty\left(kG_1\left(z,z,E-\frac{(\hbar k)^2}{2M}\right)+\frac{M}{\hbar^2}\right)dk. \tag{5.67}$$

The diagonal matrix elements $(\mathbf{C}(E))_{jj}$ can now be calculated with a simple integration through (5.67).

5.5 The one–dimensional Green's function for small energies

Here an interesting method is described which further increases the accuracy of the Hankel transform. Since integrals of the following type

$$\int_0^\infty kJ_0(k\rho)G_1\Big(z,z',E-\frac{(\hbar k)^2}{2M}\Big)\,dk \tag{5.68}$$

must be evaluated numerically, it is important to consider the behaviour of the one–dimensional Green's function $G_1\big(z,z',E-\frac{(\hbar k)^2}{2M}\big)$ (for the potential $U(z)$) for large k. The basic idea is that the real part of the Green's function G_1 can be approximated for large k by

$$G_1^{\text{free}}=-\frac{M}{k_{\text{free}}\hbar^2}e^{-k_{\text{free}}|z-z'|}, \tag{5.69}$$

where

$$k_{\text{free}}=\sqrt{\frac{2M}{\hbar^2}\Big(U(\frac{z+z'}{2})-E\Big)+k^2}. \tag{5.70}$$

The imaginary part is proportional to the total current and is much more well behaved for small energies. For potentials with a lower bound (like the soft– and hard step potentials), the imaginary part is exactly 0 for $E\in]E_{\max},-\infty[$. The above approximation for the real part of the Green's function for small energies can be justified since the real part of the WKB one–dimensional Green's function in the tunnelling region is

$$G_1^{\text{WKB}}=-\frac{M}{\hbar^2}\frac{1}{\sqrt{\kappa(z_<,E)\kappa(z_>,E)}}e^{-\int_{z_<}^{z_>}\kappa(x,E)\,dx}, \tag{5.71}$$

where

$$\kappa(x,E)=\sqrt{\frac{2M}{\hbar^2}\big(U(x)-E\big)+k^2}. \tag{5.72}$$

Assuming that the potential $U(x)$ is monotone, it follows that $\kappa(x,E)$ is monotone with respect to x. From the mean value theorem it follows that there exists a point $y\in[z_<,z_>]$ such that $\sqrt{\kappa(z_<,E)\kappa(z_>,E)}=\kappa(y,E)$. On the other hand, it follows from the mean value theorem of integration theory that there exists a point $v\in[z_<,z_>]$ such that $\int_{z_<}^{z_>}\kappa(x,E)\,dx=(z_>-z_<)\kappa(v,E)$. A possible approximation would be to choose $v=y=\frac{z_<+z_>}{2}$. In the limit $k\to\infty$, this choice is definitely justified.

Thus in fact, it is not the function G_1 that is numerically Hankel transformed, but the function

$$G_1\Big(z, z', E - \frac{(\hbar k)^2}{2M}\Big) + \mathrm{Re}\Big(\frac{M}{\sqrt{k_c^2 + k^2}\hbar^2} e^{-\sqrt{k_c^2+k^2}|z-z'|}\Big), \tag{5.73}$$

where the constant k_c is given by:

$$k_c \stackrel{\mathrm{def}}{=} \sqrt{\frac{2M}{\hbar^2}\Big(U(\frac{z+z'}{2}) - E\Big)} \tag{5.74}$$

so that

$$k_{\mathrm{free}} = \sqrt{k_c^2 + k^2}. \tag{5.75}$$

For sake of clarity, let $h(z, z', \rho)$ be the Hankel transform of the function (5.73):

$$\begin{aligned} h(z, z', \rho) \stackrel{\mathrm{def}}{=} \frac{1}{2\pi} \int_0^\infty \Bigg(& G_1\Big(z, z', E - \frac{(\hbar k)^2}{2M}\Big) + \\ & \mathrm{Re}\Big(\frac{M}{\sqrt{k_c^2 + k^2}\hbar^2} e^{-\sqrt{k_c^2+k^2}|z-z'|}\Big)\Bigg) k J_0(k\rho) dk. \end{aligned} \tag{5.76}$$

In order to obtain the Hankel transform of G_1, that is G, the following function (the three–dimensional Green's function corresponding to G_1^{free}) must be added to $h(z, z', \rho)$:

$$G(z, z', \rho) = h(z, z', \rho) - \frac{M}{2\pi\hbar^2} \mathrm{Re}\Big(\frac{e^{-k_c|\mathbf{r}-\mathbf{r}'|}}{|\mathbf{r}-\mathbf{r}'|}\Big). \tag{5.77}$$

What makes the described method even more effective is that the function (5.73) even gives convergent results for $z = z'$. For the integral (5.67), only the real part of the following constant must be added to the transform of function (5.73):

$$\frac{1}{2\pi}\int_0^\infty \frac{M}{\sqrt{k_c^2 + k^2\hbar^2}} - \frac{M}{k\hbar^2} k dk = \frac{M}{2\pi\hbar^2}\Big[-k + \sqrt{k_c^2 + k^2}\Big]_0^\infty = -\frac{M k_c}{2\pi\hbar^2}. \tag{5.78}$$

Thus for the diagonal T–matrix elements the following constant must be added to h:

$$(\mathbf{C}(z, E))_{jj} = h(z, z, 0) + \mathrm{Re}\Big(\frac{M k_c}{2\pi\hbar^2}\Big). \tag{5.79}$$

The extension of the described method to multipoles is straight forward but cumbersome. The multipole Green's function G_{lm} is given by equation (2.87). The correction term that must be added to the numerical transform is determined by:

$$-\frac{M}{2\pi\hbar^2} \mathcal{Y}_{lm}\Big(\frac{\partial}{\partial \mathbf{r}'}\Big) \mathrm{Re}\Big(\frac{e^{-k_c|\mathbf{r}-\mathbf{r}'|}}{|\mathbf{r}-\mathbf{r}'|}\Big). \tag{5.80}$$

5.6 Summary: How to simulate an STM

For someone interested only in the implementation of the STM simulation, this section gives a comprehensive description of the employed methods.

At first, the mean tip–vacuum–probe potential $U_1(z)$ must be chosen (section 2.5.1). The program developed in this thesis offers three options: the triangular (section 5.1.3), the smooth (section 5.1.1), and the step barrier (section 5.1.2). When the probe harbours a two–dimensional electron gas, in the studied energy range a partially reflecting surface must be additionally introduced (see equation (3.4)). The atoms at the surface of the probe are described by zero range potentials. For more details see section 2.5.4.

With these preliminary measures, the model is set up. Now the multipole current is calculated in the following four steps:

At first, the three–dimensional multipole Green's function $G_{lm}(\mathbf{r}, \mathbf{r}', E)$ is determined. It is calculated from the one–dimensional Green's $G_1(z, z', E)$ function of the potential $U_1(z)$. (See section 2.5.3.) The following numerical methods are employed:

1. the ideas presented in section 5.5 to improve accuracy
2. the Hankel transform (section 5.2)

Next, the background current $Y_{l-m}(\partial_{\mathbf{r}})G_{lm}(\mathbf{r}, \mathbf{r}', E)$ is calculated as in section 5.3:

1. to improve accuracy, employ the ideas presented in section 5.5
2. employ the Hankel transform of section 5.2

Finally, the T–matrix (section 2.5.4) is calculated:

1. the diagonal T–matrix elements need special treatment as presented in section 5.4 and 5.5
2. employ the Hankel transform

From these quantities, the multipole current can be directly calculated by equation (2.110). The three–dimensional Green's functions are determined for all values of ρ at once. This is the fundamental property of the numerical Hankel transform (that is the reason why it is called a transform not an integral). Thus, the whole constant height image of the STM is easily calculated, since the T–matrix and the three–dimensional Green's function are only calculated once. To simulate corrugation images, the following method is most

effective: depending on the desired accuracy, at least 3 constant height images with the tip–probe distances z_0, $z_0 - 0.5$Å, $z_0 + 0.5$Å of the surface are calculated. From these three images, a constant current image can be easily calculated via interpolation. Since for this purpose an (at first) arbitrary current value must be selected, it is sensible to calculate the maximum and minimum current values for each constant height image. From these three current intervals, a reasonable current can be selected.

Chapter 6

The Kondo effect

For more then 70 years, it is known that the resistivity of dilute magnetic alloys has a completely different temperature dependence than normal metals. Typically, copper with small traces of iron was used for the experiments. While the temperature decreases, the resistivity reaches a minimum and then increases again with an $-\ln T$ dependence. This $-\ln T$ dependence does not continue indefinitely for low temperatures; instead, below a characteristic temperature T_k (Kondo temperature), it phases out. What is more important, as the temperature decreases, also the magnetic moment of the impurity — embedded in the ordinary metal — exhibits an "anomalous" behaviour. The magnetic susceptibility ceases to follow the Curie law at the temperature T_k, and rather saturates to a constant value at $T = 0$. A constant susceptibility at $T = 0$ is characteristic of a singlet state polarised by a magnetic field. The magnetic moment of the impurity is fully compensated and quenched by the conduction electrons of the host metal at very low temperatures. Thus magnetism ceases at low temperatures. This is also confirmed by an extra contribution to the specific heat, corresponding to an entropy change of the order of $k_b \ln 2$, for each magnetic impurity. Thus several properties appear to be anomalous in ordinary metals with dilute magnetic impurities. All these effects are collectively referred to as the "Kondo effect".

The simplest Hamiltonian that represents the interaction of a localised spin with the electrons of the host metal is:

$$\hat{H} = \sum_{\mathbf{k},\sigma} \epsilon_{\mathbf{k}} n_{\mathbf{k}\sigma} - \sum_{\mathbf{k},\mathbf{k}'} \frac{J_{\mathbf{k}\mathbf{k}'}}{\hbar^2} \left(\psi^\dagger_{\mathbf{k}'} \mathbf{S} \psi_{\mathbf{k}}\right) \cdot \left(\psi^\dagger_d \mathbf{S} \psi_d\right). \tag{6.1}$$

In equation (6.1), the two–component spinor operators that remove electrons from conduction and impurity states have been introduced:

$$\psi_{\mathbf{k}} = \begin{pmatrix} c_{\mathbf{k}\uparrow} \\ c_{\mathbf{k}\downarrow} \end{pmatrix}, \psi_d = \begin{pmatrix} c_{d\uparrow} \\ c_{d\downarrow} \end{pmatrix}. \tag{6.2}$$

The spin matrix operator is given by,

$$\mathbf{S} = \frac{\hbar\sigma}{2}, \tag{6.3}$$

where the σ's are the usual Pauli matrices,

$$\sigma_x = \begin{pmatrix} 0 & 1 \\ 1 & 0 \end{pmatrix}, \sigma_y = \begin{pmatrix} 0 & -i \\ i & 0 \end{pmatrix}, \sigma_z = \begin{pmatrix} 1 & 0 \\ 0 & -1 \end{pmatrix}. \tag{6.4}$$

Kondo solved the Hamiltonian (6.1) perturbatively up to the second order in J. He showed that a $-\ln T$ term appears in the scattering rate that arises between the conduction electrons and the localised spin. The reason why the Kondo problem was not completely solved until the early 1980's is that this perturbative solution of the Kondo problem is not valid for temperatures below the Kondo temperature.

The Hamiltonian given in equation (6.1) already assumes a definite impurity spin that is temperature independent. A more realistic approach would be to simply introduce a single energy level (usually the d or f–electron level) into the system that can only be occupied by a single electron. This f–electron level can only be occupied by a single electron due to a large Coulomb repulsion between two electrons occupying this level. The Hamiltonian with the features described is the so–called Anderson Hamiltonian, which is given by:

$$\hat{H} = \sum_{\mathbf{k},\sigma} \epsilon_{\mathbf{k}} n_{\mathbf{k}\sigma} - \sum_{\sigma} \epsilon_d n_{d\sigma} + \frac{1}{\sqrt{N}} \sum_{\mathbf{k},\sigma} \left(V_{\mathbf{k}d} c^{\dagger}_{\mathbf{k}\sigma} c_{d\sigma} + V^{*}_{\mathbf{k}d} c^{\dagger}_{d\sigma} c_{\mathbf{k}\sigma} \right) + U n_{d\uparrow} n_{d\downarrow}. \tag{6.5}$$

Shortly after the Kondo problem (6.1) was completely solved, the more general Anderson problem was also successfully tackled. The fourth term in equation (6.5) is the already mentioned Coulomb repulsion between f–electrons. The parameter U is assumed so high ($U \to \infty$) as to allow occupancy not higher than one of the f orbital.

6.1 Relationship between the total cross section and the impurity Green's function

The impurity Green's function can be directly derived from the Anderson Hamiltonian:

$$\hat{H} = \sum_{\mathbf{k},\sigma} \epsilon_{\mathbf{k}} n_{\mathbf{k}\sigma} - \sum_{\sigma} \epsilon_d n_{d\sigma} + \frac{1}{\sqrt{N}} \sum_{\mathbf{k},\sigma} \left(V_{\mathbf{k}d} c^{\dagger}_{\mathbf{k}\sigma} c_{d\sigma} + V^{*}_{\mathbf{k}d} c^{\dagger}_{d\sigma} c_{\mathbf{k}\sigma} \right) + U n_{d\uparrow} n_{d\downarrow}. \tag{6.6}$$

The retarded double–time Green's function $\langle\langle A(t_1) : B(t_2)\rangle\rangle$ for the operators A and B is defined by

$$\langle\langle A(t_1) : B(t_2)\rangle\rangle = -i\theta(t_1 - t_2)\langle[A(t_1), B(t_2)]_\eta\rangle, \tag{6.7}$$

where $[A, B]_\eta = AB + \eta BA$, and $\eta = +1$ for Fermi operators and $\eta = -1$ for Bose operators. The operators are in Heisenberg representation $A(t) = \exp(iH't)A\exp(-iH't)$, with $H' = H - \nu N_0$. Furthermore, $\langle \ldots \rangle$ denotes the usual thermal average:

$$\langle A\rangle = \frac{\mathrm{Tr}(e^{-\beta(H-\nu N_0)}A)}{\mathrm{Tr}\, e^{-\beta(H-\nu N_0)}}. \tag{6.8}$$

The Fourier transform $G_{i,j}(\omega)$ of the Green's function $\langle\langle A_i(t_1) : B_j(t_2)\rangle\rangle$ is given by

$$G_{i,j}(\omega^+) = \int_{-\infty}^{\infty} e^{i\omega^+(t_1-t_2)}\langle\langle A_i(t_1) : B_j(t_2)\rangle\rangle\, d(t_1 - t_2), \tag{6.9}$$

where $\omega^+ = \omega + is$, $s \to +0$. The double–time Green's functions satisfy the equation of motion:

$$\begin{aligned} i\frac{d}{dt_1}\langle\langle A(t_1) : B(t_2)\rangle\rangle =& \langle[A(t_1), B(t_2)]_\eta\rangle\delta(t_1 - t_2) + \\ &+ \langle\langle[A(t_1), H'(t_1)]_- : B(t_2)\rangle\rangle. \end{aligned} \tag{6.10}$$

Taking the Fourier transform of the above identity (6.10) leads to the equation of motion for the energy Green's functions:

$$E\langle\langle A : B\rangle\rangle_E = \hbar\langle[A, B]_\eta\rangle + \langle\langle[A, H']_- : B\rangle\rangle_E \tag{6.11}$$

The above equation of motion is not a differential equation any more but an algebraic equation. Applying this equation of motion to the operator combination $c_{\mathbf{k}\sigma}, c^\dagger_{d\sigma}$ leads to the following equation:

$$(\omega - \epsilon_{\mathbf{k}})G_{\mathbf{k}\sigma,d\sigma}(\omega) = V^*_{\mathbf{k}}G_{d\sigma,d\sigma}(\omega). \tag{6.12}$$

The operator combination $c_{\mathbf{k}\sigma}$, $c^\dagger_{\mathbf{k}'\sigma}$ and $c_{d\sigma}, c^\dagger_{\mathbf{k}\sigma}$ can be treated in the very same way:

$$(\omega - \epsilon_{\mathbf{k}})G_{\mathbf{k}\sigma,\mathbf{k}'\sigma}(\omega) = \delta_{\mathbf{k},\mathbf{k}'} + V^*_{\mathbf{k}}G_{d\sigma,\mathbf{k}'\sigma}(\omega) \tag{6.13}$$

$$(\omega - \epsilon_{\mathbf{k}'})G_{d\sigma,\mathbf{k}'\sigma}(\omega) = V_{\mathbf{k}'}G_{d\sigma,d\sigma}(\omega). \tag{6.14}$$

From equations (6.12), (6.13) and (6.14), the following important identity is easily derived:

$$G_{\mathbf{k}\sigma,\mathbf{k}'\sigma} = \frac{\delta_{\mathbf{k},\mathbf{k}'}}{\omega - \epsilon_{\mathbf{k}}} + \frac{V_{\mathbf{k}}^*}{\omega - \epsilon_{\mathbf{k}}} G_{d\sigma,d\sigma}(\omega) \frac{V_{\mathbf{k}'}}{\omega - \epsilon_{\mathbf{k}'}} \tag{6.15}$$

The function

$$G^0_{\mathbf{k}\sigma,\mathbf{k}'\sigma}(\omega) = \frac{\delta_{\mathbf{k},\mathbf{k}'}}{\omega - \epsilon_{\mathbf{k}}} \tag{6.16}$$

is the Green's function for the Hamiltonian

$$\hat{H}^0 = \sum_{\mathbf{k},\sigma} \epsilon_{\mathbf{k}} n_{\mathbf{k}\sigma} - \sum_{\sigma} \epsilon_d n_{d\sigma}. \tag{6.17}$$

Thus the T-matrix can be identified from equation (6.15) as:

$$T_{\mathbf{k}\sigma,\mathbf{k}'\sigma}(\omega) = V_{\mathbf{k}}^* G_{d\sigma,d\sigma}(\omega) V_{\mathbf{k}'}. \tag{6.18}$$

It should be stated that the Anderson model cannot be solved exactly by this method. The equation of motion for the operator combination $c_{d\sigma}, c^\dagger_{d\sigma}$ leads to:

$$(\omega - \epsilon_d) G_{d\sigma d\sigma}(\omega) - U\Gamma_{dd}(\omega) = 1 + \sum_{\mathbf{k}} V_{\mathbf{k}} G_{\mathbf{k}\sigma d\sigma}(\omega), \tag{6.19}$$

where the following commutator was employed:

$$[c_{d\sigma}, H']_- = (\epsilon_d - \mu) c_{d\sigma} + \sum_{\mathbf{k}} V_{\mathbf{k}} c_{\mathbf{k}\sigma} + U c_{d\sigma} c^\dagger_{d-\sigma} c_{d-\sigma}. \tag{6.20}$$

The problem is that equation (6.19) includes a higher order Green's function $\Gamma_{dd}(\omega)$ that is defined by:

$$\Gamma_{dd}(\omega) \stackrel{\text{def}}{=} \langle\langle c_{d\sigma} n_{d-\sigma} : c^\dagger_{d\sigma} \rangle\rangle. \tag{6.21}$$

On the other hand, the optical theorem directly relates the total cross section with the imaginary part of the T–matrix:

$$\sigma_{\text{tot}} = -\frac{2M}{\hbar^2 k} (2\pi)^3 \operatorname{Im}\big(T_{\mathbf{k}\sigma,\mathbf{k}\sigma}(\omega)\big) \tag{6.22}$$

Thus the energy dependent total cross section of a Kondo impurity is given by:

$$\sigma_{\text{tot}} = -\frac{2M}{\hbar^2 k} (2\pi)^3 |V_{\mathbf{k}}|^2 \operatorname{Im}\big(G_{d\sigma,d\sigma}(\omega)\big). \tag{6.23}$$

The imaginary part of the retarded Green's function $G_{d\sigma,d\sigma}$ is directy proportional to the spectral density $S_{d\sigma d\sigma}$ (see figure 6.1) of the impurity:

$$S_{d\sigma d\sigma}(\omega) = -\frac{1}{\pi}\,\mathrm{Im}\big(G_{d\sigma,d\sigma}(\omega)\big). \tag{6.24}$$

In case of an STM measurement, the incident particles are the one particle states $c_{\mathbf{k}\sigma}|0\rangle$. The dispersion relation E that these incident particles obey can at once be derived from the Hamiltonian (6.5): $E(\mathbf{k}) = \epsilon_{\mathbf{k}}$. This dispersion relation (band structure) combined with equation (6.23) shows that the total cross section depends only on the energy of the incident electrons. It can be shown that the Green's function $G_{d\sigma,d\sigma}(\omega)$ has a sharp resonance at (or more precisely, very close to) the Fermi level. How this resonance appears will be made plausible in section 6.2. Extensive numerical treatments of the Kondo problem show that the shape of this resonance can be approximated by a Lorentzian. As long as the dispersion relation of the electrons behaves relatively smooth within the small Kondo resonance region, the total cross section will also have a Lorentzian behaviour.

Since the Kondo impurity only reveals itself through its scattering properties by an (spin) unpolarised beam of electrons, it is possible to introduce a fake Kondo impurity by simply matching the total cross sections of the Kondo impurity and the fake impurity. For a zero–range potential, the following relationship between T–matrix and the total cross section was found for a single adatom at position $\mathbf{r}_A$ (see equation (2.102), (2.95) and equation (2.107):

$$\mathbf{T}(E) = \left(\frac{M}{\hbar^2}\frac{1}{\sqrt{\pi\sigma_{\mathrm{tot}}}} - \big[\partial_{|\mathbf{r}-\mathbf{r}_A|}|\mathbf{r}-\mathbf{r}_A|G^{\mathrm{w}}(\mathbf{r},\mathbf{r}_A,E)\big]_{\mathbf{r}=\mathbf{r}_A}\right)^{-1}. \tag{6.25}$$

This equation (6.25) can now be proposed as a generalised relationship between the T–matrix and the total cross section for zero–range potentials. Of course, it must be verified that a resonance in σ_{tot} at energy E_r does in fact lead to a resonance in the conductivity of the STM at the same energy E_r.

6.2 The zero band width Anderson model

The zero band width Anderson model is a drastic simplification of the full Anderson Hamiltonian. Nonetheless, it has some fundamental properties in common with the full Hamiltonian. Especially the appearance of a resonance at the Fermi energy can be understood within this model. Any direct solution (a precise solution based on verified theoremes of quantum mechanics) of the

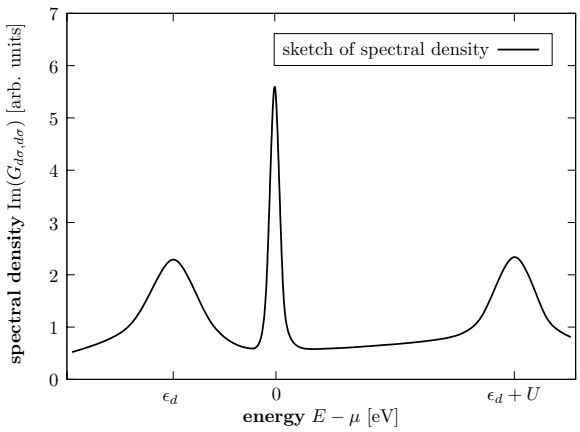

Figure 6.1: This is the spectral density of the Anderson impurity model in the Kondo regime. This figure is not based on an actual calculation but illustrates the central features of the spectral density. The broad peaks near ϵ_d and ϵ_d+U are due to single–particle energy levels of the impurity. They are broadened by coupling to the Fermi sea. The very narrow central peak is a many–body resonance (also called the "Kondo peak"). Its width is proportional to the Kondo temperature.

Anderson Hamiltonian includes extensive numerical calculations (for details of the different methods see [28]).

Here a very simple model is considered in which the conduction electrons are described by a single state at the Fermi level (zero band width limit). The simplicity of the model is such that the many–body states can be calculated by diagonalisation of matrices no greater than 3×3. Nevertheless, the results do give some insight as to why a singlet ground state occurs in the strong correlation limit, and why states with small weight are seen in the vicinity of the Fermi level when the impurity d or f electron is added or removed. The model is the non–degenerate Anderson model with a single conduction band state at the Fermi level ϵ_F:

$$\hat{H} = \sum_\sigma \epsilon_F n_{1\sigma} - \sum_\sigma \epsilon_d n_{d\sigma} + V\sum_\sigma \left(c^\dagger_{1\sigma}c_{d\sigma} + c^\dagger_{d\sigma}c_{1\sigma}\right) + U n_{d\uparrow}n_{d\downarrow}. \qquad (6.26)$$

A correctly antisymmetrised basis for one particle states of this problem is given by the following four operators:

$$c^\dagger_{1\downarrow}, \quad c^\dagger_{1\uparrow}, \quad c^\dagger_{d\downarrow}, \quad c^\dagger_{d\uparrow}. \qquad (6.27)$$

These four states are obviously eigenstates of S^2 and S_z with the eigenvalues:

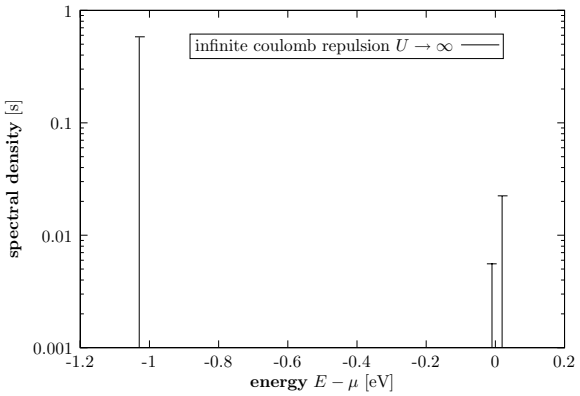

Figure 6.2: A schematic representation of the excitations from the ground state of the zero band width Anderson model. Here, the limit where the Coulomb repulsion is infinitely strong $U \to \infty$ is considered. Although this approximation is often employed, it is only valid in a certain energy regime. The Coulomb repulsion for iron group impurities is $U \approx 10$eV and for rare earth impurities $U \approx 15$eV. The other parameters have been given typical values: $\epsilon_F = \mu$, $\epsilon_F - \epsilon_d = 1$eV, $V = 0.1$eV and $U = 10$eV. A resonance close to the impurity level ϵ_d even appears in the well known model (6.1) where $U = 0$ [24], (page 452). This resonance close to the impurity level is thus expected. On the other hand, the appearance of the Kondo resonance close to the Fermi energy is a characteristic of the Anderson model. The Kondo resonance is due to the peculiar ground state $\mathsf{e}_2^\dagger|0\rangle$ (see equation (6.58)) of the system.

state	S^2	S_z
$c_{1\downarrow}^\dagger$	1/2	$-1/2$
$c_{1\uparrow}^\dagger$	1/2	$+1/2$
$c_{d\downarrow}^\dagger$	1/2	$-1/2$
$c_{d\uparrow}^\dagger$	1/2	$+1/2$

Therefore the operators S^2 and S_z are given by:

$$S^2 = \hbar^2 \frac{3}{4}\big(c_{1\downarrow}^\dagger c_{1\downarrow} + c_{1\uparrow}^\dagger c_{1\uparrow} + c_{d\downarrow}^\dagger c_{d\downarrow} + c_{d\uparrow}^\dagger c_{d\uparrow}\big) \tag{6.28}$$

and

$$S_z = \hbar \frac{1}{2}\big(c_{1\uparrow}^\dagger c_{1\uparrow} + c_{d\uparrow}^\dagger c_{d\uparrow} - c_{1\downarrow}^\dagger c_{1\downarrow} - c_{d\downarrow}^\dagger c_{d\downarrow}\big). \tag{6.29}$$

A simple calculation shows that

$$[H, S^2] = 0 \qquad \text{and} \qquad [H, S_z] = 0. \tag{6.30}$$

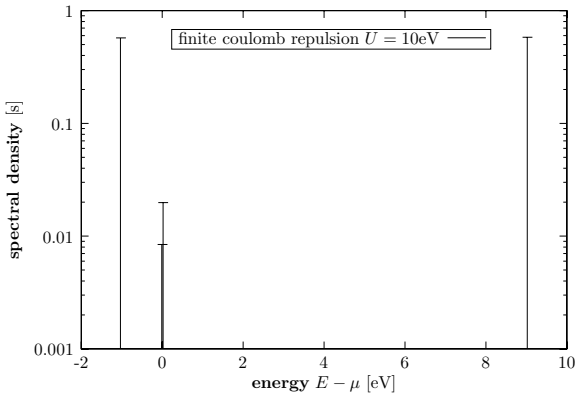

Figure 6.3: A schematic representation of the excitations from the ground state of the zero band width Anderson model. The parameters have typical values: The hybridisation parameter has a magnitude of $V \approx 10 - 100$meV. The Coulomb repulsion for iron group impurities is $U \approx 10$eV, and for rare earth impurities $U \approx 15$eV. The impurity level is typically $\epsilon_F - \epsilon_d \approx 1$eV below the Fermi energy. The following choice of parameters has been employed to calculate this picture: $\epsilon_F = \mu$, $\epsilon_F - \epsilon_d = 1$eV, $V = 0.1$eV and $U = 10$eV. While the resonances close to the impurity level ϵ_d and a resonance close to U can be expected, the appearance of two small but finite resonances (the Kondo resonance) very close to the Fermi energy may be surprising.

Therefore, the operators H, S^2, S_z have a common set of eigenstates. The operator S_z splits the four–dimensional vector space in two two–dimensional vector spaces.

The exact eigenbasis of H in these two–fold degenerate S_z–eigenspaces is now determined. At first, the spin–up space $(c^\dagger_{1\uparrow}, c^\dagger_{d\uparrow})$ is considered. The normalised eigenstates must have the following structure:

$$\mathsf{a}_{\pm\uparrow}|0\rangle = A_\pm c^\dagger_{d\uparrow}|0\rangle + B_\pm c^\dagger_{1\uparrow}|0\rangle \tag{6.31}$$

with

$$A_\pm^2 + B_\pm^2 = 1. \tag{6.32}$$

With these states, the stationary Schrödinger equation is easily written as a matrix equation:

$$\begin{pmatrix} \epsilon_d & V \\ V & \epsilon_F \end{pmatrix} \begin{pmatrix} A_\pm \\ B_\pm \end{pmatrix} = E \cdot \begin{pmatrix} A_\pm \\ B_\pm \end{pmatrix}. \tag{6.33}$$

From this matrix equation, the eigenvalues can be straight forward deter-

mined:

$$E_{\pm} = \frac{\epsilon_F + \epsilon_d \pm \sqrt{(\epsilon_F - \epsilon_d)^2 + 4V^2}}{2}. \tag{6.34}$$

The evaluation of the normalised eigenstates is cumbersome, but not difficult:

$$A_+ = \frac{\epsilon_d - \epsilon_F + \sqrt{4V^2 + (\epsilon_F - \epsilon_d)^2}}{\sqrt{4V^2 + \left(\epsilon_d - \epsilon_F + \sqrt{4V^2 + (\epsilon_F - \epsilon_d)^2}\right)^2}} \tag{6.35}$$

$$B_+ = \frac{2V}{\sqrt{4V^2 + \left(\epsilon_d - \epsilon_F + \sqrt{4V^2 + (\epsilon_F - \epsilon_d)^2}\right)^2}} \tag{6.36}$$

and

$$A_- = -\frac{\epsilon_F - \epsilon_d + \sqrt{4V^2 + (\epsilon_F - \epsilon_d)^2}}{\sqrt{4V^2 + \left(\epsilon_F - \epsilon_d + \sqrt{4V^2 + (\epsilon_F - \epsilon_d)^2}\right)^2}} \tag{6.37}$$

$$B_- = \frac{2V}{\sqrt{4V^2 + \left(\epsilon_F - \epsilon_d + \sqrt{4V^2 + (\epsilon_F - \epsilon_d)^2}\right)^2}}. \tag{6.38}$$

A direct calculation shows that these states are orthonormal. The spin–down space $(c^\dagger_{1\downarrow}, c^\dagger_{d\downarrow})$ is treated in exactly the same way. The normalised eigenstates are given by:

$$\mathsf{a}_{\pm\downarrow}|0\rangle = C_\pm c^\dagger_{d\downarrow}|0\rangle + D_\pm c^\dagger_{1\downarrow}|0\rangle. \tag{6.39}$$

Since the Hamiltonian treats spin–up particles in exactly the same way as spin down particles, it is immediately seen that:

$$A_\pm = C_\pm \quad \text{and} \quad B_\pm = D_\pm. \tag{6.40}$$

A correctly antisymmetrised basis for two particle states of this problem is given by the following six operators:

$$c^\dagger_{1\downarrow}c^\dagger_{1\uparrow}, \quad c^\dagger_{1\downarrow}c^\dagger_{d\downarrow}, \quad c^\dagger_{1\downarrow}c^\dagger_{d\uparrow}, \quad c^\dagger_{1\uparrow}c^\dagger_{d\downarrow}, \quad c^\dagger_{1\uparrow}c^\dagger_{d\uparrow}, \quad c^\dagger_{d\downarrow}c^\dagger_{d\uparrow}. \tag{6.41}$$

The eigenstates of the total spin operator are as follows:

state	S^2	S_z
$c^\dagger_{1\downarrow}c^\dagger_{1\uparrow}$	0	0
$c^\dagger_{d\downarrow}c^\dagger_{d\uparrow}$	0	0
$\frac{c^\dagger_{1\downarrow}c^\dagger_{d\uparrow} - c^\dagger_{1\uparrow}c^\dagger_{d\downarrow}}{\sqrt{2}}$	0	0
$c^\dagger_{1\uparrow}c^\dagger_{d\uparrow}$	1	1
$\frac{c^\dagger_{1\downarrow}c^\dagger_{d\uparrow} + c^\dagger_{1\uparrow}c^\dagger_{d\downarrow}}{\sqrt{2}}$	1	0
$c^\dagger_{1\downarrow}c^\dagger_{d\downarrow}$	1	-1

From these states and their corresponding eigenvalues, it is now easy to construct the the operators S^2 and S_z:

$$S^2 = \hbar^2 \sum_\sigma \big(2c^\dagger_{1\sigma}c^\dagger_{d\sigma}c_{1\sigma}c_{d\sigma} + c^\dagger_{1\sigma}c^\dagger_{d-\sigma}c_{1\sigma}c_{d-\sigma} + c^\dagger_{1\sigma}c^\dagger_{d-\sigma}c_{1-\sigma}c_{d\sigma}\big) \tag{6.42}$$

and

$$S_z = \hbar\big(c^\dagger_{1\uparrow}c^\dagger_{d\uparrow}c_{1\uparrow}c_{d\uparrow} - c^\dagger_{1\downarrow}c^\dagger_{d\downarrow}c_{1\downarrow}c_{d\downarrow}\big). \tag{6.43}$$

Again, a simple calculation shows that

$$[H, S^2] = 0 \qquad \text{and} \qquad [H, S_z] = 0. \tag{6.44}$$

From the equations (6.44) it is immediately seen that the following obviously normalised states are solutions of the Schrödinger equation:

$$\mathsf{b}^\dagger|0\rangle \stackrel{\text{def}}{=} c^\dagger_{1\uparrow}c^\dagger_{d\uparrow}|0\rangle = \mathsf{a}^\dagger_{+\uparrow}\mathsf{a}^\dagger_{-\uparrow}|0\rangle \tag{6.45}$$

$$\mathsf{c}^\dagger|0\rangle \stackrel{\text{def}}{=} \frac{c^\dagger_{1\downarrow}c^\dagger_{d\uparrow} + c^\dagger_{1\uparrow}c^\dagger_{d\downarrow}}{\sqrt{2}}|0\rangle = \frac{\mathsf{a}^\dagger_{+\uparrow}\mathsf{a}^\dagger_{-\downarrow} + \mathsf{a}^\dagger_{+\downarrow}\mathsf{a}^\dagger_{-\uparrow}}{\sqrt{2}}|0\rangle \tag{6.46}$$

$$\mathsf{d}^\dagger|0\rangle \stackrel{\text{def}}{=} c^\dagger_{1\downarrow}c^\dagger_{d\downarrow}|0\rangle = \mathsf{a}^\dagger_{+\downarrow}\mathsf{a}^\dagger_{-\downarrow}|0\rangle. \tag{6.47}$$

All three states have the same degenerate energy eigenvalue $\epsilon_F + \epsilon_d = E_+ + E_-$. The triplet states are thus merely products of single particle states. There are three possible singlet states built up from the states, $c^\dagger_{1\uparrow}c^\dagger_{1\downarrow}|0\rangle$, $(c^\dagger_{1\uparrow}c^\dagger_{d\downarrow} - c^\dagger_{1\downarrow}c^\dagger_{d\uparrow})|0\rangle/\sqrt{2}$, and $c^\dagger_{d\uparrow}c^\dagger_{d\downarrow}|0\rangle$, with energies $E_{1,2,3}$ corresponding to the solutions of the equation:

$$\begin{pmatrix} E-2\epsilon_F & -\sqrt{2}V & 0 \\ -\sqrt{2}V & E-\epsilon_d-\epsilon_F & -\sqrt{2}V \\ 0 & -\sqrt{2}V & E-2\epsilon_d-U \end{pmatrix} \begin{pmatrix} c^\dagger_{1\uparrow}c^\dagger_{1\downarrow} \\ \frac{c^\dagger_{1\uparrow}c^\dagger_{d\downarrow}-c^\dagger_{1\downarrow}c^\dagger_{d\uparrow}}{\sqrt{2}} \\ c^\dagger_{d\uparrow}c^\dagger_{d\downarrow} \end{pmatrix} = 0. \tag{6.48}$$

This 3×3–matrix can still be diagonalised analytically, but the exact expressions are quite lengthy. Using the abbreviations:

$$X = U + 3(\epsilon_d - \epsilon_F) \tag{6.49}$$

$$Y = XU + 3(4V^2 + (\epsilon_d - \epsilon_F)^2) \tag{6.50}$$

$$Z = \sqrt[3]{U\big(X(U+X) - 18V^2\big) + \sqrt{U^2\big(X(U+X) - 18V^2\big)^2 - 4Y^3}}, \tag{6.51}$$

the eigenenergies are given by:

$$E_1 = \frac{1}{3}(U + 3\epsilon_d + 3\epsilon_F) + \frac{Z}{3\sqrt[3]{2}} + \frac{\sqrt[3]{2}Y}{3Z} \tag{6.52}$$

$$E_2 = \frac{1}{3}(U + 3\epsilon_d + 3\epsilon_F) - \frac{1 - i\sqrt{3}}{6\sqrt[3]{2}}Z - \frac{1 + i\sqrt{3}}{3\sqrt[3]{4}Z}Y \tag{6.53}$$

$$E_3 = \frac{1}{3}(U + 3\epsilon_d + 3\epsilon_F) - \frac{1 + i\sqrt{3}}{6\sqrt[3]{2}}Z - \frac{1 - i\sqrt{3}}{3\sqrt[3]{4}Z}Y. \tag{6.54}$$

In the interesting case where the Coulomb repulsion gets very strong, $U \to \infty$, these energies are

$$E_1 \to \infty \tag{6.55}$$

$$E_2 = \frac{\epsilon_d + 3\epsilon_F - \sqrt{(\epsilon_d - \epsilon_F)^2 + 8V^2}}{2} \tag{6.56}$$

$$E_3 = \frac{\epsilon_d + 3\epsilon_F + \sqrt{(\epsilon_d - \epsilon_F)^2 + 8V^2}}{2}. \tag{6.57}$$

The normalised states are given by the following linear combinations:

$$\mathsf{e}^\dagger_{1,2,3}|0\rangle = F_{1,2,3}c^\dagger_{1\uparrow}c^\dagger_{1\downarrow}|0\rangle + G_{1,2,3}\frac{c^\dagger_{1\uparrow}c^\dagger_{d\downarrow} - c^\dagger_{1\downarrow}c^\dagger_{d\uparrow}}{\sqrt{2}}|0\rangle + H_{1,2,3}c^\dagger_{d\uparrow}c^\dagger_{d\downarrow}|0\rangle. \tag{6.58}$$

Since the first two lines of equation (6.48) must be linear independent if $V \neq 0$ (if $V = 0$ this Hamiltonian can be easily solved see [28]), the coefficients are given by:

$$F = \frac{\sqrt{2}V}{E - 2\epsilon_F}/L \tag{6.59}$$

$$G = 1/L \tag{6.60}$$

$$H = \left(\frac{E - \epsilon_d - \epsilon_F}{\sqrt{2}V} - \frac{\sqrt{2}V}{E - \epsilon_F}\right)/L. \tag{6.61}$$

The indices $1, 2, 3$ for F, G, H, E and L have been dropped in the above equations. The normalisation constant L is given by

$$L^2 = \left(\frac{\sqrt{2}V}{E - 2\epsilon_F}\right)^2 + 1 + \left(\frac{E - \epsilon_d - \epsilon_F}{\sqrt{2}V} - \frac{\sqrt{2}V}{E - \epsilon_F}\right)^2. \tag{6.62}$$

The antisymmetrised basis for three particle states of this problem is given by the following four operators:

$$c^\dagger_{1\uparrow}c^\dagger_{1\downarrow}c^\dagger_{d\uparrow}, \quad c^\dagger_{d\uparrow}c^\dagger_{d\downarrow}c^\dagger_{1\uparrow}, \quad c^\dagger_{1\uparrow}c^\dagger_{1\downarrow}c^\dagger_{d\downarrow}, \quad c^\dagger_{d\uparrow}c^\dagger_{d\downarrow}c^\dagger_{1\downarrow}. \tag{6.63}$$

These four states are obviously eigenstates of S^2 and S_z with the eigenvalues:

state	S^2	S_z
$c^\dagger_{1\uparrow}c^\dagger_{1\downarrow}c^\dagger_{d\uparrow}$	$1/2$	$+1/2$
$c^\dagger_{d\uparrow}c^\dagger_{d\downarrow}c^\dagger_{1\uparrow}$	$1/2$	$+1/2$
$c^\dagger_{1\uparrow}c^\dagger_{1\downarrow}c^\dagger_{d\downarrow}$	$1/2$	$-1/2$
$c^\dagger_{d\uparrow}c^\dagger_{d\downarrow}c^\dagger_{1\downarrow}$	$1/2$	$-1/2$

Therefore, the operators S^2 and S_z are given by:

$$S^2 = \hbar^2\frac{3}{4}\big(c^\dagger_{1\uparrow}c^\dagger_{1\downarrow}c^\dagger_{d\uparrow} + c^\dagger_{d\uparrow}c^\dagger_{d\downarrow}c^\dagger_{1\uparrow} + c^\dagger_{1\uparrow}c^\dagger_{1\downarrow}c^\dagger_{d\downarrow} + c^\dagger_{d\uparrow}c^\dagger_{d\downarrow}c^\dagger_{1\downarrow}\big) \tag{6.64}$$

and

$$S_z = \hbar\frac{1}{2}\big(c^\dagger_{1\uparrow}c^\dagger_{1\downarrow}c^\dagger_{d\uparrow} + c^\dagger_{d\uparrow}c^\dagger_{d\downarrow}c^\dagger_{1\uparrow} - c^\dagger_{1\uparrow}c^\dagger_{1\downarrow}c^\dagger_{d\downarrow} - c^\dagger_{d\uparrow}c^\dagger_{d\downarrow}c^\dagger_{1\downarrow}\big). \tag{6.65}$$

Again, simple calculation shows that

$$[H, S^2] = 0 \qquad \text{and} \qquad [H, S_z] = 0. \tag{6.66}$$

A basis in the spin–up space is given by the following linear combination:

$$\mathtt{f}^\dagger_{\pm\uparrow}|0\rangle \stackrel{\text{def}}{=} I_\pm c^\dagger_{1\uparrow}c^\dagger_{1\downarrow}c^\dagger_{d\uparrow}|0\rangle + J_\pm c^\dagger_{d\uparrow}c^\dagger_{d\downarrow}c^\dagger_{1\uparrow}|0\rangle. \tag{6.67}$$

Thus the Hamiltonian can be recast into the following matrix equation:

$$\begin{pmatrix} \epsilon_d + 2\epsilon_F & -V \\ -V & 2\epsilon_d + \epsilon_F + U \end{pmatrix}\begin{pmatrix} I_\pm \\ J_\pm \end{pmatrix} = E\cdot\begin{pmatrix} I_\pm \\ J_\pm \end{pmatrix}. \tag{6.68}$$

The three particle case thus turns out to be very similar to the one particle case. Therefore, the eigenenergies are easily derived from the one–particle eigenenergies:

$$E_\pm = \frac{3\epsilon_F + 3\epsilon_d + U \pm \sqrt{(\epsilon_d - \epsilon_F + U)^2 + 4V^2}}{2}. \tag{6.69}$$

Finally, the only possible four–particle state is given by:

$$\mathtt{g}^\dagger \stackrel{\text{def}}{=} c^\dagger_{1\uparrow}c^\dagger_{1\downarrow}c^\dagger_{d\uparrow}c^\dagger_{d\downarrow}. \tag{6.70}$$

The energy of this normalised state is easily calculated:

$$2\epsilon_d + 2\epsilon_F + U \tag{6.71}$$

To summarise, the number of states for a given particle number is shown in the following table:

particles	states
0	1
1	4
2	6
3	4
4	1

After the complete solution of the Hamiltonian, the possible resonances in the total cross section of this system can be studied. So far, the Hamiltonian (6.26) has been completely diagonalised. It is important to note that the eigenstates and the eigenenergies in the spectral density (6.73) belong to the Hamiltonian:

$$\hat{\mathcal{H}} = \hat{H} - \mu\hat{N} = \sum_{\sigma}(\epsilon_F - \mu)n_{1\sigma} - \sum_{\sigma}(\epsilon_d - \mu)n_{d\sigma} + V\sum_{\sigma}\left(c^{\dagger}_{1\sigma}c_{d\sigma} + c^{\dagger}_{d\sigma}c_{1\sigma}\right) + Un_{d\uparrow}n_{d\downarrow}. \tag{6.72}$$

Technically, each appearance of ϵ_F must be replaced by $\epsilon_F - \mu$ and ϵ_d by $\epsilon_d - \mu$. This replacement will in fact leave the eigenstates unchanged and only shifts the eigenenergies. The eigenenergy E of an N–particle state is shifted to $E - \mu N$. This transformation rule is general and not only true for this special model, as it can be easily proved. With this relationship it is easy to evaluate the eigenenergies of $\hat{\mathcal{H}}$ from the eigenenergies of $\hat{H}$ and vice versa. This transformation has been employed in the pictures 6.2 and 6.3, where the energy scale of the original Hamiltonian $\hat{H}$ is used.

The spectral density $S_{AB}(E)$ of two operators A and B is given by:

$$S_{AB}(E) = \frac{\hbar}{\Xi}\sum_{n,m}\langle E_n|B|E_m\rangle\langle E_m|A|E_n\rangle \cdot \cdot e^{-\beta E_n}(e^{\beta E} + 1)\delta\big(E - (E_n - E_m)\big), \tag{6.73}$$

where the sum runs over all eigenstates of the system. The grand canonical partition function Ξ is given by:

$$\Xi = \mathrm{Tr}\big(e^{-\beta\hat{\mathcal{H}}}\big). \tag{6.74}$$

The spectral density $S_{d\sigma d\sigma}(E)$ of $G_{d\sigma d\sigma}(E) \stackrel{\mathrm{def}}{=} \langle\langle c_{d\sigma} : c^{\dagger}_{d\sigma}\rangle\rangle$ can be simplified to:

$$S_{d\sigma d\sigma}(E) = \frac{\hbar}{\Xi}\sum_{n,m}|\langle E_m|c_{d\sigma}|E_n\rangle|^2 \cdot \cdot \left(e^{-\beta E_m} + e^{-\beta E_n}\right)\delta\big(E - (E_n - E_m)\big). \tag{6.75}$$

The only transitions that are non–vanishing are:

$$\langle 0|c_{d\downarrow}\mathtt{a}^{\dagger}_{\pm\downarrow}|0\rangle = A_{\pm} \tag{6.76}$$

$$\langle 0|\mathtt{a}_{\pm\uparrow}c_{d\downarrow}\mathtt{c}^{\dagger}|0\rangle = -\frac{B_{\pm}}{\sqrt{2}} \tag{6.77}$$

$$\langle 0|\mathtt{a}_{\pm\downarrow}c_{d\downarrow}\mathtt{d}^{\dagger}|0\rangle = -B_{\pm} \tag{6.78}$$

$$\langle 0|\mathtt{a}_{\pm\uparrow}c_{d\downarrow}\mathtt{e}^{\dagger}_{1,2,3}|0\rangle = -\frac{B_{\pm}G_{1,2,3}}{\sqrt{2}} - A_{\pm}H_{1,2,3} \tag{6.79}$$

$$\langle 0|\mathtt{b}c_{d\downarrow}\mathtt{f}^{\dagger}_{\pm\uparrow}|0\rangle = J_{\pm} \tag{6.80}$$

$$\langle 0|\mathtt{c}c_{d\downarrow}\mathtt{f}^{\dagger}_{\pm\downarrow}|0\rangle = \frac{J_{\pm}}{\sqrt{2}} \tag{6.81}$$

$$\langle 0|\mathtt{e}_{1,2,3}c_{d\downarrow}\mathtt{f}^{\dagger}_{\pm\downarrow}|0\rangle = F_{1,2,3}I_{\pm} - \frac{J_{\pm}G_{1,2,3}}{\sqrt{2}} \tag{6.82}$$

$$\langle 0|\mathtt{f}_{\pm\uparrow}c_{d\downarrow}\mathtt{g}^{\dagger}|0\rangle = -I_{\pm}. \tag{6.83}$$

Here only the resonances at $T = 0$ are considered. For this case the $T \to 0$ behaviour of the following expression must be studied:

$$\frac{C}{\Xi}e^{-\beta E_n} = \frac{C}{\sum_i e^{-\beta(E_i - E_n)}}. \tag{6.84}$$

Let $E_{\mathrm{gnd}} = \min_i(E_i)$. Here it is assumed that the ground state with energy E_{gnd} is non–degenerate. Otherwise, the sum over all ground states must be included in the spectral density (6.86). It is easily seen that the expression (6.84) is non–vanishing in the $\beta \to \infty$ limit if and only if $E_n = E_{\mathrm{gnd}}$. Thus

$$\lim_{\beta\to\infty}\frac{C}{\Xi}e^{-\beta E_n} = \begin{cases} 0 & \text{if } E_n \neq E_{\mathrm{gnd}} \\ C & \text{if } E_n = E_{\mathrm{gnd}}. \end{cases} \tag{6.85}$$

Finally, the spectral density at $T = 0$ is given by:

$$\begin{aligned} S_{d\sigma d\sigma}(E) = \hbar\Bigg(&\sum_m |\langle E_m|c_{d\sigma}|E_{\mathrm{gnd}}\rangle|^2\delta\big(E - (E_{\mathrm{gnd}} - E_m)\big) + \\ &\sum_n |\langle E_{\mathrm{gnd}}|c_{d\sigma}|E_n\rangle|^2\delta\big(E - (E_n - E_{\mathrm{gnd}})\big)\Bigg). \end{aligned} \tag{6.86}$$

In order to illustrate the resulting spectral densities, the following special case is considered: Let the Coulomb repulsion be infinitely strong, that is, $U \to \infty$. Furthermore, the temperature dependent chemical potential μ should be $\mu(T = 0) = \epsilon_F$. Since the energy ϵ_F is interpreted as the "Fermi

energy" of the model, this choice is natural. Finally, let $V \neq 0$ in order to avoid a completely degenerate system. In this case, a simple calculation shows that the energy E_2 given by expression (6.57) must be the ground state energy. Furthermore, the following eigenstates ($\mathtt{e}_1^\dagger$, $\mathtt{f}_{+\uparrow}^\dagger$, $\mathtt{f}_{+\downarrow}^\dagger$ and $\mathtt{g}^\dagger$) do not exist in that limit. Their corresponding eigenenergies are diverging. In picture 6.2, the resulting resonances for a typical choice of parameters are shown.

It is the singlet ground state $\mathtt{e}_2^\dagger|0\rangle$ given by equation 6.58 that is responsible for the appearance of resonances close to the Fermi energy. Thus as long as the parameters μ, ϵ_d, ϵ_F, V and U are such that $\mathtt{e}_2^\dagger|0\rangle$ is the ground state, the system will show a resonance close to $E - \mu = 0$. In the picture 6.3, the infinite Coulomb repulsion approximation has been dropped. This has direct consequences for the spectrum, since a peak appears at $E \approx U$. The Kondo resonance appears since for the choice of parameters the ground state is still $\mathtt{e}_2^\dagger|0\rangle$, as it can be easily verified.

The fundamental quantities have been determined to study the finite temperature behaviour of this model. Since the main intension of this model was to illustrate the appearance of a resonance close to the Fermi level, the finite temperature behaviour of this system will not be discussed. Although the zero band width Anderson Hamiltonian is a drastic simplification, this approximation is useful even for the solution of the complete Anderson model. In the renormalisation group calculations, first introduced by Wilson, further sites are added to the chain to build up the band of conduction states.

It is interesting to note that the occupation of the d–level can easily be determined from the so–called spectral theorem:

$$\langle B(t')A(t)\rangle = \frac{1}{\hbar}\int_{-\infty}^{\infty} \frac{S_{AB}(E)}{e^{\beta E}+1}\exp\Big(-\frac{i}{\hbar}E(t-t')\Big)dE. \tag{6.87}$$

(This expression is only valid for anticommuting operators A and B.) From this relationship and the limit (6.85), it is seen at once that

$$\langle n_{d\sigma}\rangle = \frac{1}{\hbar}\int_{-\infty}^{\infty} \frac{S_{d\sigma d\sigma}(E)}{e^{\beta E}+1}dE = \sum_m |\langle E_m|c_{d\sigma}|E_{\rm gnd}\rangle|^2 \tag{6.88}$$

for $T = 0$. On the other hand, the occupation of the d–level can be directly calculated from the ground state by:

$$\begin{aligned}\langle n_{d\sigma}\rangle = \langle E_{\rm gnd}|c_{d\sigma}^\dagger c_{d\sigma}|E_{\rm gnd}\rangle = &\sum_m \langle E_{\rm gnd}|c_{d\sigma}^\dagger|E_m\rangle\langle E_m|c_{d\sigma}|E_{\rm gnd}\rangle = \\ &\sum_m |\langle E_m|c_{d\sigma}|E_{\rm gnd}\rangle|^2.\end{aligned} \tag{6.89}$$

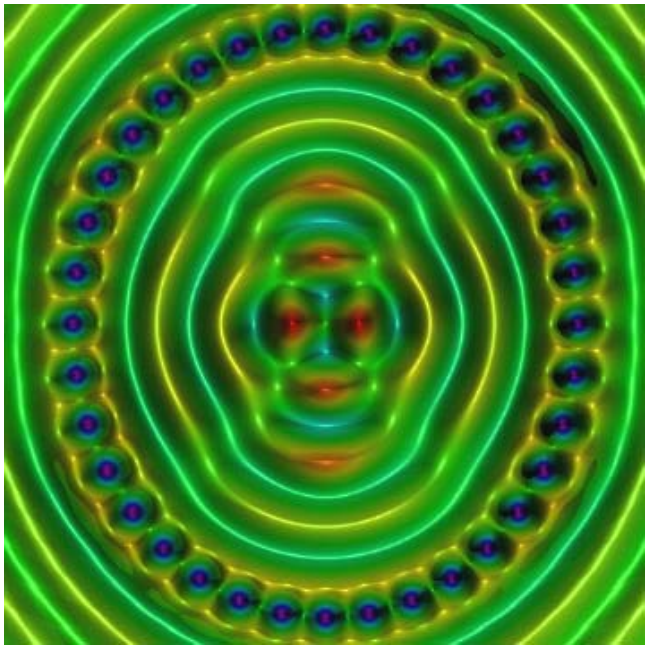

Figure 6.4: This is an ellipse of 36 adatoms. The ellipse has the major–half axis with the lengths 60Å and 70Å. The conductivity is measured while electrons with the energy -0.1965eV are emitted from the tip that is 4Å away from the adatoms and 8Å away from the partially reflecting surface. All the parameters are almost identical with the parameters used for the quantum corral. But the partially reflecting surface is much stronger now ($\alpha = 600$ÅeV). The slope of the barrier is again $F = 1$eV/Å. The energy has been chosen so that two minima are clearly visible in the two foci of the ellipse.

This relationship leads to some interesting identities, such as:

$$\left(\frac{B_+G_{1,2,3}}{\sqrt{2}} + A_+H_{1,2,3}\right)^2 + \left(\frac{B_-G_{1,2,3}}{\sqrt{2}} + A_-H_{1,2,3}\right)^2 = \frac{G_{1,2,3}^2}{2} + H_{1,2,3}^2. \quad (6.90)$$

6.3 The Kondo mirage

The Kondo mirage is a variation of the original quantum corral. For this experiment, 36 adatoms are placed on a Cu(111) surface. They are arranged to form an ellipse with the following geometry: The great major–half axis is 70Å and the small is 60Å. Thus again, the corral is several magnitudes larger than

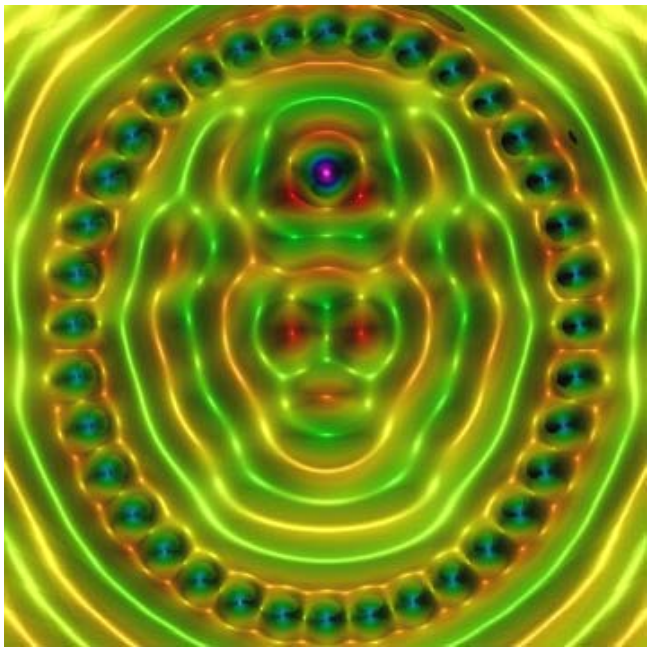

Figure 6.5: This image shows the same ellipse as in figure 6.4 with a Kondo adatom in the upper focus of the ellipse. In this case, the energy of the electron coincides with the maximum in the Kondo resonance. But since the energy of the emitted electron is fixed, the Kondo adatom in this case behaves like an adatom with energy independent scattering cross section. The Lorentzian energy dependence of the magnetic adatom is given by equation (6.91).

the maximum possible resolution of an STM. This elliptical wall can be built with magnetic as well as non–magnetic adatoms (adsorbates). In the original experiment [26], the same result was found when the wall Co adatoms were replaced by non–magnetic CO molecules. The foci of this ellipse are ± 36.06Å away from the centre. In one of the foci, a magnetic adatom (Co) is placed that shows a Kondo resonance for temperatures up to 4K on Cu(111). The STM can be used to perform three different measurements on this setup. At first, the usual corrugation (or current) picture can be done for a fixed bias voltage V. The following short hand notation may be useful: V — $(\mathbf{r}, I)$. Second, the conductivity σ can be measured for a fixed bias voltage V (V — $(\mathbf{r}, \sigma)$). And finally, the bias voltage V versus conductivity σ characteristics can be determined ($\mathbf{r}$ — (V, σ)) for a fixed point in the corral. Let V_{res} be the bias voltage at the resonance, that is where σ is extremal. It should be mentioned that since the total cross section of the magnetic adatom is ex-

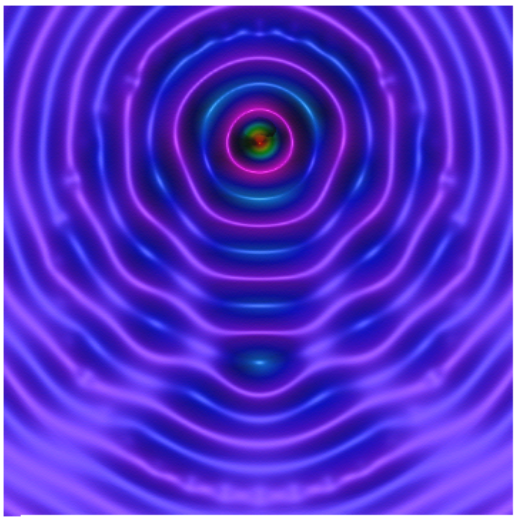

Figure 6.6: This is the difference between figure 6.4 and figure 6.5, which have been taken with the same electron energy. From the simple superposition model it is expected that this difference should look like picture 3.5. In a very crude approximation, this difference picture has some similarities with a single adatom STM image. But there are some obvious deviations, especially the maximum in the empty focus. As already mentioned above, the superposition model takes into account only the diagonal T–matrix elements, and thus it cannot predict this maximum. Hence, this maximum is directly related to the size of the off–diagonal T–matrix elements.

tremely energy dependent near the Kondo resonance (the region of interest), the approximation (2.17) must fail. Thus corrugation and current pictures must be calculated by the integral (2.16). The two measurements that show the Kondo mirage are the following:

1. An (V, σ) measurement is done in both foci. In the focus where the magnetic adatom is placed, the typical Kondo resonance is found. But the empty focus also shows a Kondo resonance. This mirage resonance is attenuated by approximately a factor of 10. At another point which is much closer (10Å) to the magnetic atom than the other focus (that is 72.12Å away), no resonance is found in the (V, σ) measurement. The (V, σ) measurements have the advantage that they can determine the

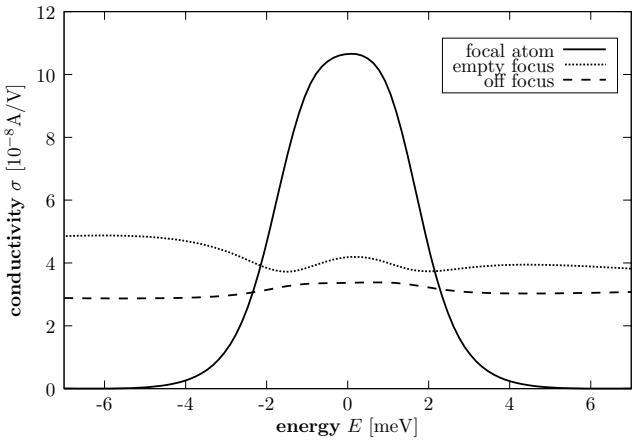

Figure 6.7: The lineshapes for different points inside the ellipse. The focal Kondo atom shows the typical Kondo resonance at 0eV. The Kondo resonance is also present in the empty focus, although it is damped by almost a factor of 10. The dashed line shows the lineshape for a point close to the centre of the ellipse. At this point, the Kondo resonance cannot be distinguished from the background, despite the fact that this point is closer to the Kondo adatom than the empty focus.

detailed lineshape. On the other hand, this lineshape can be measured only at some special points of the corral.

2. A measurement that shows the spatial distribution of the Kondo mirage can be done by an $(\mathbf{r}, \sigma)$ measurement. Here the bias voltage is chosen very close to V_{res}. At first, an $(\mathbf{r}, \sigma)$ picture is taken from the empty ellipse of 36 non–magnetic adatoms with no magnetic adatom inside the corral. Then the magnetic adatom is placed in one of the foci. The second $(\mathbf{r}, \sigma)$ picture is taken from this constellation. And finally, these two pictures are subtracted from each other. By this method, the effect of the additional magnetic adatom is spatially resolved. Of course, the 'difference picture' has a peak at the focus that was filled with the magnetic adatom. Although nothing changed in the vicinity of the empty focus, the difference picture shows a spike in the empty focus.

Only ellipses with a very special geometry — those which have large surface state amplitudes at the two foci — will give a good mirage effect. In other words, the $(\mathbf{r}, I)$ image of the empty ellipse must have maxima at the two foci. The physics of the empty ellipse can be controlled by the very same

approximations that were introduced for the circular quantum corral. Thus it is clear that the appearance of a maximum in the two foci not only depends on the geometry of the ellipse but also on the bias voltage.

All the presented features of a Kondo mirage can be reproduced in this theory of an STM. This is no surprise since the theory of Heller [20], which is capable of simulating quantum mirages, was already shown to be a special case of the theory presented here. At first, the ellipse must be prepared to show a maximum in the $(\mathbf{r}, I)$ or corrugation scan. The resulting ellipse is shown in figure 6.4. Since the geometry of the ellipse was fixed by the experimental setup, the energy of the emitted electrons was tuned until a maximum appeared in the foci. It was necessary to increase the repulsiveness α of the partially reflecting wall. Otherwise, the maxima in the foci could not be constructed. Since the theory presented in [20] reproduced the experimental results with $\alpha = \infty$, this tuning of the partially reflecting surface could be expected.

Next, the magnetic adatom must be constructed. For this purpose, the relationship (6.25) is utilised. The now energy dependent total cross section $\sigma_{\mathrm{tot}}(E)$ is given a resonance behaviour that mimics the Kondo resonance. That such a "magnetic adatom" does in fact show the desired resonance behaviour can be seen in figure 6.7. For sake of completeness, here are the precise parameters that have been used to model the Kondo adatom:

$$u(E) = 80.7754 - \frac{(373.134 + 80.7754)0.001 \cdot 0.001}{(E + 0.1835)(E + 0.1835) + (0.001 \cdot 0.001)}. \qquad (6.91)$$

Finally, this "magnetic atom" is introduced into one of the foci of the prepared ellipse. The $(\mathbf{r}, \sigma)$ scan of this configuration is shown in picture 6.5. It may be a surprise that no maximum is seen in the empty focus, although the name "quantum mirage" may suggest it otherwise. But the theoretical prediction is in complete agreement with the experimental results (see for instance [22]). The "mirage" is only seen when the empty ellipse is subtracted from this picture. In the difference picture 6.6 the mirage effect in the empty focus can be clearly seen. If the superposition approximation would be exact, the difference image would be identical to the image of a single Kondo adatom. The fact that this is not the case — especially that there is a mirage effect seen in the other focus — is thus directly related to the off–diagonal elements of the T–matrix.

At last, the (V, σ) lineshape at selected points of the quantum corral can be studied as shown in figure 6.7. At the magnetic adatom position itself the Kondo resonance is clearly seen. The empty focus shows the same resonance behaviour although the peak is lowered by a factor of 10. The third point is

close to the centre of the ellipse and thus only half as far away as the empty focus. Nonetheless, no Kondo resonance signal is detected at this point.

That the quantum mirage can be correctly described by a scattering theory has already been pointed out by Heller [26]. In comparison with Heller's theory, the merit of the calculation of "quantum mirages" from source theory is that here a fully three–dimensional approach has been taken. This approach does in fact lead to some insights which are not accessible from a purely two–dimensional solution. Nonetheless, both theories have some difficulties in describing the magnetic adatom. So in both cases the scattering properties of this Kondo impurity had to be introduced ad hoc.

Chapter 7

Conclusion

This thesis presented a three–dimensional model of an STM which could simulate a multitude of experimental images. Among others, the corrugation pictures of quantum corrals and quantum mirages could be calculated with this theory. Due to its relative simplicity, the theory allowed the prediction of the experimental STM images without any approximations. The calculations presented were not only treated on a proof of concept basis, but were completely implemented. That is, all simulated STM pictures presented in this thesis were calculated by a standard C++ program which was developed in the course of the work by the author. The algorithms that were developed specifically for this program were described in detail, and their mathematical derivation was also included.

Except for calculations from first principles, previous simulations of an STM are mainly based either on the theory of Tersoff–Hamann [60] or the theory of Heller [22, 20]. While Tersoff–Hamann's model is primarily used for the simulation of simple metallic surfaces, Heller's outright two–dimensional approach is employed to calculate quantum corrals. The theory presented in this thesis is more comprehensive than either of these two previous approaches because it can simulate, for the first time, both simple metallic surfaces *and* quantum corrals. That this theory can reproduce the results of the Tersoff–Hamann theory was already shown by [6]. It can, however, also reproduce the results of Heller's theory of quantum corrals, as it was shown in section 4.3 of this thesis.

Beside the models of Tersoff–Hamann and Heller, in recent years calculations from first principles are also employed in STM simulations. This development was made possible by the increase in available computer power. First principle calculations are primarily used to generate STM images of simple metallic surfaces. However, first principle calculations are multi–particle approaches and hence are not directly comparable with either of the models

mentioned above, which are single–particle theories. Although theoretically, first principle calculations are the royal road to the understanding of physical problems, there are limitations to the approach in this case. Due to the numerical complexity of the problems and the restrictions of the underlying libraries, quite a few approximations must be made. For instance, periodic boundary conditions are usually imposed on the problem. Thus, instead of a single tip, the calculations take into account an infinite array of tips.

Although the first principle calculations for the STM yield fairly accurate and quantitatively precise results for simple metallic surfaces, at present they can hardly cope with more complicated problems such as quantum corrals or quantum mirages. Despite the fact that the theory presented here makes use of cruder approximations, it can deal with problems of great complexity, such as unusual quantum corrals and quantum mirages. In fact, STM images of arbitrary adatom arrangements can be easily calculated. Last but not least, it delivers results rapidly: while a typical first principles calculation takes several hours, the simulation of a corrugation picture in the model presented here takes about 3 minutes on an already relatively slow personal computer.

While most approaches set out to model a *whole* quantum corral, to my knowledge there are no publications that deal with the oscillations of electronic density of a *single* adatom. Therefore, the present thesis started out by examining and explaining the standing wave patterns of single adatoms. From the theoretical point of view, the single adatom case is easier to handle due to a reduced computation time and a further simplification of the theory. One striking result of this approach was the insight that the single adatom problem displays almost *all* physical properties of the arbitrary adatom arrangements. What is more, it could be shown that the naive superposition of single adatom images gives qualitatively acceptable results in most cases. Thus, the naive superposition of single adatom images, an idea that has not been tried out before, turned out to be a useful aid to give zero order approximations of STM pictures. Within the framework of the theory presented here, the terms that were neglected in the naive superposition approximation can be identified. Thus it is possible to foresee when the naive superposition approximation must break down. This possibility is the direct consequence of the rigorous derivations that result in a clear solution of the model.

One of the greatest merits of the (unapproximated) model developed here is to link the ad hoc parameters of the two–dimensional theory of quantum corrals introduced by Heller to physical quantities. Thus, the theory presented here succeeds in giving a physical interpretation of the observed wavelength of the electrons in the surface states. Furthermore, the scattering phase shifts can be linked to the T–matrix elements that are directly given by the potential distribution in the model.

Experimental observations showed that tungsten tips yield images with higher resolution than other tips; therefore, usually tungsten tips are used in the STM apparatus. Theoretically, the increased resolution of tungsten tips has been attributed to the fact that the emitted electrons originate from d orbitals [8, 9, 54]. It is a further feature of the model that tips with definite multipole characteristics can be easily introduced. Since this feature can only be integrated into a three–dimensional model, the theory developed here allows a more realistic simulation of the experiment than it is the case in Heller's two–dimensional model.

The thesis also addressed the simulation of the Kondo mirage. With a relatively simple extension, the model was also capable of reproducing STM images of the Kondo ellipse. The calculation of the spectral density of the zero band width Anderson model paved the way for this extension. The typical Kondo lineshape could be observed in the empty focus of the ellipse. In addition, the topographic STM image of the whole ellipse showed the mirage peak in the empty focus. That this model is capable of reproducing the Kondo mirage is a consequence of its close relationship to Heller's theory, which could also be extended to cover this phenomenon [20].

Potential applications of this model beyond the areas covered in solid state physics include the recent experimental realisations of optical corrals [17, 16]. Present theories of these optical corrals employ the same methods as for the quantum corrals. Thus it may be possible to predict these optical corrals with the theory presented in this thesis. It is also claimed that acoustical corrals could be constructed [20]. Should this be the case, the application of the presented ideas could be considered also in this domain.

Lastly, a few remarks must be made on the energy Green's function, on which the theory put forward in this thesis heavily relies. It is surprising that there are hardly any proven mathematical properties of the three–dimensional Green's functions. Although some fundamental properties were derived in [6], it has not been shown anywhere whether the three–dimensional Green's function is symmetric or not in the spatial variables. In the present thesis, this problem could be circumvented since only three–dimensional Green's functions of a special structure were dealt with. For this case, it could be easily demonstrated that the Green's function is symmetric in its spatial arguments.

Another example of how untouched this area of mathematical physics is, is the lack of closed–form expressions for the three–dimensional Green's function for a step barrier. The step barrier is one of the most often used potential distributions in quantum mechanics to study the principal behaviour of a physical system. Nonetheless, the three–dimensional version of the energy Green's function of the step barrier has never been studied in detail. No

fast convergent series expansion or expression in terms of other special functions (if possible) can be found for this three–dimensional Green's function. Clearly, this untouched area of physics and mathematical physics is still full of potential discoveries.

Chapter 8

Appendix

8.1 Legend

δ_{lm}	multipole delta function defined by equation (2.46)
ϵ_F	Fermi energy
G,G_{ret}	three–dimensional retarded Green's function
G_1,$G_{1\mathrm{ret}}$	one–dimensional retarded Green's function
G_{lm}	three–dimensional retarded multipole Green's function (equation (2.56))
h_l^+, h_l^-	Hankel functions given by $h_l^+ = h_l^{(1)}$ $h_l^- = h_l^{(2)}$; cf. [1] [10.1.16, 10.1.17]
$J(E)$	total current generated by the electrons with energy E
$J_m(\cdot)$	Bessel function of the first kind [1] [9.1.10]
J_{tot}	total current
$K_0(\cdot)$	modified Bessel function [1] [9.6.13]
λ_{lm}	source strength in this model given by equation (2.69)
M	electron mass $9.1 \cdot 10^{-31}$kg
σ	conductivity defined by equation (2.13)
ς	source term defined by equation (2.4)
σ_{tot}	total cross section
$T(E)$	T–matrix given by equation (2.102)
$U(\cdot)$	potential
$U_1(z)$, $U_2(\mathbf{r})$	the full potential $U(\mathbf{r})$ is split into these two potentials; see section 2.5
u_i	strength of the zero–range potentials; see definition (2.89)
V	bias voltage of the STM
$\mathcal{Y}_{lm}(\hat{\mathbf{r}})$	spherical harmonics; see [55] page 451

8.2 A different derivation of the bouncing ball Green's function

The differential equation to be solved for the quantum mechanical ballistic motion is

$$\Big(E + \frac{\hbar^2}{2M}\partial_z^2 + F \cdot z)\Big)\phi(z, E) = 0. \tag{8.1}$$

The solution of this differential equation is given by

$$\phi(z, E) = c_1 \cdot \mathrm{Ai}\big(-2\beta(Fz + E)\big) + c_2 \cdot \mathrm{Bi}\big(-2\beta(Fz + E)\big), \tag{8.2}$$

where $\beta = (M/4\hbar^2F^2)^{\frac{1}{3}}$. For the bouncing ball problem the particle faces an impenetrable wall in the region $[0, \infty[$. Thus the potential for the bouncing ball problem is given by:

$$U(z) = -F \cdot z + \begin{cases} 0 & \text{for } z < 0 \\ \infty & \text{for } z \geq 0 \end{cases}. \tag{8.3}$$

Let $\phi_-(z, E)$ be the solution of the bouncing ball problem with the correct boundary behaviour for $z \to -\infty$. Since the solution must be bounded for $z \to -\infty$,

$$\phi_-(z, E) = A \cdot \mathrm{Ai}\big(-2\beta(Fz + E)\big). \tag{8.4}$$

On the other hand, let $\phi_+(z, E)$ be the solution of the bouncing ball problem with the correct boundary behaviour for $z \to \infty$. Since the solution vanishes for $z \in [0, \infty[$, the boundary condition is $\phi_+(0, E) = 0$. Thus

$$\begin{aligned} \phi_+(z, E) = \quad & B \cdot \Big(\mathrm{Ai}\big(-2\beta(Fz + E)\big) \cdot \mathrm{Bi}\big(-2\beta E\big) - \\ & \mathrm{Bi}\big(-2\beta(Fz + E)\big) \cdot \mathrm{Ai}\big(-2\beta E\big)\Big). \end{aligned} \tag{8.5}$$

The Wronskian $\mathcal{W}(\phi_-, \phi_+) = \phi_-(0, E) \cdot \phi'_+(0, E) - \phi'_-(0, E) \cdot \phi_+(0, E)$ is given by

$$\mathcal{W}(\phi_-, \phi_+) = \frac{2F\beta AB}{\pi}\,\mathrm{Ai}\big(-2\beta E\big). \tag{8.6}$$

It should be mentioned that the Wronskian condition of the Airy differential equation is used in this derivation:

$$\mathrm{Ai}(x)\,\mathrm{Bi}'(x) - \mathrm{Ai}'(x)\,\mathrm{Bi}(x) = \frac{1}{\pi}. \tag{8.7}$$

With these results the Green's function is given by:

$$G(z,z',E) = \frac{2M}{\hbar^2}\frac{\phi_-(z_<,E)\phi_+(z_>,E)}{\mathcal{W}(\phi_-,\phi_+)} = -4\pi F\beta^2\,\mathrm{Ai}\big(-2\beta(Fz_< + E)\big)\cdot \\ \frac{\mathrm{Ai}\big(-2\beta(Fz_> + E)\big)\cdot \mathrm{Bi}\big(-2\beta E\big) - \mathrm{Bi}\big(-2\beta(Fz_> + E)\big)\cdot \mathrm{Ai}\big(-2\beta E\big)}{\mathrm{Ai}\big(-2\beta E\big)}. \quad (8.8)$$

This solution is identical to the solution (3.10) for $\alpha \to \infty$.

8.3 Scattering phase shifts of the regularised delta potential

Here all scattering phase shifts of the regularised delta potential are determined. It will be shown that the only basic limitation of these potentials is that they can only generate s–wave scattering. Any scattering wavefunction of a radial symmetric potential can be expressed as:

$$\psi(\mathbf{r}) = \frac{1}{(2\pi)^{3/2}}\sum_{l=0}^{\infty} i^l(2l+1)\psi_l(\mathbf{r})P_l(\cos(\theta)), \quad (8.9)$$

where the $\psi_l(\mathbf{r})$ are given by:

$$\psi_l(\mathbf{r}) = e^{i\delta_l}\big(j_l(kr)\cos(\delta_l) - n_l(kr)\sin(\delta_l)\big) \quad (8.10)$$

and must satisfy the following differential equation:

$$\Big(E + \frac{\hbar^2}{2M}\Delta - u\delta(\mathbf{r})\partial_r r\Big)\psi_0(\mathbf{r})d^3r = 0. \quad (8.11)$$

When only s–scattering is taken into account, the scattering wavefunction must have the following structure:

$$\psi_0(\mathbf{r}) = \frac{\sin(kr+\delta_0)}{r}. \quad (8.12)$$

Clearly, this is usually an approximation, but in fact it will be shown at the end of this section that for the regularised delta potentials the phase shifts δ_l vanish for $l \in \mathbb{N}$ and thus δ_0 defines the full scattering properties. The phase shift δ_0 can now be determined by the following standard method:

Let B_ϵ be the ball with radius ϵ around 0. Consider the expression:

$$\lim_{\epsilon\to 0}\int_{B_\epsilon}\Big(E + \frac{\hbar^2}{2M}\Delta - u\delta(\mathbf{r})\partial_r r\Big)\psi_0(\mathbf{r})d^3r = 0. \quad (8.13)$$

The second term in equation (8.13) can be evaluated as follows:

$$\begin{aligned}\int_{B_\epsilon} \frac{\hbar^2}{2M}\Delta\Big(\frac{\sin(kr+\delta_0)}{kr}\Big)d^3r = \frac{\hbar^2}{2M}\int_{B_\epsilon} \operatorname{div}\Big(\operatorname{grad}\frac{\sin(kr+\delta_0)}{kr}\Big)d^3r = \\ \frac{\hbar^2}{2M}\int_{\partial B_\epsilon} \frac{kr\cos(kr+\delta_0)-\sin(kr+\delta_0)}{kr^2}d\mathbf{f} = \\ \frac{\hbar^2}{2Mk}\int_0^{2\pi}\int_0^{\pi}\big(k\epsilon\cos(k\epsilon+\delta_0)-\sin(k\epsilon+\delta_0)\big)\sin\theta d\theta d\phi = \\ \frac{2\pi\hbar^2}{Mk}\big(k\epsilon\cos(k\epsilon+\delta_0)-\sin(k\epsilon+\delta_0)\big).\end{aligned} \tag{8.14}$$

The first term in equation (8.13) must vanish since an ordinary function is integrated over a set of measure zero:

$$\begin{aligned}\lim_{\epsilon\to 0}\int_{B_\epsilon} E\frac{\sin(kr+\delta_0)}{r}d^3r = \lim_{\epsilon\to 0} 4\pi E\int_0^{\epsilon}\frac{\sin(kr+\delta_0)}{r}r^2dr = \\ \lim_{\epsilon\to 0} 4\pi E\Big(\frac{\sin(k\epsilon+\delta_0)}{k^2}-\frac{\epsilon\cos(k\epsilon+\delta_0)}{k}-\frac{\sin(\delta_0)}{k^2}\Big)=0.\end{aligned} \tag{8.15}$$

Finally, the third term in equation (8.13) is:

$$\lim_{\epsilon\to 0}\int_{B_\epsilon} u\delta(\mathbf{r})\partial_r\sin(kr+\delta_0)d^3r = uk\cos(\delta_0). \tag{8.16}$$

Thus from equation (8.13) the following condition can be derived:

$$-\frac{2\pi\hbar^2}{Mk}\sin(\delta_0) = uk\cos(\delta_0). \tag{8.17}$$

The total cross section can be expressed in terms of the phase shifts (see for instance [55], page 403). Since the total cross section has already been determined in equation (2.106), we can state that:

$$\begin{aligned}\frac{4\pi}{k^2+\big(\frac{2\pi\hbar^2}{Mu}\big)^2} = \sigma_{\text{tot}} = \frac{4\pi}{k^2}\sum_{l=0}^{\infty}(2l+1)\sin^2\delta_l \geq \\ \geq \frac{4\pi}{k^2}\sin^2\delta_0 = \frac{4\pi}{k^2+\big(\frac{2\pi\hbar^2}{Mu}\big)^2}.\end{aligned} \tag{8.18}$$

The important point is that equality in equation (8.18) holds only if and only if $\delta_l = 0$ for $l \in \mathbb{N}$.

8.4 The Dyson equation

$$\Big(E + \frac{\hbar^2}{2M}\nabla^2 - U(\mathbf{r})\Big)G(\mathbf{r},\mathbf{r}',E) = \delta(\mathbf{r}-\mathbf{r}') \tag{8.19}$$

$$V(\mathbf{r}) = U(\mathbf{r}) + W(\mathbf{r}) \tag{8.20}$$

$$\Big(E + \frac{\hbar^2}{2M}\nabla^2 - V(\mathbf{r})\Big)G^{\mathrm{w}}(\mathbf{r},\mathbf{r}',E) = \delta(\mathbf{r}-\mathbf{r}') \tag{8.21}$$

On the one hand, $W(\mathbf{r})$ can be seen as a perturbation of $U(\mathbf{r})$ so that the Green's function $G(\mathbf{r},\mathbf{r}',E)$ for the potential $V(\mathbf{r}) = U(\mathbf{r}) + W(\mathbf{r})$ is given by:

$$G^{\mathrm{w}}(\mathbf{r},\mathbf{r}',E) = G(\mathbf{r},\mathbf{r}',E) + \int_{\mathbb{R}^3} G(\mathbf{r},\mathbf{r}'',E)W(\mathbf{r}'')G^{\mathrm{w}}(\mathbf{r}'',\mathbf{r}',E)\,d^3r''. \tag{8.22}$$

On the other hand, $-W(\mathbf{r})$ can be seen as a perturbation of $V(\mathbf{r})$ so that the Green's function $G^{\mathrm{w}}(\mathbf{r},\mathbf{r}',E)$ for the potential $U(\mathbf{r}) = V(\mathbf{r}) - W(\mathbf{r})$ is given by:

$$G(\mathbf{r},\mathbf{r}',E) = G^{\mathrm{w}}(\mathbf{r},\mathbf{r}',E) + \int_{\mathbb{R}^3} G^{\mathrm{w}}(\mathbf{r},\mathbf{r}'',E)(-W(\mathbf{r}''))G(\mathbf{r}'',\mathbf{r}',E)\,d^3r''. \tag{8.23}$$

From the equations (8.22) and (8.23) it follows immediately that the Green's functions can be rearranged in the Dyson equation:

$$\int_{\mathbb{R}^3} G^{\mathrm{w}}(\mathbf{r},\mathbf{r}'',E)W(\mathbf{r}'')G(\mathbf{r}'',\mathbf{r}',E)\,d^3r'' = \int_{\mathbb{R}^3} G(\mathbf{r},\mathbf{r}'',E)W(\mathbf{r}'')G^{\mathrm{w}}(\mathbf{r}'',\mathbf{r}',E)\,d^3r''. \tag{8.24}$$

Bibliography

[1] Milton Abramowitz and Irene A. Stegun. *Handbook of Mathematical Functions*. Dover Publications, New York, 1972.

[2] C. Grosche F. Steiner. *Handbook of Feynman Path Integrals*. Springer–Verlag, Berlin Heidelberg New York Tokio, 1998.

[3] Philippe Blanchard and Erwin Brüning. *Distributionen und Hilbertraumoperatoren*. Springer–Verlag, Wien New York, 1993.

[4] Arno Bohm. *Quantum Mechanics Foundations and Applications*. Springer–Verlag, New York, Berlin, Heidelberg, third edition, 1979.

[5] W.E. Boyce and R.C. DiPrima. *Gewöhnliche Differentialgleichungen*. Spektrum Akademischer Verlag, Heidelberg Berlin Oxford, 1995.

[6] Christian Bracher. *Quantum Ballistic Motion and its Applications*. PhD thesis, Technische Universität München, July 1999.

[7] E. Oran Brigham. *The Fast Fourier Transform*. Prentice–Hall Inc., Englewoods Cliffs, N.J., 1974.

[8] C.J. Chen. Origin of Atomic Resolution on Metal Surfaces in Scanning Tunneling Microscopy. *Physical Review Letters*, 65(4):448–451, 1990.

[9] C.J. Chen. Tunneling matrix elements in three–dimensional space: The derivative rule and sum rule. *Physical Review B*, 42(14):8841–8857, 1990.

[10] Mustafa Riza Christian Bracher and Manfred Kleber. Propagator theory of scanning tunneling microscopy. *Physical Review B*, 56(12):7704–7715, September 1997.

[11] Yu. N. Demkov and V.N. Ostrovskii. *Zero–Range Potentials and Their Application in Atomic Physics*. Plenum, New York, 1988.

[12] Bernd Donner. 3D–Greenfunktionen im Tunnelbereich: Ein Vergleich für verschiedene Potentiale. Master's thesis, Technische Universität München, November 2000.

[13] Eleftherios N. Economou. *Green's Functions in Quantum Physics*. Springer–Verlag, Berlin Heidelberg New York Tokio, 1983.

[14] W. Elberfeld and M. Kleber. Tunneling from an ultrathin quantum well in a strong electrostatic field: A comparision of different methods. *Zeitschrift für Physik B*, 73:23–32, 1988.

[15] C.P. Lutz Eric J. Heller, M.F. Crommie and D. Eigler. Scattering and absorbtion of surface electron waves in quantum corrals. *Nature*, 369:464, June 1994.

[16] C. Chicanne et al. Imaging the Local Density of States of Optical Corrals. *Physical Rewiew Letters*, 88(9):097402–1 – 097402–4, March 2002.

[17] Gérard Colas et al. Optical Analogy to Electronic Quantum Corrals. *Physical Review Letters*, 86(21):4950–4953, May 2001.

[18] K.H. Rieder et al. STM as an operative tool: physics and chemistry with single atoms and molecules. *Europhysics News*, 34(3):1, 2003.

[19] Rosei et al. Organic Molecules Acting as Templates on Metal Surfaces. *Science*, 296:328–331, 2002.

[20] Gregory A. Fiete and Eric J. Heller. Colloquium: Theory of quantum corrals and quantum mirrages. *Review of Modern Physics*, 75:993, July 2003.

[21] Hans-Werner Fink. Point Sources for Ions and Electrons. *Physica Scripta*, 38:260–263, 1988.

[22] Jesse S. Hersch Gregory A. Fiete and Eric J. Heller. Scattering Theory of Kondo Mirages and Observation of Single Kondo Atom Phase Shift. *Physical Review Letters*, 86(11):2392–1395, March 2001.

[23] Axel Groß. *Theoretical Surface Science*. Springer–Verlag, Berlin Heidelberg, 2003.

[24] Guiseppe Grosso and Giuseppe Pastori Parravicini. *Solid State Physics*. Academic Press, San Diego, 2003.

[25] Henry K. Harbury and Wolfgang Porod. Elastic scattering theory for electronic waves in quantum corrals. *Physical Review B*, 53(23):15455–15458, June 1996.

[26] C.P. Lutz H.C. Manoharan and D.M. Eigler. Quantum mirrages formed by coherent projection of electronic structure. *Nature*, 403:512, February 2000.

[27] Eric J. Heller. Bound-State Eigenfunctions of Classically Chaotic Hamiltonian Systems: Scars of Periodic Orbits. *Physical Review Letters*, 53(16):1515, October 1984.

[28] A. C. Hewson. *The Kondo Problem to Heavy Fermions*. Cambridge university press, 1993.

[29] G. Hörmandinger. Imaging of the Cu(111) surface state in scanning tunneling microscopy. *Pysical Review B*, 49(19):13897–13905, May 1994.

[30] Y. P. Hsu. Development of a Gaussian hypergeometric function code in the complex domain. *International Journal of Modern Physics C*, 4(4):805–840, August 1993.

[31] Y. Imry. *Introduction to Mesoscopic Physics*. Oxford University Press, Oxford, 1997.

[32] Hong Guo Jeremy Taylor and Jiam Wang. Ab initio modeling of quantum transport properties of molecular electronic devices. *Physical Review B*, 63(24):245407–1–245407–13, June 2001.

[33] Frank Jones. *Lebesgue Integration on Euclidean Space*. Jones and Brtlett Publishers International, Boston, London, 1993.

[34] Sakari Lahti Jouko Nieminen and Sami Paavilainen. Contrast changes in STM images and relations between different tunneling models. *Physical Review B*, 66(16):165421–1–165421–9, October 2002.

[35] M. Kleber. Exact solutions for time–dependent phenomena in quantum mechanics. *Physics Reports*, 236(6):331–393, 1994.

[36] Hagen Kleinert. *Pfadintegrale*. BI–Wissenschaftsverlag, Mannheim Leibzig Wien Zürich, 1993.

[37] W. Kohn and L.J. Sham. Self–Consistent Equations Including Exchange and Correlation Effects. *Physical Review A*, 140(4):A1133–A1138, November 1965.

[38] H.J. Kreuzer and L.C. Wang. Self–consistent calculation of atomic absorbtion on metals in high electric fields. *Physical Review B*, 45(20):12050–12055, May 1992.

[39] Hirondo Kuki. Complex Gamma Function with Error Control. *Communications of the ACM*, 15(4):262–267, 271, 272, April 1972.

[40] L.D. Landau and E.M. Lifschitz. *Quantenmechanik*. Akademie–Verlag, Berlin, fifth edition, 1974.

[41] R. Landauer. Electrical Transport in Open and Closed Systems. *IBM J. Res. Dev.*, 1(217), 1957.

[42] N.D. Lang and W. Kohn. Theory of Metal Surfaces: Charge Density and Surface Energy. *Physical Review B*, 1(12):4555–4568, June 1970.

[43] Qing Huo Liu and Zhong Qing Zhang. Nonuniform fast Hankel transfrom algorithm. *Applied Optics*, 38(32):6705–6708, November 1999.

[44] August Ludviksson. A simple model of a decaying quantum mechanical state. *Journal of Physics A*, 20:4733–4738, 1987.

[45] Vittro Magni, Giulio Cerullo, and Sandro De Silvestri. High–accuracy fast Hankel transform for optical beam propagation. *J. Opt. Soc. Am. A*, 9(11):2031–2033, November 1992.

[46] D.M. Eigler M.F. Crommie, C.P. Lutz. Confinement of Electrons to Quantum Corrals on a Metal Surface. *Science*, 262:218–220, October 1993.

[47] B. Mrowka and A. Recknagel. *Physik Zeits.*, 38:758, 1937.

[48] Fritz Oberhettinger. *Tables of Bessel Transforms*. Springer–Verlag, Berlin Heidelberg New York, 1972.

[49] Mustafa H. A. Riza. Streutheoretische Beschreibung des Rastertunnelmikroskops. Master's thesis, Technische Universität München, October 1996.

[50] L.S. Rodberg and R.M. Thaler. *Introduction to the Quantum Theory of Scattering*. Academic Press, 1967.

[51] Paul Roman. *Advanced quantum theory*. Addison–Wesley, Reading, Massachusetts, 1965.

[52] E. G. Peter Rowe. Spherical delta functions and multipole expansions. *Journal of Mathematical Physics*, 19(9):1962 – 1968, September 1978.

[53] M.H. Boon S. Crampin and J.E. Inglesfield. Influence of Bulk States on Laterally Confined Surface State Electrons. *Physical Review Letters*, 73(7):1015–1018, August 1994.

[54] W. Sacks. Tip–Orbitals and atomic corrugation of metal surfaces in Scanning Tunneling Microscopy. *Physical Review B*, 61(11):7656–7668, March 2000.

[55] Jun John Sakurai. *Modern Quantum Mechanics*. Addison–Wesley, Reading, Massachusetts, 1985.

[56] Philippe Sautet. Images of Adsorbates with the Scanning Tunneling Microscope: Theoretical Approaches to the Contrast Mechanism. *Chemical Reviews*, 97:1097–1116, 1997.

[57] J. Schwinger. *Particles sources and fields*, volume 2. Addison–Wesley, Reading, Massachusetts, 1973.

[58] C. Bracher M. Kleber T. Kramer. Four-path interference and uncertainty principle in photodetachment microscopy. *Europhysics Letters*, 56(4):471–477, 2001.

[59] C. Bracher M. Kleber T. Kramer. Matter waves from quantum sources in a force field. *Journal of Physics A*, 35(40):8361–8372, October 2002.

[60] J. Tersoff and D.R. Hamann. Theory and Application for the Scanning Tunneling Microscope. *Physical review letters*, 50(25):1998–2001, June 1983.

[61] J. Tersoff and D.R. Hamann. Theory of the scanning tunneling microscope. *Physical Review B*, 31(2):805–813, January 1985.

[62] M. Trott and Ch. Schittler. Construction and application of the green's function for stepwise constant potentials. *Physica Status Solidi*, 152(1):153 – 161, 1989.

[63] A. Lohr W. Becker and M. Kleber. Effects of rescattering on above–threshold ionization. *Journal of Physics B*, 27(14):L325–L332, July 1994.

[64] G.N. Watson. *A Treatise on the Theory of Bessel Functions*. Cambridge University Press, Cambridge, 2 edition, 1996.

[65] "P. Weinberger". *Electron Scattering Theory for Ordered and Disordered Matter*. Clarendon Press, Oxford, 1990.

[66] E.J. Weniger and E.O. Steinborn. New representations for the spherical tensor gradient and spherical delta function. *Journal of Mathematical Physics*, 24:2553–2563, 1983.

[67] K. Wódkiewicz. Fermi pseudopotential in arbitrary dimensions. *Physical Review A*, 43(1):68–76, January 1991.

Danksagung

An erster Stelle möchte ich mich bei Prof. Dr. Manfred Kleber bedanken, der durch die Motivation und Untersttzung wesentlich zum Gelingen dieser Arbeit beigetragen hat. Fr das angenehme Arbeitsklima und die wertvollen Diskussionen in unserer Gruppe will ich Tobias Kramer, Christian Bracher und Mustafa Riza hier besonders danken.

Außer der Arbeitsgruppe mï£¡hte ich insbesondere meiner Frau Daniella danken, die wohl am meisten unter dieser Arbeit zu leiden hatte.